INVESTIGATING LARGE EARTHQUAKE RUPTURE KINEMATICS FROM THE JOINT ANALYIS OF SEISMOLOGICAL, GEODETIC AND REMOTE SENSING DATA

Thesis by

A. Ozgun Konca

In Partial Fulfillment of the Requirements for the Degree of

Doctor of Philosophy

CALIFORNIA INSTITUTE OF TECHNOLOGY

Pasadena, California

2008

(Defended April 24, 2008)

ACKNOWLEDGEMENTS

I would like to thank my advisor Don Helmberger, and although not official, my co-advisor Jean-Philippe Avouac. Not only did I appreciate their scientific skills, but I also personally liked them as human beings. I am grateful for their support and efforts throughout my PhD. I hope I can get to be as good advisers as them one day. I would also like to thank my thesis committee members Jeron Tromp and Mark Simons. I should also mention Hiroo Kanamori, he was a great inspiration to me as a scientist and a teacher.

I also want to mention my collaborators throughout this PhD; Kerry Sieh, Sebastien LePrince, Mohamed Chlieh, Rich Briggs, Aron Meltzner, Alex Song, Eric Fielding, John Galetzka, Ken Hudnut, Sarah Minson, and Anthony Sladen. Thanks for sharing your efforts, knoweledge and ideas with me.

I would like to thank Vala Hjorleifsdottir, for her friendship and being a cool colleague. I am grateful to Chen Ji, who introduced me to studying large events and to his code. Jascha Polet, Leo Eisner, Javier Favela, Brian Savage, and Anupama Venkataraman were of great help when I first arrived as an inexperienced young student. I also would like to thank friends who shared dinners, lunches and chats; Lydia and Chris, Nathan, Min. I would like to thank my officemates Debbie, Chen, Min, Xianyang, and Francisco.

Viola Carter was more than an administrator of the lab for most of us, and for me too. She increased our quality of life with incredible efforts beyond her duties throughout these years. I will not forget her devotion.

I also have met many Turkish friends at Caltech over the years. Thanks a lot Sirin, Arkadas, Can, Caglar, Selim, Burak Erdogan, Burak Cendek, Ahmet, Omer, Muruvvet, Mustafa, Ersen, Ercan, and Bahar.

I feel that I also need to include my yoga instructor, Paul Cabanis in the acknowledgement. His Iyengar style yoga classes were of great help in focusing and concentration, mental and physical health in the last year of my PhD.

The greatest of thanks comes to my family, my parents Haydar and Naciye, siblings, Ozgur and Gunos Abla, and my girlfriend Yeliz. Their support has been the most influential to keep me going at the times I needed support. Their love and devotion was

beyond words and I take comfort in knowing that I will be with them in my life in later years, too.

ABSTRACT

This thesis presents detailed studies of 4 large earthquakes. The 2006 M_w 8.6 Nias-Simeulue earthquake and 2007 Sumatra M_w 8.4 and 7.9 earthquake sequence which occurred on the Mentawai Island area of Sunda megathrust are studied using teleseismic, long period, GPS, and field data. Two crustal earthquakes, the 2005 M_w 7.6 Kashmir and the 1999 M_w 7.1 Duzce earthquakes, are studied using satellite image cross-correlation, seismic, GPS and SAR data.

The 2005, M_w 8.6, Nias-Simeulue earthquake was caused by rupture of a portion of the Sunda megathrust offshore northern Sumatra. Based on the excitation of the normal modes and geodetic data, we put relatively tight constrains on the seismic moment and the fault dip, where the dip is determined to be 8^o to10^o with corresponding moments of 1.24×10^{22} to 1.00×10^{22} Nm, respectively. The geodetic constraints on slip distribution help to eliminate the trade-off between rupture velocity and slip kinematics. Our results indicate a relatively slow average rupture velocity of 1.5 to 2.5 km/s and long average rise time of up to 20 s.

Our study of the 2007 Mentawai Islands earthquakes shows the influence of permanent barriers on the extent of large megathrust ruptures, which can be a cause of some regularity of the seismic behavior, but also that the same portion of a megathrust can rupture in different patterns depending on whether asperities break as isolated seismic events or cooperate to produce a larger rupture. This variability arises mostly from the influence of nonpermanent barriers, probably zones with locally lower prestress due to the past earthquakes. The state of stress on that portion of the Sumatra megathrust was not adequate for the development of a single major large rupture at the time of this seismic crisis. However, the slip deficit that has accumulated since the 1833 and 1797 events remains large, and so is the potential for a large megahrust event in the Mentawai area.

We analyzed the rupture process of 1999 M_w 7.1 Duzce earthquake using geodetic and seismic data. Applying subpixel cross-correlation of SPOT images acquired before and after the event, we mapped a continuous fault trace over 55 km; 15 km longer than the field reports. We investigated the spatiotemporal evolution of the earthquake using four-segment fault geometry with constraints on surface offsets based on satellite imagery, incorporated GPS and InSAR data and four strong-motion stations in the vicinity of the rupture. Our joint modeling

shows a very stable slip distribution that does not depend on constraints imposed on rupture velocity. We show that no constant rupture velocity can explain the strong-motion data. Due to constraints from fault geometry and geodetic data, the rupture velocity has to vary rapidly. The rupture starts slow, accelerates to supershear speeds toward east and subsequently slows down. Supershear rupture is local and only toward the east of the hypocenter. Teleseismic data are consistent with the joint near-field model when 2 s time shifts are applied to their hand-picked arrivals. This implies that the weak beginning of the earthquake is not observable at teleseismic distances. This appears to be a common problem with teleseismic modeling and leads to more compact models with major slip around the hypocenter than the actual phenomenon. We performed teleseismic inversion models comparing four-segment fault geometry based on satellite imagery to one-segment geometry based on CMT solution. The four-segment model gives better predictions of near-field ground motions.

We analyzed the M_w 7.6 Kashmir earthquake of October 8, 2005, using sub-pixel correlation of ASTER images to measure ground deformation, and modeling SAR imagery data along with seismic waveforms. The surface rupture is continuous over a distance of 75 km. The rupture lasted about 25 s and propagated up-dip and bilaterally by ~2 km/s, with a rise time of 2-5 s. The shallowness and compactness of the rupture, both in time and space, provide an explanation for the intensity of destructions. By comparing the teleseismic models with SAR data, we infer that satellite image correlation puts constraints on teleseismic models, which lead to more coherent models with the geodetic data. This kind of satellite image analysis could be achieved as soon as a postearthquake image is available, and would provide key information for early assessment of damages.

TABLE OF CONTENTS

Acknowledgements iii
Abstract v
Table of Contents vii
List of Figures ix
List of Tables xi
Chapter 1: Introduction 1
1.1 Objective and Summary 1
1.2 Method 2
Chapter 2: 2005 Rupture Kinematics of the Nias-Simeulue Earthquake 9
2.1 Abstract 9
2.2 Introduction 9
2.3 Seismological and geodetic data 10
2.4 Inversion of the data: modeling approach 15
2.5 Determination of seismic moment and fault dip angle 16
2.6 Source models obtained from inversion of seismic and geodetic data 18
2.7 Testing the source models against long period data 27
2.8 Strong motion estimates 29
2.9 Discussion 31
2.10 Conclusion 36
2.11 Acknowledgement 37
Chapter 3: Mentawai Earthquake Sequence on the Sumatra Megathrust 38
3.1 Abstract 38
3.2 Introduction 38
3.3 Datasets 40
3.4 Finite source models 43
3.5 Discussion 50
3.6 Conclusion 54
3.7 Supplementary Information 55
3.8 Acknowledgement 64
Chapter 4: Rupture Process of M_w 7.1 Duzce Earthquake 65
4.1 Abstract 65
4.2 Introduction 65
4.3 Fault trace and offsets: Sub-pixel cross-correlation of images 68
4.4 Datasets 73
4.5 Inversion Method 74
4.6 Joint near-field models with surface offset constraints 74
4.7 Prediction of teleseismic data from the near-field Data 83
4.8 Strong-Motion Estimation using Teleseismic Data 85
4.9 Conclusion 89
4.10 Acknowledgement 90

Chapter 5: The 2005, M_w 7.6, Kashmir Earthquake: Sub-pixel Correlation of ASTER Images, Seismic Waveform and SAR Analysis 91
5.1 Abstract 91
5.2 Introduction 91
5.3 Remote-sensing analysis 93
5.4 Seismological Analysis 98
5.5 Discussion 100
5.6 Conclusion 107
Chapter 6: Conclusions 109
Bibliography 111

LIST OF FIGURES

Number *Page*

1.1 Synthetic model and data for simulated annealing example 5
1.2 Result of synthetic inversion at various iterations 6
1.3 Fits to the data and comparison of input and output models 7
1.4 Progression of misfit with iterations 8
2.1 The location of the Nias-Simeulue Earthquake 13
2.2 Prediction of Earth's normal modes from finite fault model 17
2.3 Slip distributions of models of various combinations of datasets 19
2.4 Fits to the teleseismic data 21
2.5 Map view of slip and fits to GPS data for various models 22
2.6 Uplift distribution predicted from various models 24
2.7 Slip and rise time distributions of various models 25
2.8 Fits to the 100 to 500 s waves using best model with SEM 28
2.9 Prediction of time evolution of motion at the GPS site LHWA 30
2.10 Fits to datasets with various rupture velocity constraints 34
3.1 Interseismic coupling and large events on Sunda megathrust 41
3.2 Cumulative slip distribution and fits 45
3.3 Source model of the M_w 8.4 earthquake 47
3.4 Source model of the M_w 7.9 earthquake 49
3.5 Latitudinal moment released in large earthquakes 52
3.6 Cumulative slip using GPS only and adding events 59
3.7 M_w 8.4 earthquake fits to the data 60
3.8 M_w 7.9 earthquake fits to the data 61
3.9 Slip and rise time for M_w 8.4 and M_w 7.9 earthquakes 62
3.10 Moment rate of M_w 8.4 event with and without the deep patch 63
3.11 Fits to the LAIS station with and without the deep patch 63
3.12 Geodetic data residuals from the cumulative model 64

4.1 Map of the Duzce study area and datasets 67
4.2 Cross-correlated SPOT images 69
4.3 Comparison of fault trace and surface offsets; field vs SPOT 70
4.4 Slip and rise time maps for models with various rupture velocities .. 75
4.5 Fits to the GPS and InSAR data 76
4.6 Fits to the strong-motion data 80
4.7 Progression of rupture for the preferred model 82
4.8 Prediction of teleseismic waves from near-field model 84
4.9 Map view of teleseismic models with various fault geometries 86
4.10 Fits to the teleseismic data from teleseismic models 87
4.11 Prediction of strong-motion data from teleseismic models 88
5.1 Tectonic setting of Kashmir earthquake 92
5.2 Cross-correlated ASTER images 94
5.3 Map of fault trace obtained from satellite imagery 95
5.4 Map of fault trace with offsets 96
5.5 Fits to the teleseismic data 98
5.6 Slip distribution of teleseismic model 100
5.7 Map view of slip models with different geometries and datasets 103
5.8 Fits to the teleseismic data 104
5.9 Fits to the SAR data 105
5.10 Fault trace in the bedrock geology 106

LIST OF TABLES

Number *Page*

2.1 GPS data for the Nias-Simeulue earthquake 14

2.2 Fault geometry 14

2.3 Velocity model 14

3.1 Information on interferograms 57

3.2 Misfits and normalized uncertainties for models and events 58

4.1 Information on SPOT images 71

4.2 geometry and dimensions of the fault model 71

4.3 Velocity model for static and teleseismic data 71

4.4 Model descriptions and misfits to datasets 71

Chapter 1: Introduction

1.1 Objective and Summary

Studying earthquakes is one of the key interests of geophysics. The global seismic networks provide seismic data in almost real time, strong-motion data are becoming more commonly available, and the developments in satellite imagery, GPS, and radar interferometry provide data that need to be used all together. The purpose of this thesis is to exhibit models of earthquakes with realistic fault geometries based on satellite images and using both geodetic and seismic data in various frequency bands to improve our understanding of earthquakes.

There are studies of 4 large earthquakes in this thesis. The first two chapters focus on events on the Sumatra subduction zone. The last two chapters focus on two crustal earthquakes and using multiple datasets along with realistic geometries based on satellite image cross-correlation.

In chapter 2, we model teleseismic, GPS and field data for the 2005 M_w 8.6 Nias-Simeulue earthquake. We used long period surface waves and earth's normal mode excitation along with joint teleseismic and geodetic modeling to constrain slip distribution, and moment of the earthquake and obtain an average dip angle for the megathrust.

In chapter 3, we study the 2007 Mentawai Island sequence. We model the M_w 8.4 and M_w 7.9 earthquakes using GPS, coral uplift and teleseismic data. By comparing these models to the prior works of historical earthquakes and interseismic coupling, we try to assess how a subduction zone works, how the coseismic earthquake ruptures relate to historical events and interseismic coupling.

In chapter 4, we study the 199 M_w 7.1 Duzce earthquake of Turkey. By using SPOT images before and after the earthquake, we obtain the fault rupture accurately along with surface offsets. We use a realistic fault geometry, constrain surface slip and model all geodetic and strong-motion data to study the earthquake kinematics. We also use models of near-field data to predict far-field seismograms and modeling of teleseismic data to predict nearfield data

to investigate how nearfield and farfield models compare. We test whether addition of optical imagery constraints to teleseismic models can be used to improve rapid earthquake models and estimates of near-field ground motions.

In chapter 5, we study the 2005 M_w 7.6 Kashmir Earthquake using ASTER image cross-correlation, teleseismic and SAR data. We obtain a fault trace from satellite images before and after the earthquake, and build a multiple plane fault model. We compare the rupture to the geological setting to show the structural control on rupture. We use SAR data to refine the source models and compare how the various datasets contribute to the refining of the earthquake model.

1.2 Method

1.2.1 Basics of Simulated Annealing Method for Optimization

Throughout this thesis, we have used the inversion method of (Ji, Wald and Helmberger 2002a) that applies simulated annealing method, which involves searching for the best fit model in the bounded parameter space starting from a random model. Therefore, it is worthwhile to go over the basics of the method with an example.

The joint inversions require fitting the wavelet transform of seismograms and geodetic data using simulated annealing algorithm. The seismograms are calculated by

$$u(t) = \sum_{j=1}^{n} \sum_{k=1}^{m} D_{jk} \cdot Y_{jk}\left(\vec{x}, t - d_{jk} / V_{jk}\right) \cdot \dot{S}_{jk}(t), \qquad (1.1)$$

where j and k are indices of summation along strike and dip, respectively, Y_{jk} are the sub-fault Green's functions, D_{jk} the dislocations, V_{jk} are the rupture velocities between the hypocenter and sub-faults and d_{jk} are the distance of the sub-fault from the hypocenter. The rise time for each element is given by $S_{jk}(t)$. Both the V_{jk}'s and $S_{jk}(t)$'s control the timing of the contribution from each sub-fault. We approximate $S_{jk}(t)$ the latter as a modified cosine function defined by one parameter, as first proposed by (Cotton and Campillo 1995b). These seismograms are then transformed to wavelet domain to use the time and frequency variations in the signal.

The misfit between the measurement and synthetic waveforms is quantified by the sum of L1 and L2 norms of the seismograms in different wavelet channels:

$$e_l = \sum_{j=j_{\min}}^{j=jc} w_j \cdot \left(\frac{1}{k_j} \sum_{k}^{k_j} \left| o_{j,k} - y_{j,k} \right| + \sqrt{\frac{1}{k_j} \sum \left(o_{j,k} - y_{j,k} \right)^2} \right), \qquad (1.2)$$

where $o_{j,k}$ and $y_{j,k}$ are the wavelet coefficients of the observed and synthetic seismogram for station k and wavelet index j, w_j are the weight of each wavelet channel (Ji, Wald and Helmberger 2002b).

The static displacement Green's functions are calculated with the method developed by (Xie and Yao 1989). The model prediction is done by adding the appropriate Green's functions from the point sources of the finite fault. We compare the quality of the fit to the geodetic data provided by each source model based on the reduced chi-square criteria defined as:

$$\chi_r^{\,2} = \frac{1}{n} \sum_{i=1}^{i=n} \left(\frac{(pred^i - ob^i)}{\sigma_i} \right)^2, \qquad (1.3)$$

where n is the number of geodetic data, σ_i is the uncertainty associated for the each measurement ob^i, $pred^i$ is the predicted displacement at site i.

In addition, we constrain the solution by requiring minimization of slip difference between adjacent faults (smoothing) and minimizing the moment difference from an *a priori* value (moment constraint). The objective function is

$$misfit = e_{WF} + W_{ST} e_{ST} + Wsm \cdot e_{SM} + W_{MO} \cdot e_{MO}, \qquad (1.4)$$

where e_{WF} is the waveform error, W_{ST} is the weight of the static data, e_{ST} is static data error, w_{SM} and e_{SM} are weight and error for smoothness, and w_{MO} and e_{SM} are weight and error for moment constraint, respectively.

All inversions start with a random initial model. The weight of the static error is then chosen to be equal to the waveform error. Weights of the constraining parameters are determined by trial and error. As the bound parameter space is searched, the objective function is minimized with a predefined number of iterations. At each iteration, the parameters are changed by a random neighborhood algorithm depending of the temperature ($\boldsymbol{T}$) of the system and misfit is calculated. Probability of selecting the new model as the best fit model depends on the misfit of the new model. There is finite probability of moving to a higher error

state to avoid being stuck to local minimum error point. The temperature is gradually decreased so the randomness is decreases and solution converges to a minimum, using

$$T = T_0 \cdot \beta^N \ , \tag{1.5}$$

where T is the temperature at iteration number N, T_o is the initial temperature and β is the cooling parameter.

1.2.2 Synthetic example of a teleseismic inversion using simulated annealing method

We illustrate an example of a teleseismic inversion to better understand the simulated annealing method. It should be noted that this example is not set up to perform a resolution test; it is shown for illustrative purposes.

Initially, we build a synthetic rupture model based on the 1999 M_w 7.1 Duzce earthquake, which is discussed in detail in chapter 4 of this manuscript (see Figure 1.1 for the list of parameters used to build the synthetic input model). The synthetic data are then calculated at teleseismic distances for 19 P and 17 SH waveforms. Afterwards we model the synthetic data calculated from the model shown in Figure 1.1. Figure 1.2 shows the progression of the model through iterations for $\beta = 0.99$. By 200 iterations, the solution converges to a minimum. Comparison of the input and output models (Figure 1.2, Figure 1.3) show that the solution is quite similar to the input, except that it is much smoother, especially for the deeper patch toward west of the hypocenter. The map view of the input and output models and fits to the data are shown in Figure 1.3

Figure 1.4 shows the convergence of teleseismic models for various models of cooling parameter. For this simple example, all solutions converge to the same value of misfit. However, the solution with $\beta = 0.99$ searches a broader range of parameter space. Throughout this study, we use $\beta = 0.99$ *or* $\beta = 0.98$ to assure enough randomness in order to span the parameter space.

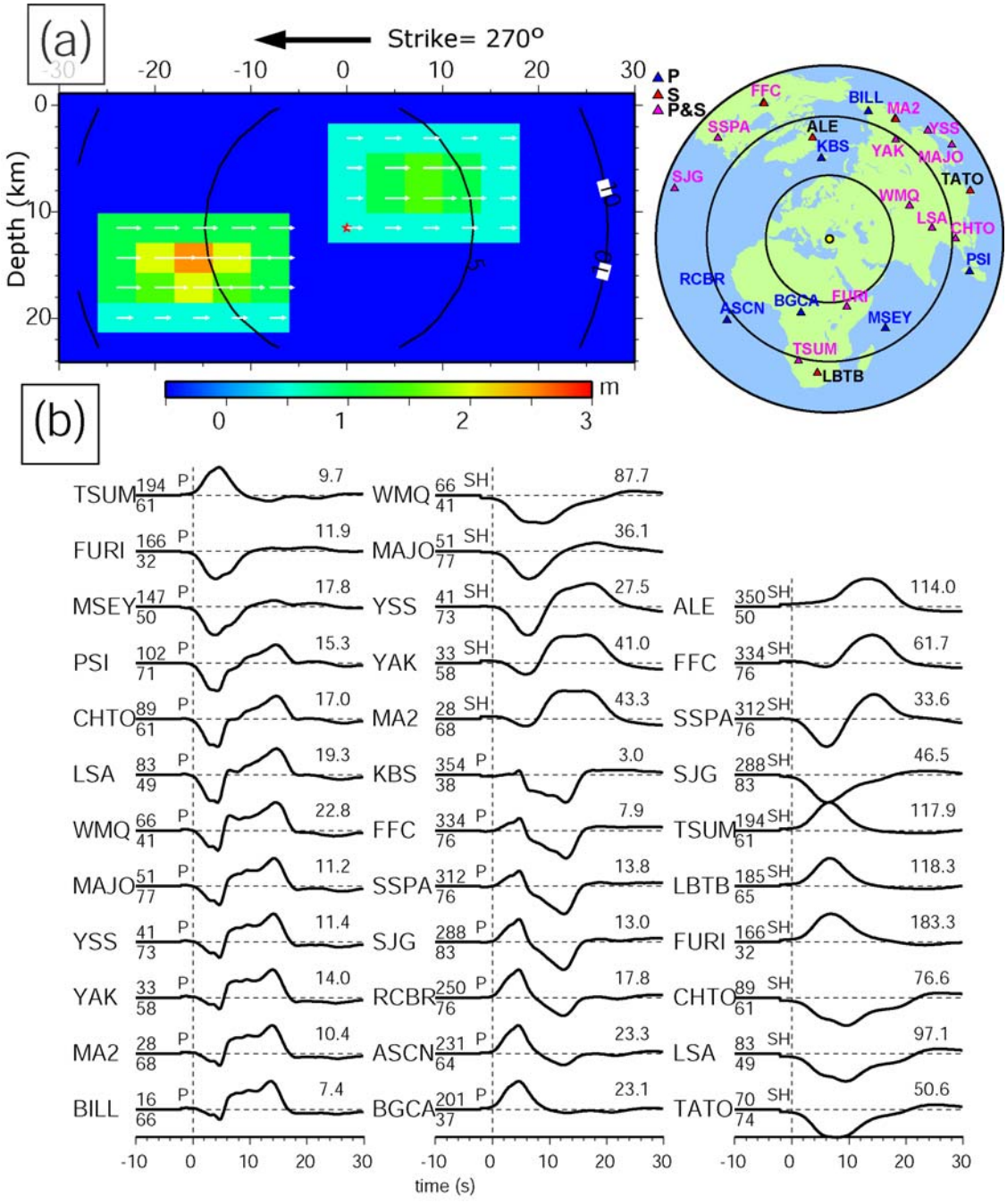

Figure 1 1 (a) The input model for an M_w 6.85 earthquake with a dip angle of 65°, rake of 180°, rupture velocity of 2.8 km/s, and rise times scaled with slip by 50 cm in 1s scale. The 5 s rupture contours are also shown. (b) The synthetic data calculated from the model in (a) at the station locations shown in the inset.

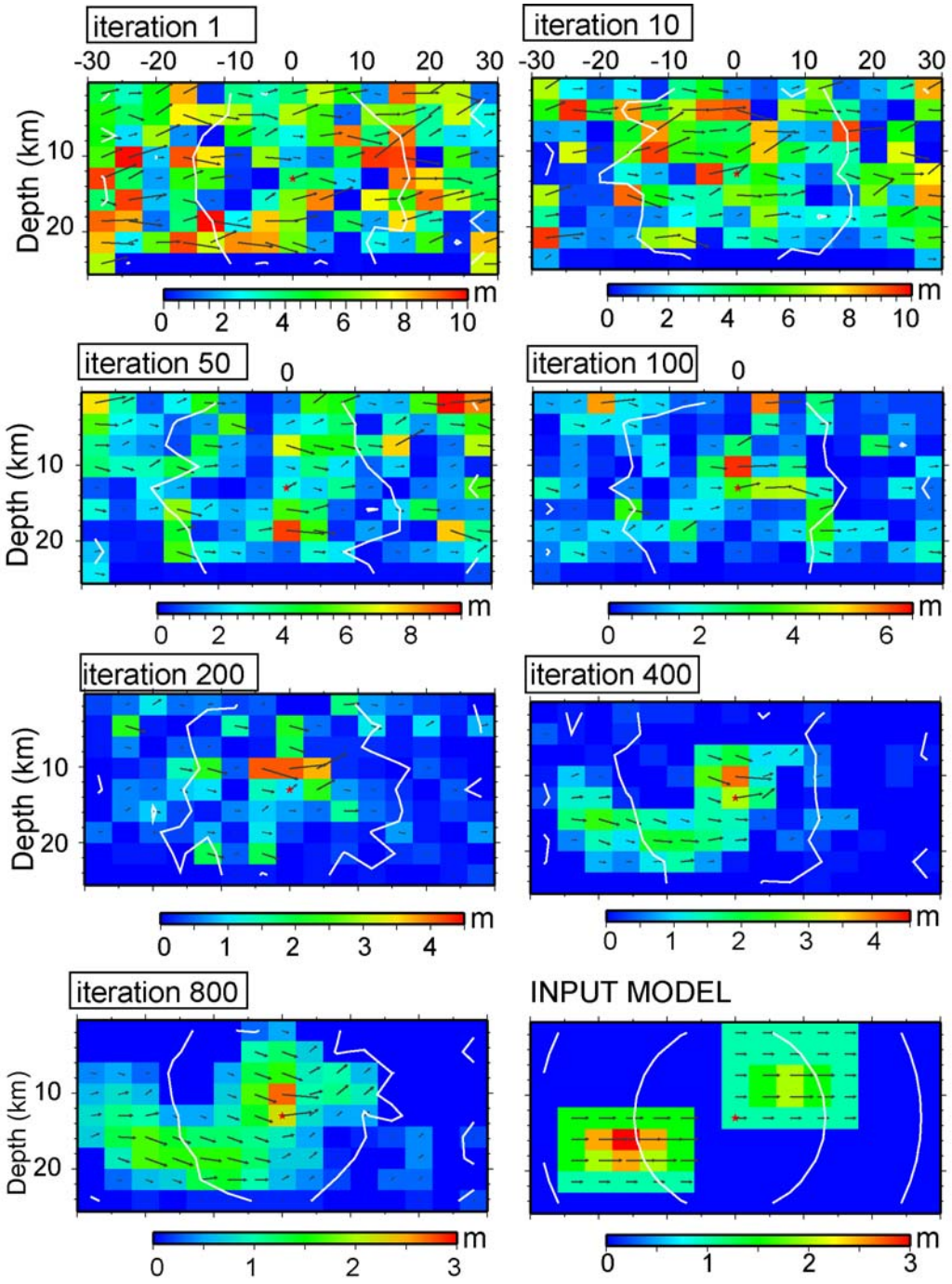

Figure 1.2 The result of the inversion at various iteration stages. The ranges for the parameter spaces in the inversion are: slip: 0-5m, rupture velocity: 2-3.5 km/s, rise time: 1-7s, rake: 160°-200°. Input model is displayed next to the final iteration of inversion for comparison.

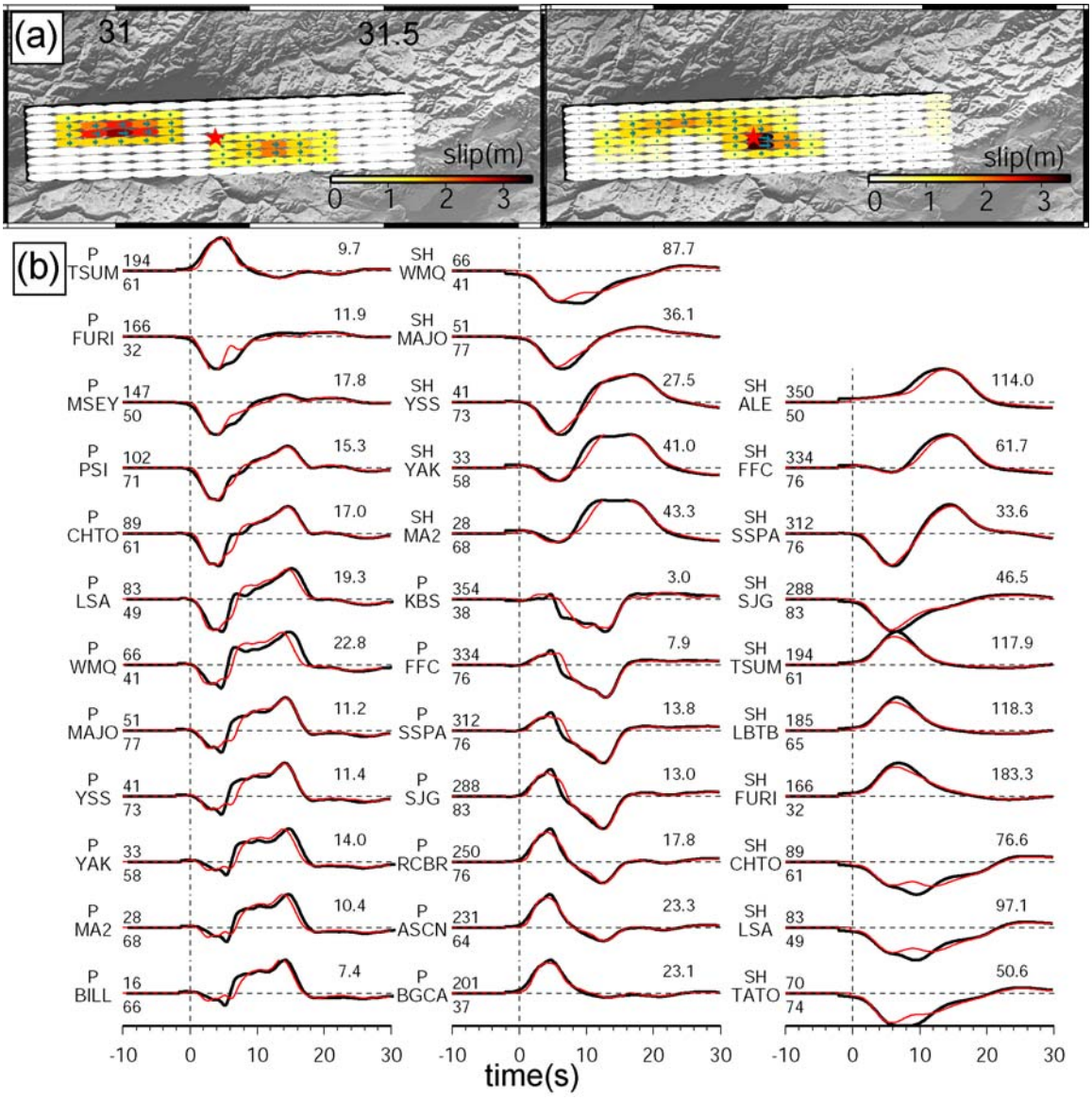

Figure 1.3 (a) Map view of input (left) and output (right) slip models (b) Fits to the teleseismic data of the model shown in Figure 1.2. Black traces are data and red traces are synthetics.

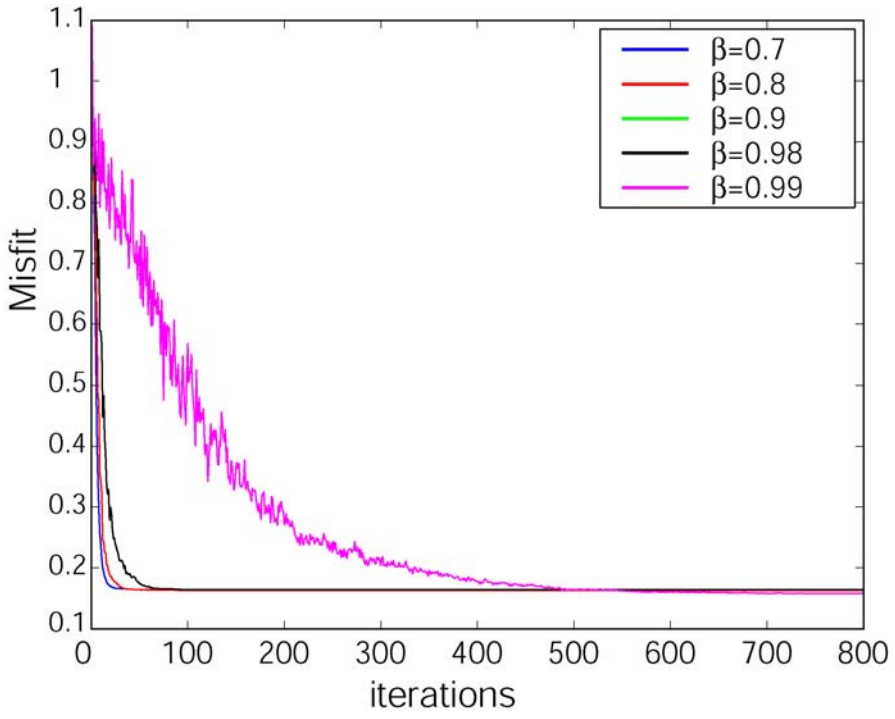

Figure 1.4 Progression of misfit through iterations for various values of cooling parameter β for the inversion of the teleseismic data from model in Figure 1.1.

Chapter 2: Rupture Kinematics of the 2005, M_w 8.6, Nias-Simeulue Earthquake from the Joint Inversion of Seismic and Geodetic data

2.1. Abstract

The 2005, M_w 8.6, Nias-Simeulue earthquake was caused by rupture of a portion of the Sunda megathrust offshore northern Sumatra. This event occurred within an array of continuous GPS stations and produced measurable vertical displacement of the fringing coral reefs above the fault rupture. Thus, this earthquake provides a unique opportunity to assess the source characteristics of a megathrust event from the joint analysis of seismic data and near-field static co-seismic displacements. Based on the excitation of the normal mode data and geodetic data we put relatively tight constrains on the seismic moment and the fault dip, where the dip is determined to be 8^o to 10^o with corresponding moments of 1.24×10^{22} to 1.00×10^{22} N.m, respectively. The geodetic constraints on slip distribution help to eliminate the trade-off between rupture velocity and slip kinematics. Source models obtained from the inversion of various combinations of the teleseismic body waves and geodetic data are evaluated by comparing predicted and observed long period seismic waveforms (100 s to 500 s). Our results indicate a relatively slow average rupture velocity of 1.5 to 2.5 km/s and long average rise time of up to 20 s. The earthquake nucleated between two separate slip patches, one beneath Nias and the other beneath Simeulue Island. The gap between the two patches and the hypocentral location appears to be coincident with a local geological disruption of the forearc. Coseismic slip clearly tapers to zero before it reaches the trench, probably because the rupture propagation was inhibited when it reached the accretionary prism. Using the models from joint inversions, we estimate the peak ground velocity on Nias Island to be about 30 cm/s, an order of magnitude slower than for thrust events in continental areas. This study emphasizes the importance of utilizing multiple datasets in imaging seismic ruptures.

2.2. Introduction

The characteristics of large subduction earthquakes, in particular those regarding the rupture kinematics and near-field ground motion, remain poorly known. This is a major

societal concern since many of the world's largest cities are situated close to subduction plate boundaries. Because great events have long repeat times, generally hundreds of years, few of them have been recorded by modern geophysical instruments. In addition, along most subduction zones the seismogenic portion of the plate interface lies offshore, making the near-field area inaccessible for direct observation. In the few case studies where geodetic or strong-motion data can be compared with far-field seismological data, it appears that shaking was less severe than in earthquakes of similar magnitude in other tectonic settings. Specific examples include the 1985 M_w 8.1 Michoacan earthquake offshore Mexico (Anderson et al., 1986), the 2003 M_w 8.1 Tokachi-oki earthquake offshore Hokkaido (Honda et al., 2004) and the 1995 M_w 8.1 Antofagasta earthquake offshore Chile (Ruegg et al., 1996). It is, however, unclear whether relatively moderate shaking is a general characteristic of subduction events and whether it is related to propagation effects, to the radiation pattern, or to other source characteristics. The recent 2005 M_w 8.6 Nias-Simeulue earthquake (Figure 2.1) is unique in that (1) it occurred within an array of continuously recording GPS stations, the Sumatran GPS Array (SuGAr) and (2) several islands lying above the seismogenic rupture made it possible to measure vertical displacements from the uplift or subsidence of fringing coral reefs. These datasets provide excellent constraints on the distribution and magnitude of slip and make the determination of a more reliable rupture history possible.

Various combinations of teleseismic waveforms and the geodetic dataset are used here to derive a finite source model of the earthquake and to assess their corresponding strong ground motions. Seismic waveforms can be used on their own to invert for fault slip histories (Ammon et al., 2005), but such modeling is generally non-unique, due to trade-offs between rise time (time for the offsets to develop on a point on the fault plane), slip magnitude and rupture velocity. The availability of near-field geodetic data significantly reduces these trade-offs. The above source models are tested against long period data and normal mode excitations, utilizing the sensitivity of these datasets to moment of the earthquake and dip of the fault.

2.3 Seismological and geodetic data used in determining source models

Azimuth and relative simplicity were the principal criteria for selecting the teleseismic waveforms from the IRIS network (Figure 2.1, inset). Simplicity is judged by examining smaller

aftershock observations and picking stations with the least number of unidentified phases. The broadband seismograms were band-pass filtered from 0.8 s (P-waves) and 2 s (SH-waves) to 200 s. The long-period seismograms were selected between 40° and 100° distance and band-pass filtered from 100 s to 500 s. Normal modes spectrum below 1 mHz (> 1000 s) are generated by Hann tapering 144 hours of time series prior to discrete Fourier Transformation.

We use two types of geodetic data, GPS and coral microatoll measurements, to characterize coseismic surface deformation due to the Nias-Simeulue rupture. An array of continuously recording GPS (cGPS) stations, the Sumatran GPS Array (SuGAr), had been deployed in the years and months preceding the Nias-Simeulue earthquake. The stations record at a 120-second sampling rate and the data are available from the Caltech Tectonics Observatory web site (http://www.tectonics.caltech.edu/sumatra/data). These data and those from the cGPS station at Indonesian National Coordinating Agency for Surveys and Mapping site SAMP near Medan along the northeast coast of Sumatra were used to estimate the coseismic displacements (Briggs et al., 2006). Two GPS stations on Nias (LHWA) and Simeulue Islands (BSIM) recorded large (>2 m) coseismic displacements for the Nias-Simeulue earthquake (Figure 2.1). The stations LEWK (to the north) and PTLO and PBAI (to the south) constrain the extent of the rupture in the lateral direction. The GPS coseismic displacements from Briggs et al., (2006) were determined by least-squares fitting the time series from a model consisting of a linear trend for the secular interseismic motion, a heaviside function for the co-seismic, an exponential term for postseismic displacement and sinusoidal terms to correct for annual and semi-annual variations (see http://sopac.ucsd.edu for details). The data from the day of the earthquake were discarded. Most of the SUGAR stations in the epicentral area were deployed in January so that the preseismic dataset is limited. The estimates obtained from this approach are consistent with more elaborated models of the postseismic deformation within a few centimeters, showing that the exponential decay law assumed here does not introduce any significant bias (Hsu et al., 2006). In addition preliminary results from 120s solutions show no resolvable postseismic deformation during the first day. Uncertainties are of the order of 0.1-1 cm at the 1-σ confidence level. These measurements and their uncertainties are listed in Table 2.1.

The second geodetic dataset comes from field measurements of coseismic uplift and subsidence utilizing *Porites* coral microatolls (Briggs et al., 2006), which act as natural recorders of sea level changes with accuracies of a few centimeters (Scoffin and Stoddart 1978; Taylor et al., 1987; Zachariasen et al., 1999). Coseismic uplift or subsidence can be determined readily from the change in elevation between the pre- and post-earthquake highest level of survival of living corals with errors of ±6-25 cm. The coral data of Briggs et al. (2006) reveals a peak in surface displacement along the west coast of Nias and Simeulue, a trough in displacement between these islands and mainland Sumatra, and a line of no vertical displacement between these two zones of deformation. The measurements were collected about 2 to 3 months after the mainshock and, therefore, include some amount of postseismic deformation. Modeling of postseismic deformation using the cGPS data (Hsu et al., 2006), predicts vertical postseismic displacements over the first month at the coral measurement points of just a few cm. These postseismic displacements are generally about 5% of the measured uplift or subsidence, except at the few points near the down-dip end of the rupture zone. Hence, we assume that a correction for postseismic deformation can be neglected in this study.

The dataset used to derive the source models in this paper consist of three-component displacements measured at 16 cGPS stations, 70 measurements of vertical displacement from coral reefs and 26 seismic records (16 *P* and 10 *SH*) (Figure 2.1).

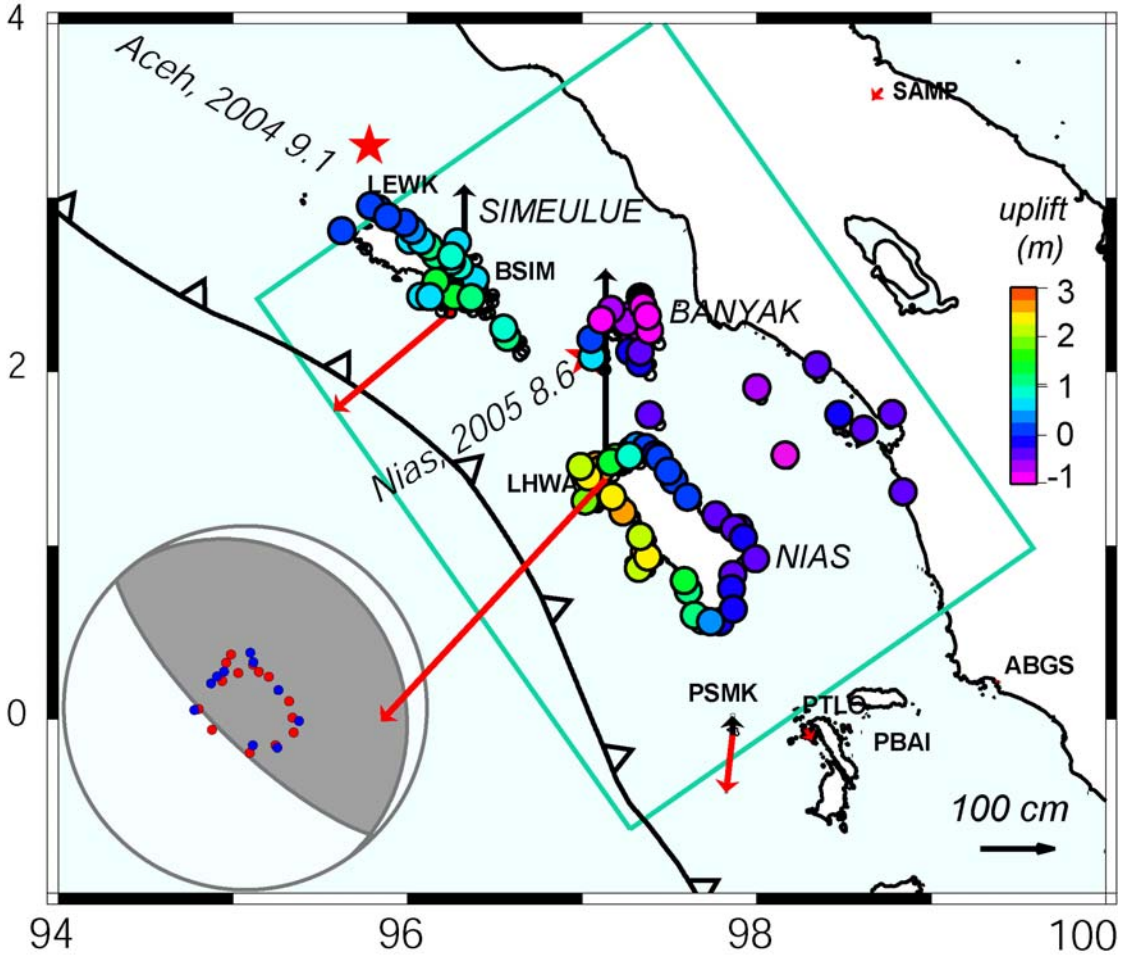

Figure 2.1: Location of the Nias-Simeulue earthquake. The hypocenters of the 2004 Aceh-Andaman and 2005 Nias-Simeulue earthquakes are show with red stars. The surface projection of the fault plane is demonstrated by the blue rectangle. The vertical component cGPS data displacements are shown in black, and the horizontals are in red. Each coral measurement point is shown with a black circle filled with a color scaled with the measured uplift or subsidence. The Simeulue, Nias and Banyak Islands are also shown for reference. The stations used in joint inversions are shown on the beach ball (red for P-waves and blue for SH-waves)

Table 2.1 | GPS data. The list of continuous GPS stations with coseismic offsets and associated 1σ error estimates.

Sta. name	Lon.	Lat.	East(cm)	σ_E (cm)	North	σ_N	vert(cm)	σ_z
ABGS	99.3875	0.2208	-4.54	0.47	-1.17	0.15	-1.48	0.64
BSAT	100.29	-3.0800	0.52	0.12	-0.28	0.06	0.00	0.30
BSIM	96.326	2.4090	-179.16	0.24	-150.54	0.74	159.59	0.17
LEWK	95.8041	2.9236	-11.30	0.20	6.83	0.45	0.66	0.42
LHWA	97.1345	1.3836	-308.31	0.75	-331.97	0.91	288.11	0.37
LNNG	101.1565	-2.2853	0.55	0.19	-0.50	0.13	-0.99	0.39
MKMK	101.0914	-2.5427	0.54	0.19	-0.44	0.14	-0.52	0.35
MSAI	99.0895	-1.3264	2.03	0.58	-0.48	0.21	-1.42	0.74
NGNG	99.2683	-1.7997	0.85	0.15	-0.67	0.09	-0.96	0.25
PBAI	98.5262	-0.0316	-0.85	0.34	-5.38	0.21	-5.51	0.58
PRKB	100.3996	-2.9666	0.82	0.24	-0.35	0.15	-0.79	0.39
PSKI	100.35	-1.1200	0.36	0.20	-0.66	0.09	-0.91	0.22
PSMK	97.8609	-0.0893	-8.87	0.81	-79.00	0.37	26.37	1.04
PTLO	98.28	-0.0500	8.22	0.38	-14.95	0.19	-0.59	0.25
UMLH	95.339	5.0531	-3.58	1.58	-5.76	1.40	1.26	1.58
SAMP	98.7147	3.6216	-12.16	0.64	-13.85	0.26	1.33	0.44

Table 2.2 | Fault Geometry: The corners of the planar fault geometry for the preferred dip of angle of 10° used in the inversions.

Lat	Lon	Depth(km)
-0.63	97.27	3.8
2.42	95.10	3.8
0.98	99.58	59
4.03	97.45	59

Table 2.3 | Velocity Model. Velocity models used in the inversion, modified from crust 2.0 at the location of the epicenter (97.013E, 2.074N).

Depth(km)	v_p(km/s)	v_s(km/s)	ρ (kg/m^3)	μ(GPa)
0-1	2.1	1	2100	2.1
1-8	6.0	3.4	2700	31.2
8-15	6.6	3.7	2900	39.7
15-22	7.2	4.0	3100	49.6
>22	8.1	4.5	3380	68.5

2.4 Inversion of Teleseismic Waveforms and Geodetic Data: Modeling Approach

The geodetic data and seismological waveforms were used to determine the finite source model of the rupture parameterized in terms of a grid of point sources. We employed a simulated annealing algorithm to fit the wavelet transform of the seismograms (Ji, Wald and Helmberger 2002a). For the sake of simplicity, we assumed a planar fault plane constrained to meet the earth surface at the trench taking into account the ~4 km depth of the trench (Figure 2.1). Given the curvature of the trench both along strike and down dip, this is only a first-order approximation. The dip angle was determined to be 10^o based on normal mode excitations and geodetic misfits as discussed below. The geometry of the plane is given in Table 2.2.

The rupture velocity and the rake angle (80^o-115^o) vary within given ranges, except for specific cases discussed later. We used 16 km by 16 km sub-faults, similar to that used for the Aceh-Andaman earthquake (Ammon et al., 2005, Model 3). This grid size was found to offer a good compromise to keep the number of model parameters as low as possible while keeping discretization errors small. We used the hypocenter given by the NEIC (97.013E, 2.074N, 30 km). We extracted 1D velocity model from the crustal model 3D Crust 2.0 (Bassin, Laske and Masters 2000) at the epicenter (Table 2.3).

The displacement field generated by an earthquake can be approximated by summing up the contributions from the various elements (Hartzell and Helmberger 1982a)

$$u(t) = \sum_{j=1}^{n} \sum_{k=1}^{m} D_{jk} \cdot Y_{jk}\left(\vec{x}, t - d_{jk} / V_{jk}\right) \cdot \dot{S}_{jk}(t), \qquad (2.1)$$

where j and k are indices of summation along strike and dip, respectively, Y_{jk} are the sub-fault Green's functions, D_{jk} the dislocations, V_{jk} are the rupture velocities between the hypocenter and sub-faults and d_{jk} are the distance of the sub-fault from the hypocenter. The rise time for each element is given by $S_{jk}(t)$. Both the V_{jk}'s and $S_{jk}(t)$'s control the timing of the contribution from each sub-fault. Thus, the V_{jk}s and $S_{jk}(t)$'s are extremely important in estimating strong motions. We approximate the latter as a modified cosine function defined by one parameter, as first proposed by Cotton and Campillo, (1995a). This greatly reduces the number of parameters compared to the multiple time window used by most researchers (see Ji

et al., 2002a for a discussion of this issue). The static displacements are calculated with the method developed by Xie and Yao (1989) using the same layered elastic half-space (Table 2.3) as for the modeling of the seismic waves.

2.5 Determination of seismic moment and fault dip angle

The long period excitation of a point source depends on the source depth, fault geometry and the seismic moment (Kanamori and Stewart 1976). In the case of a shallow dipping thrust fault, the amplitude of excitation is proportional to $M_0 \sin(2\delta)$, where M_0 is the moment and δ is the dip angle (Kanamori and Given 1981), so that shallower the dip angle, the larger the inferred moment. Therefore without further constraints, it is not possible to get the dip and moment separately from normal mode excitations. The near-field geodetic data shows an opposite trade-off. The shallower the fault dip angle, the smaller is the moment required for the measured displacements. Therefore, the fault dip angle can be constrained from adjusting the geometry and moment to fit both normal mode amplitudes and geodetic data.

In practice, for any prescribed dip angle, we constrained the moment to the value required to fit the normal mode amplitudes. Given that the CMT solution indicates a dip angle of 8^0 for the east dipping plane, we have tested dip angle values between 8^o and 12^o (Table 2.4). In order to accurately compute the very long period normal modes, we take into account the coupling caused by Earth's rotation, ellipticity and heterogeneities of earth structure (Dahlen and Tromp 1998; Park and Gilbert 1986). Following Park et al., (1986) we compute the normal mode spectrum, which includes 3D earth model (Ritsema, van Heijst and Woodhouse 1999) and a group-coupling scheme (Deuss and Woodhouse 2001). The result of this exercise is that for a dip angle of 12^0, the moment is 8.3×10^{21} N.m, for 10^0 it is 1×10^{22} N.m and for an 8^0 we get 1.24×10^{22} *N.m*. For each assumed dip angle we have computed source models derived from the inversion of the geodetic and teleseismic data. We have compared the quality of the fit to the geodetic data provided by each source model based on the reduced chi-square criteria defined as:

$$\chi_r^{\,2} = \frac{1}{n}\sum_{i=1}^{i=n}\left(\frac{(pred^i - ob^i)}{\sigma_i}\right)^2, \qquad (2.2)$$

where n is the number of geodetic data, σ_i is the uncertainty associated for the each measurement ob^i, $pred^i$ is the predicted displacement at site *i*. Our results show that the source model with a dip angle of 12^0 yields a higher reduced chi square (~21) compared to dip angle of 8^0 and 10^0 (~14). The moment required to fit the normal modes for a dip angle of 12^0 does not allow slip amplitudes large enough to explain the near-field coseismic displacements. Therefore, the average dip angle has to be less than 12^0.

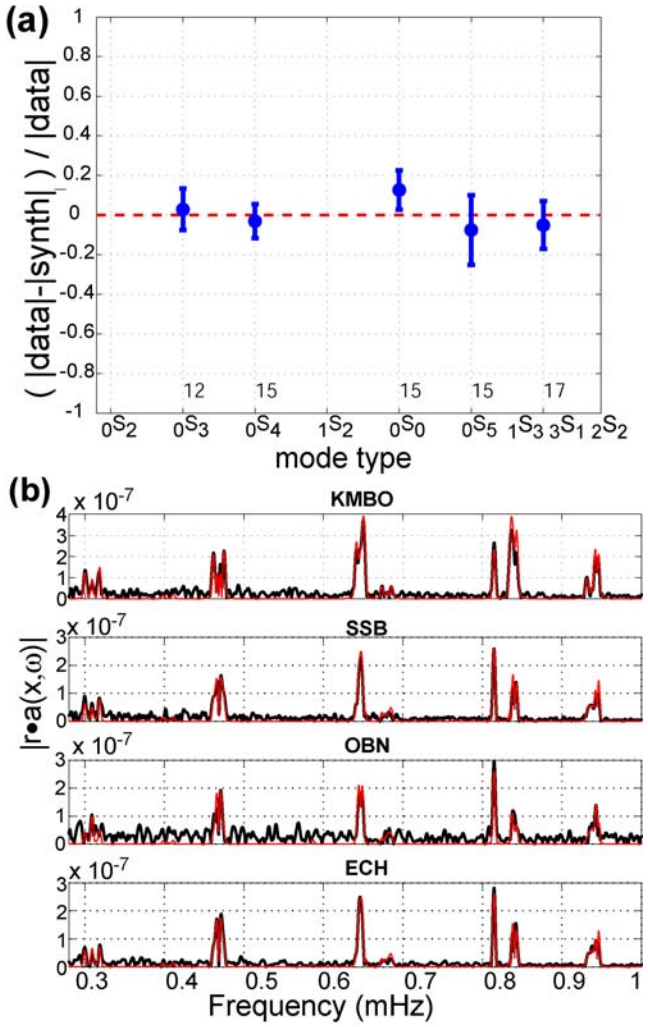

Figure 2.2: Prediction of Earth's normal modes for a finite fault model using teleseismic and geodetic data with dip angle of 10°, Mw 8.6, Vr from 1.5 to 2.5 km/s . (a) normalized amplitude difference between synthetics and normal mode data, calculated for spheroidal modes ${}_0S_3$, ${}_0S_4$, ${}_0S_0$, ${}_0S_5$, ${}_1S_3$-${}_3S_1$-${}_2S_2$. Number of stations used to calculate the misfit is given below. Data to noise ratio for ${}_0S_2$ and ${}_1S_2$ are too small to be analyzed extensively. (b) Normal

modes spectrum calculated for 4 stations with good signal to noise ratio; KMBO, SSB, OBN, ECH. Synthetics are shown in red and data in black.

The lower bound to the fault dip comes from geometrical considerations. Given the hypocenter of the earthquake, a dip angle of less than 8° would meet the earth surface at a considerable distance from the trench. Since the subducting plate's dip angle usually decreases trenchward, a dip of less than 8^0 is geometrically not plausible. In this study, we chose to use a dip of 10^0 and a moment of$1x10^{22}$ N.m. The corresponding fit to the normal mode excitations is shown in Figure 2.2.

2.6 Source Models Obtained from the Inversion of Teleseismic Waveforms and Geodetic Data

Since three different datasets are included in the inversion, we tested various solutions and combinations to understand the constraints provided by each particular dataset (Figure 2.3). In the source inversions shown in Figure 2.3, rupture velocity is allowed to vary from 1.5 km/s to 2.5 km/s and rise time for each sub-fault is between 2 s and 32 s. The rupture velocity range was determined by carefully examining misfits of a variety of rupture velocity solutions and will be discussed later. We also performed joint inversions in which the rupture velocity was fixed to some constant value.

The misfit between the measurement and synthetic waveforms is quantified by the sum of L1 and L2 norms

$$e_l = \sum_{j=j_{\min}}^{j=jc} w_j \cdot \left(\frac{1}{k_j} \sum_{k}^{k_j} \left| o_{j,k} - y_{j,k} \right| + \sqrt{\frac{1}{k_j} \sum \left(o_{j,k} - y_{j,k} \right)^2} \right), \qquad (3)$$

where $o_{j,k}$ and $y_{j,k}$ are the wavelet coefficients of the observed and synthetic seismogram for station k and wavelet index j, w_j are the weight of each wavelet channel (Ji, Wald and Helmberger 2002a) . The errors of waveforms are normalized by dividing the calculated error with the error calculated from a random model. The model obtained from the inversion of only the seismic data (Figure 2.3a) yields an error of 0.14. The fit to the waveforms is indeed quite good (Figure 2.4a). By contrast, this model provides a very poor fit to the geodetic data

(Figure 2.5a), while models utilizing both geodetic and seismic data (Figure 2.3c, 2.3d) fit geodetic data very well (Figure 2.5c, 2.5d). The misfit to the waveforms does not vary much when the geodetic data are taken into account (Figure 2.4b, 2.4c) and remains in the 0.15-0.20 range (Table 2.4).

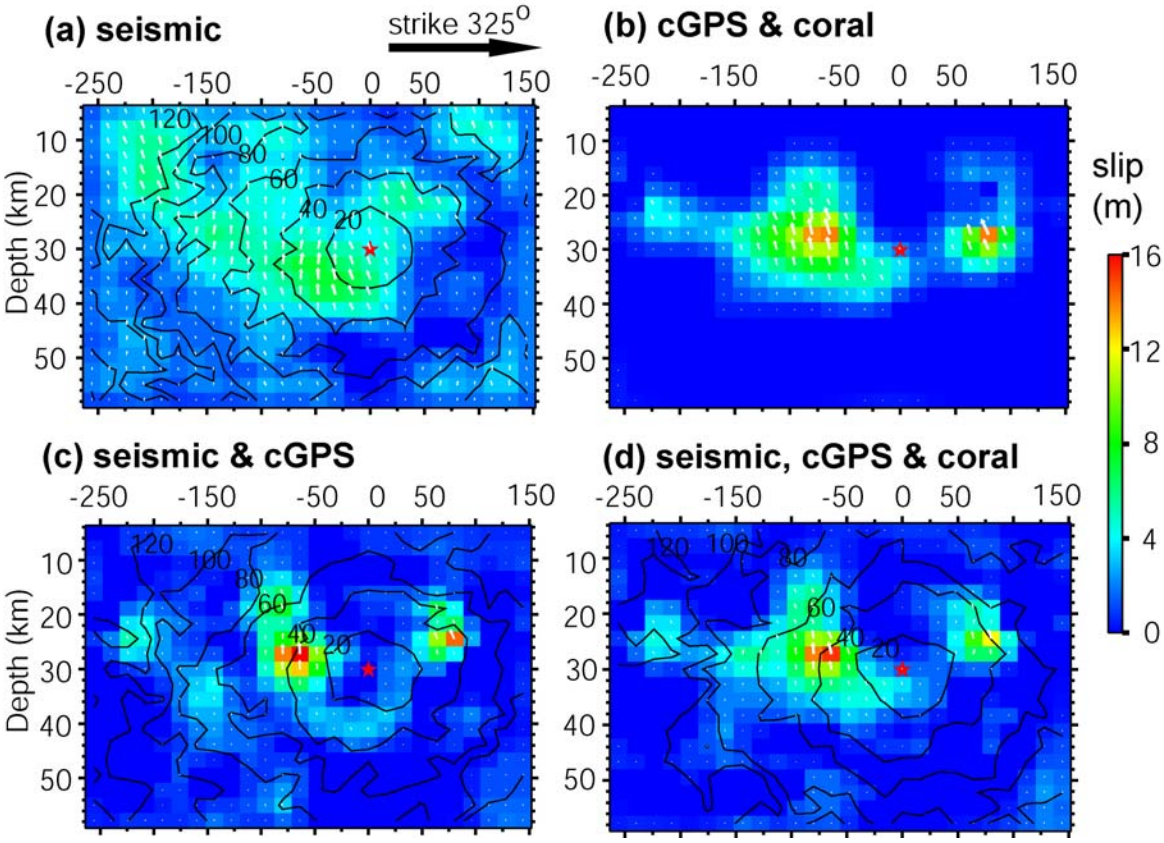

Figure 2.3: Slip distributions and 20-second contours of the rupture front for the various source models from the inversion of (a) teleseismic, (b) geodetic (cGPS and coral), (c) teleseismic and cGPS, (d) teleseismic and all geodetic data. Rupture velocity is allowed to vary between 1.5 and 2.5 km/s. White arrows show slip vectors for each sub-fault.

The geodetic inversion (Figure 2.3b) was performed with same smoothness and rake parameters as the seismic and joint inversions. Each geodetic measurement is weighted by the $1/\sigma^2$ error, where σ is the associated uncertainty for each cGPS component or coral measurement point. When only the geodetic data were considered in the inversion, we obtain a reduced chi-square of 5.2 (Table 2.3). This misfit larger than unity is due in part to a few points at which the residuals exceed notably the uncertainties on the geodetic measurements. The distribution of residuals show that most residuals are about 2 times the uncertainty but that two GPS stations, (BSIM and LHWA), contribute most to the misfit with residuals 5 to 10 times larger than the uncertainties on each component. If these two outliers are removed the reduced chi-square is close to 3. In fact, the weighted RMS on the misfits to the GPS horizontal measurement is about 0.45 cm, while assigned uncertainties are of the order of 0.2 cm, weighted RMS on the coral data is about 15 cm, similar to assigned data uncertainties. So either the uncertainties on the some GPS measurements with large displacements were underestimated or the model geometry is too simplistic. Approximating the ruptured fault by a single plane is certainly a poor approximation given the curved shape of the trench in the area and probable down-dip curvature of the plate interface. Because of the lack of detailed geophysical constraints on the fault geometry we hold to that approximation for simplicity.

The comparison of joint inversions (Figure 2.3c, 2.3d) with the purely seismic and geodetic inversions (Figure 2.3a, 2.3b) shows that the slip distribution is primarily constrained by the geodetic data. Although the joint inversion models are quite different than the pure teleseismic inversion model in terms of slip distribution, the fit to the waveforms is almost equally good (Figure 2.4, Table 2.4). This result emphasizes the non-uniqueness of the solution when only the teleseismic data is used, and the importance of bringing in near-field geodetic constraints, especially for large megathrust earthquakes. Both joint inversions (Figure 2.5c, 2.5d) show two high slip patches beneath Nias and Simeulue islands respectively, with a slip deficiency around the hypocenter. The addition of coral data into the joint inversion provides a better spatial coverage and yields a smoother slip distribution (Figure 2.5d) compared to the model derived from the teleseismic and cGPS data (Figure 2.5c). This shows that slip patches are biased by the distribution of GPS stations without addition of coral data.

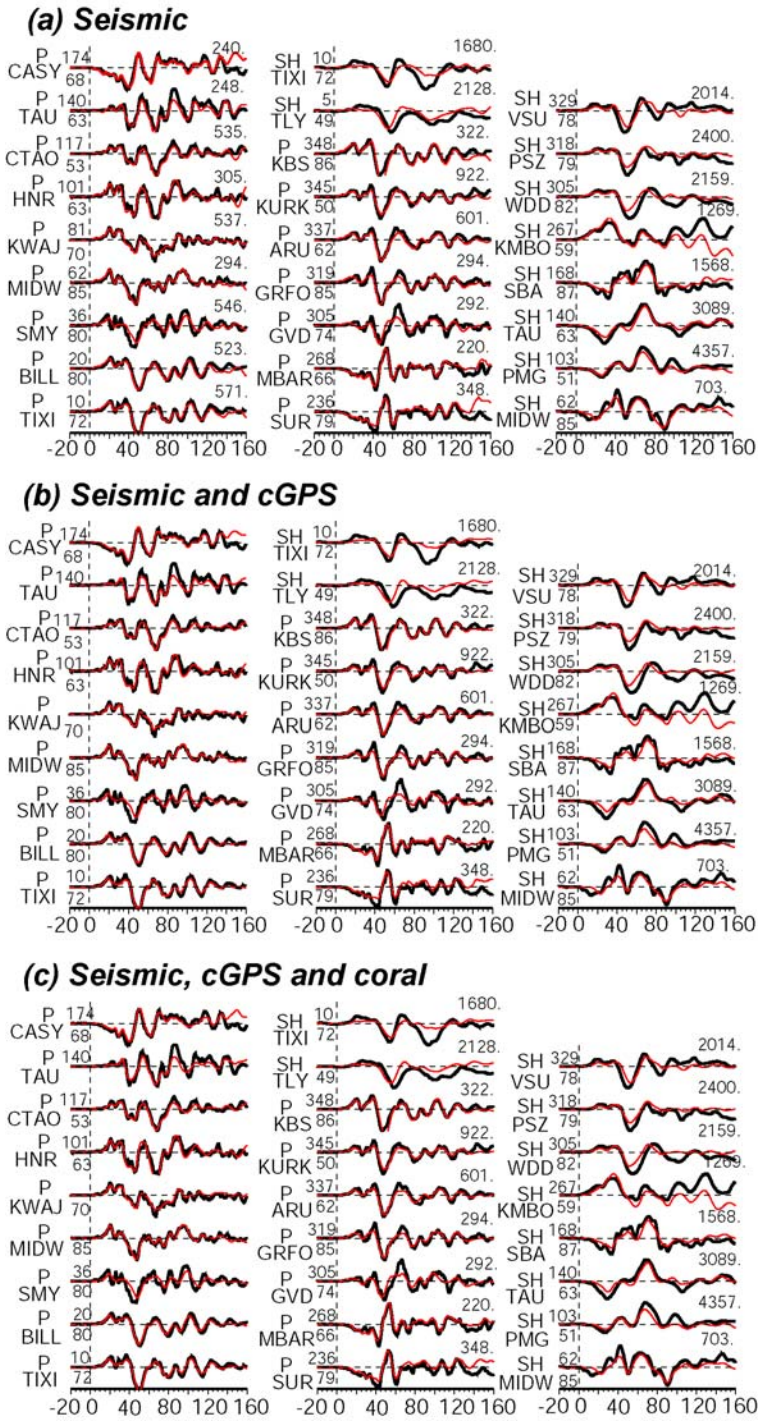

Figure 2.4: Observed (black) and synthetic (red) teleseismic P and SH waveforms. Station name, azimuth and distance are indicated on the left of each trace. The maximum displacement is shown at the top right of each trace in microns. (a) teleseismic, (b) teleseismic and cGPS, and (c) joint inversion of teleseismic and all geodetic data.

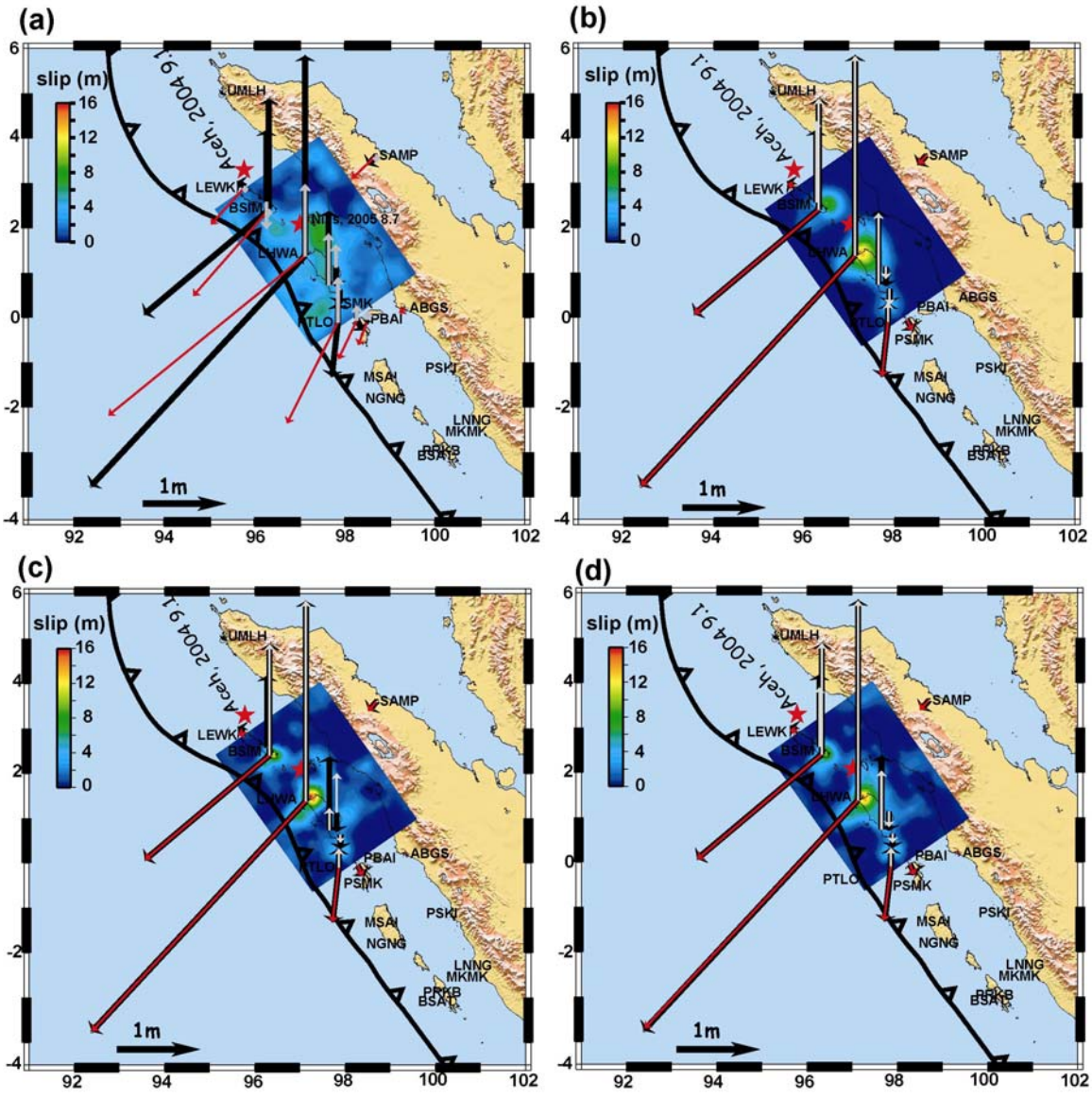

Figure 2.5: Fits to the 16 cGPS and 4 coral measurements of uplift for the inversions shown in Fig 2.3. The slip on the fault is also shown in the maps. The data is in black, the horizontal fits are in red and vertical fits are shown in gray. (a) teleseismic, (b) geodetic, (c) teleseismic and cGPS, and (d) joint inversion of teleseismic and all geodetic data

The predicted uplift from these models, along with the coral uplift measurements are shown in Figure 2.6. Note that the inversion of teleseismic data alone yields a model which seems inadequate to fit the measured pattern of uplift (Figure 2.6a). This model predicts high uplift very close to the trench which is not compatible with the modest tsunami produced by this earthquake. Geodetic and joint inversions (Figure 2.6b, 2.6c, 2.6d) show that the largest uplift is on the northwest of Nias Island, where the cGPS station LHWA recorded about 3 m of uplift and 4.3 m of horizontal displacement toward the trench (Figure 2.1). The models derived using both the cGPS and the coral data (Figure 2.6b & 2.6d) show a more elongated uplift pattern along western Nias Island, while the model using cGPS and seismic data predicts a more circular pattern centered at near LHWA, the GPS station with the highest displacement. This shows that the spatial coverage of the coral uplift data helps resolve the shape of the asperity. Another advantage of implementing the coral data into inversions is to constrain the pivot line cutting through the southeast of Nias Island.

In Figure 2.7, the rupture velocity is fixed to 1.5, 2, 2.5 and 3 km/s and the corresponding slip distributions and rise times are shown in panels (a) (b), (c) and (d), respectively. The rise time was allowed to vary from 0 to 32s in these inversions. Even with the simple cosine function with one parameter used to characterize the time evolution slip, the model fits the waveform data quite well for a variety of rupture velocities (Figure 2.7). We observe a direct trade-off between the rupture velocity and rise time since they are closely linked as indicated by equation (1), especially in the largest asperity under Nias Island. In the model with v_r = 2 km/s, the rise times $S(t)$ are mostly between 10 s and 20 s, whereas in the model with v_r=3km/s, rise times are ~25s or greater. If the slip amplitudes were not constrained by the near-field geodetic data, the trade-off between rupture velocity and rise times would be more obscure, since slip amplitudes would also be trading-off with these parameters.

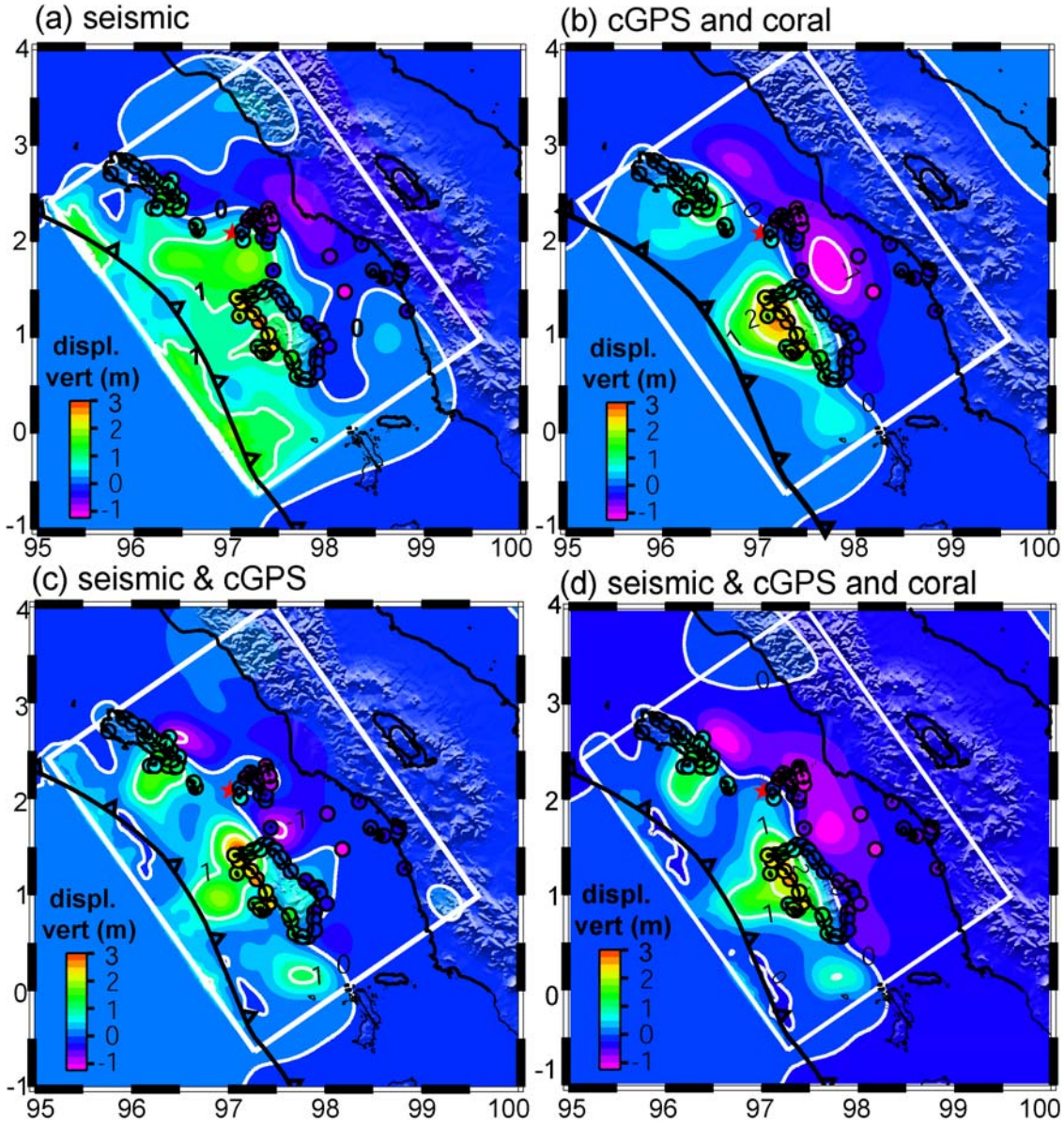

Figure 2.6: Uplift distribution predicted from the source models obtained from the inversion of (a) teleseismic, (b) geodetic (cGPS and coral), (c) teleseismic and cGPS, and (d) teleseismic and all geodetic data. The measured vertical displacements are also shown in same color scale (circles). Predicted pivot line (line of zero elevation change) is plotted in white and it separates the uplift from the subsidence.

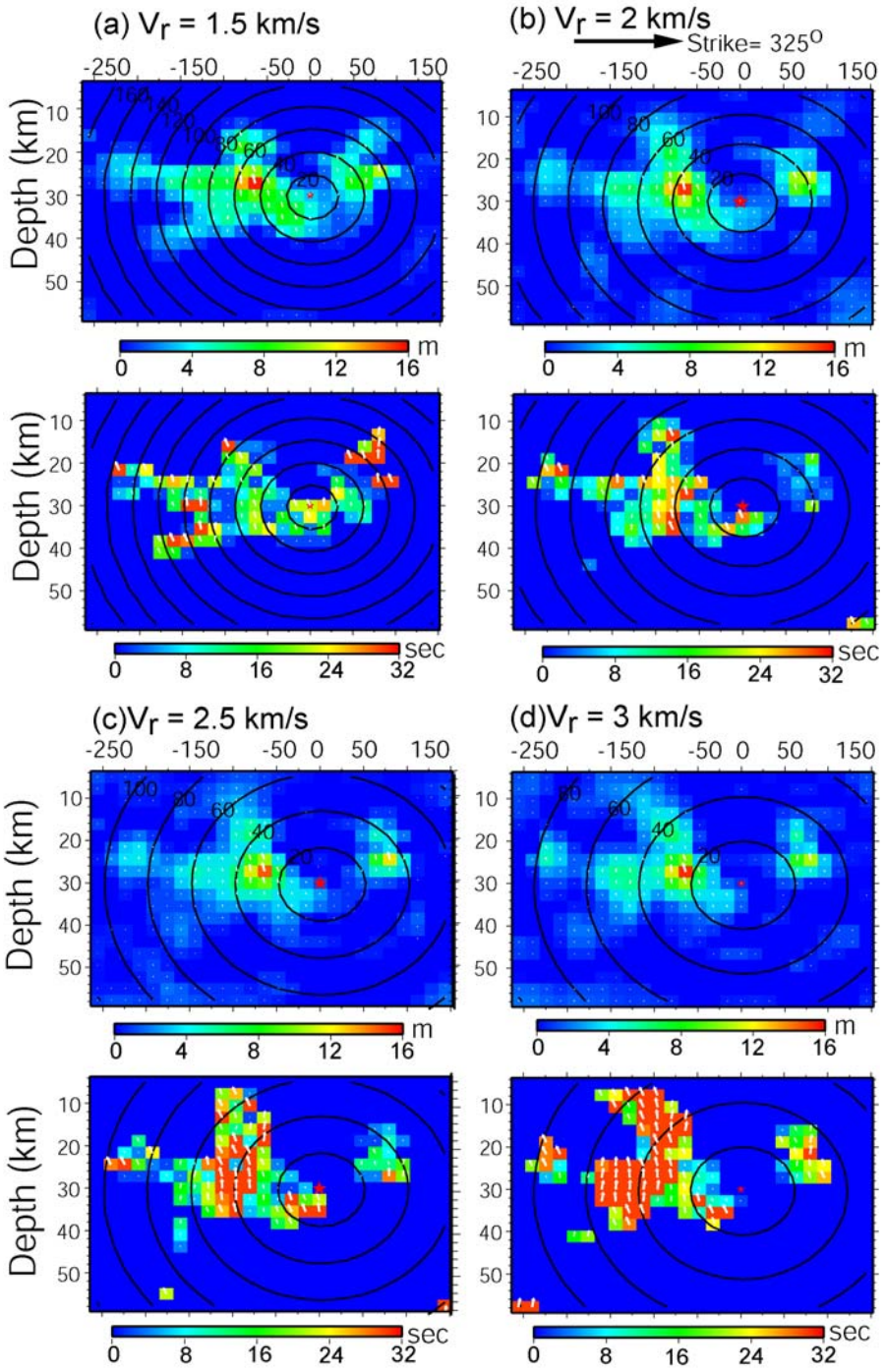

Figure 2.7: Slip and rise time distributions on the fault for inversion with (a) v_r=1.5km/s, (b)) v_r=2 km/s, (c) v_r=2.5 km/s, and (d) v_r=3 km/s. Rise times are shown for the sub-faults that slip more then 2 meters, since the ones that slip less can not be constrained reliably. The rupture front contours are drawn for every 20 seconds.

The fit to seismic waveforms are slightly better for the case where rupture velocity is fixed to 2 km/s compared to the cases where it is fixed to some higher or lower value. The fits to the geodetic data on the other hand get better with decreasing rupture velocity (Table 2.4).

Table 2.4 | Characteristics of source models and errors

Dataset	**dip**	**Vr (km/s)**	**Rise time (s)**	**Moment Magn.**	**Waveform misfit****	**Geodetic mistfit(χ_r^2)*****
Seismic	10	1.5-2.5	2-32	8.6*	0.14	12684.0
cGPS & corals	10	1.5-2.5	---	8.6*	--	5.21
Seismic, cGPS	10	1.5-2.5	2-32	8.6*	0.17	77.4
Seismic, cGPS & corals	10	1.5-2.5	2-32	8.6*	0.175	11.8
Seismic, cGPS & corals	10	1.5	2-32	8.6*	0.232	5.4
Seismic, cGPS & corals	10	2.	2-32	8.6*	0.189	12.1
Seismic, cGPS & corals	10	2.5	2-32	8.6*	0.191	13.3
Seismic, cGPS & corals	10	3.	2-32	8.6*	0.204	13.3
Seismic, cGPS & corals	10	2-2.5	2-32	8.6*	0.175	15.0
Seismic, cGPS & corals	10	1.5	2-32	8.74	0.182	19.4
Seismic, cGPS & corals	10	2	2-32	8.71	0.171	16.5
Seismic, cGPS & corals	10	2.5	2-32	8.64	0.183	12.1
Seismic, cGPS & corals	10	3.	2-32	8.62	0.202	14.6
Seismic, cGPS & corals	8	2-2.5	2-32	8.66*	0.174	14.4
Seismic, cGPS & corals	12	2.-2.5	2-32	8.55*	0.181	21.3
Seismic	15	1.5-2.5	2-32	8.80	0.150	12923.0
cGPS & corals	15	---	---	8.59	--	14.6
Seismic, cGPS & corals	15	1-3	10	8.64	0.169	18.4

*moment is constrained to the given value a priori in the source inversion.

** The waveform misfits are a combination of L1 and L2 norms (Ji et al., 2002).

***The fit to the geodetic data is quantified from the reduced Chi-square as defined by equation (2.2).

2.7 Testing the source models against long period surface waves

In spite of the constraints provided by the geodetic data, there are still some trade-offs among the model parameters, and we are left with several models that fit the data nearly equally well (Table 2.4). Since long-period surface waves were not utilized to constrain the inversions, they can be used to constrain further the range of viable models. To account accurately for the 3D structure, ellipticity, gravity and rotation, we use a spectral element method (SEM) (Komatitsch and Tromp 2002a; Komatitsch and Tromp 2002b) to compute synthetic waveforms. We use the 3D crustal model Crust 2.0 (Bassin, Laske and Masters 2000) and the 3D mantle model s20rts (Ritsema, van Heijst and Woodhouse 1999). Each sub-fault is inserted as a separate source with the mechanism, amplitude, timing and rise time determined by the source inversions (Tsuboi et al., 2003).

All of the models fit the long periods (100-500 s) reasonably well (Figure 2.8). To quantify the fit, we use the cross-correlation between the data and synthetics in the 400-second window centered on the Rayleigh waves. Synthetics computed using fixed rupture velocity models have cross-correlation values averaging around 0.97 with better fits in some azimuths. Thus, our models based on relatively short-period teleseismic data and static offsets are very compatible with the seismic data in the 100-500 s period range.

In the source inversions, the trade-off between the rupture velocity and rise time depends on the apparent velocity of the modeled phase. The apparent velocities of Rayleigh waves are about one-third of the P waves. As the models with different kinematic parameters were made to fit the P and S waves, there will be a phase shift of the Rayleigh waves depending on the rupture velocity. If the hypocenter is well located, and correct rupture velocity is used, there should be no time shift between the data and synthetics. Rupture velocities of 2-2.5 km/s give the least average travel-time shifts relative to the 3D model in order to align the waveforms (Figure 2.8 inset).

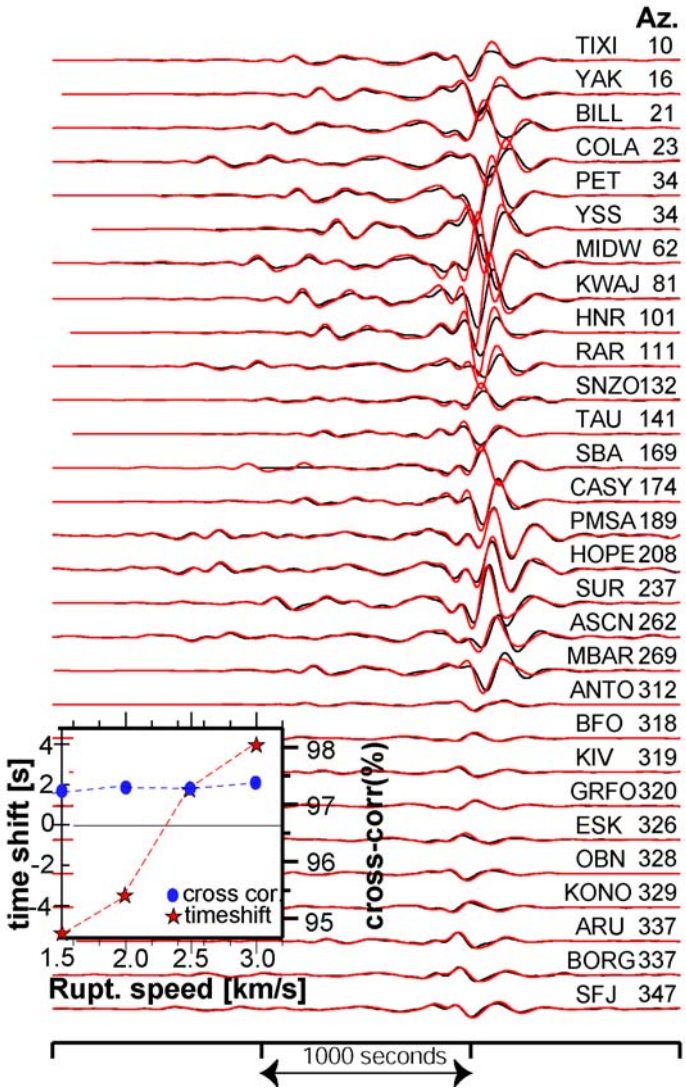

Figure 2.8: Fits to100-500 s band-pass filtered waveform fits computed using a 3D spectral element method for the model with fixed rupture velocity of 2.5 km/s (Figure 7c). The seismograms are 30-100 degree distance and are sorted by azimuth and aligned on the Rayleigh wave (3.8 km/s phase velocity). The inset shows the cross-correlation values (blue circles) and time shifts (red stars) of the Rayleigh waves for the fixed rupture velocity models of 1.5, 2.0, 2.5 and 3.0 km/s.

2.8 Strong Motion Estimates

We use the source models described above to estimate the ground motion in the near-field, specifically at the location of the GPS motion LHWA which lies above the largest asperity. To obtain detailed information about the rupture process requires near-field seismic data of the type observed for the well-studied 1999 Chi-Chi earthquake. Its strongest motions were recorded near the famous bridge failure, with horizontal offsets of 8 m and uplift of 4.5 m. These offsets occurred in a few seconds and were produced by the nearest small patch of high slip close to the surface. Peak velocities of up to 280 cm/s were observed and successfully modeled (Ji, Helmberger and Wald 2003). For the Nias-Simeulue event we measured 4.5 m horizontal displacement and 2.9 m uplift at the station LHWA, about half of the motion recorded during the Chi-Chi earthquake (Figure 2.1).

Prediction of the temporal behavior at this location is displayed for our source models in the frequency range of 1Hz to 5 mHz in Figure 2.9. The final horizontal displacements in Figure 2.9(a) is reached after 60 s because nearly the entire fault contributes to the final displacement. The vertical displacement is not monotonic because slip in each cell on the megathrust contributes differently to uplift at LHWA. Slip on cells east of the site produce subsidence, while slip on cells west of the site produce uplift. Thus a smaller portion of the fault is responsible for net uplift to sharper offsets and large vertical velocities. The slight difference between the predictions by cGPS-only model and the model that uses both the cGPS and the coral data in Figure 2.9(a) is caused by the small difference in location of the pivot line in the two models. Figure 2.9(b) shows the various models calculated with models where rupture velocity is fixed to 1.5, 2, 2.5 and 3 km/s, respectively.

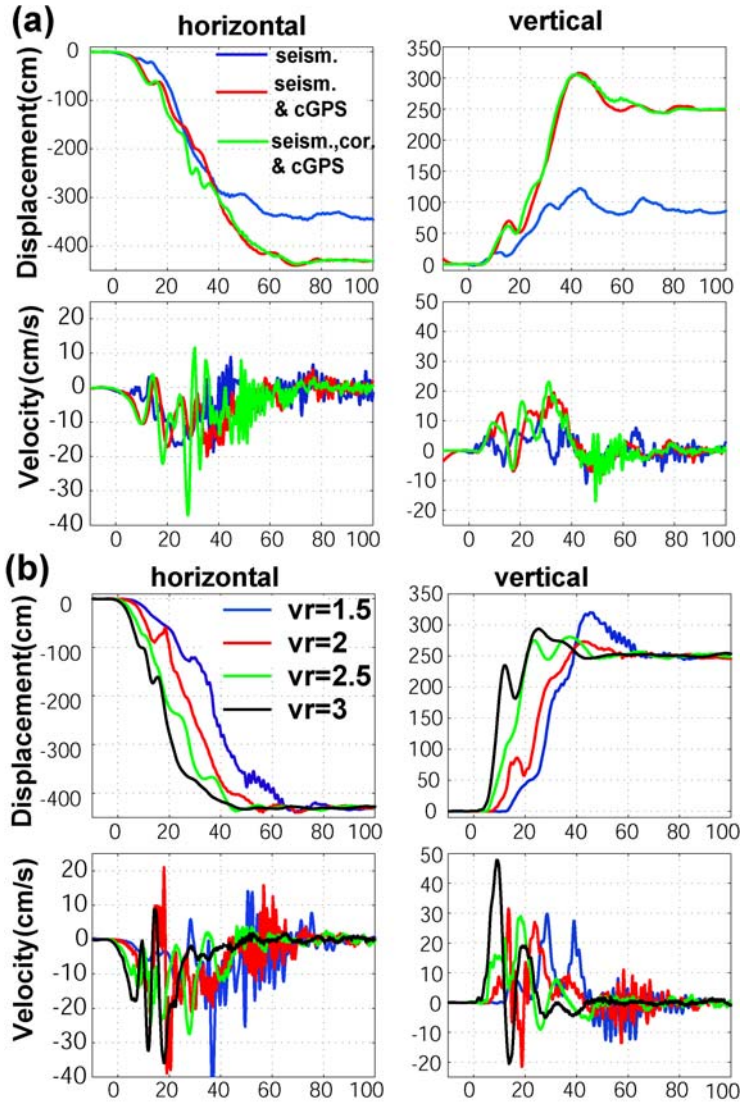

Figure 2.9: The estimated time evolution of ground displacement and velocity at the station Lahewa (LHWA), Nias Island, for various inversions. (a) Predictions for seismic and joint inversions with GPS and all coral data for rupture velocity varying 1.5-2.5 km/s. (b) Predictions for joint inversions for fixed rupture velocities of 1.5, 2.0, 2.5 and 3.0 km/s.

The strong-motion predictions show considerable variation, but all models produce relatively weak strong-motions. The largest velocity pulses (~45 cm/s) are obtained when the rupture velocity is fixed to 3 km/s; however, this rupture velocity is an extreme upper bound

for this earthquake. Figure 2.9b shows that frequency content of the prediction of ground motion changes depending on the assumed rupture velocity. This is a result of trade-off the between the rupture velocity and rise time discussed above. For the higher rupture velocities, the rise times are longer, creating more long period near-field pulses, and for lower rupture velocities, rise times are shorter, creating local high frequency data.

2.9 Discussion

In this study we attempted to construct a fault-slip model for a great earthquake that explains a wide range of datasets. Each dataset provides key constraints, but lacks the individual strength to break the many trade-offs. In this section, we will go over the issues that are investigated in this study and summarize the findings and associated constraints and limitations. For clarity, we have divided this section into four subsections, even though they are all closely related – fault geometry, slip distribution, rupture velocity and rise time, and evaluation of near-field strong ground motion.

2.9.1 fault geometry

The existence of geodetic data along with normal mode data leads us to estimate the fault dip angle to be around 8^{o}-10^{o} with corresponding moment magnitudes of 8.66 to 8.60, respectively. However, the amplitude of normal mode excitation depends on the moment and hence on the rigidity structure on the fault. Since we are approximating the subduction zone structure by a 1D velocity model, our estimates of dip angle and moment can be biased. The excitation of long period seismic waves is even more complex if it is on a structural discontinuity, which is the case for most faults (Woodhouse 1981).

It should also be noted that fault dip is more likely to increase with depth; therefore, searching for a best-fitting constant dip angle is only a first order approximation, but it seems a very reasonable assumption in views of the plate interface geometry just north of Simeulue derived from the local monitoring of aftershocks of the 2005 Sumatra earthquake (Araki et al., 2006). In addition, Hsu et al. (2006) have explored the influence of the assumed fault geometry, using both curved and planar fault geometries adjusted to the position of the trench and to the aftershock distribution, and found that the sensitivity on the slip distribution is

insignificant. A constant dip angle is thus probably a reasonable assumption in this study. Further studies of aftershock relocations using near-field and regional data can help to constrain the velocity structure and geometry of the subduction zone.

2.9.2 Slip Distribution

Our study shows the importance of incorporating geodetic data to predict the slip distribution with accuracy. The comparison of the distribution of uplift predicted from the source model based on the teleseismic data (Figure 2.6a) with those predicted from the other source models makes this point clear (Figure 2.6c-2.6d). For very large earthquakes like the Nias-Simeulue event, it is a challenge to resolve the slip with only teleseismic data due to trade-offs. Near-field seismograms would prove very valuable to resolve these trade-offs to get a better slip distribution and kinematic parameters with seismology only.

The source models obtained from the joint inversion of the seismological and geodetic data all show that the slip distribution tapers to zero very rapidly up-dip of the slip patches beneath Nias and Simeulue islands. The upward termination of the rupture down-dip of the trench is probably due to inhibition of seismic rupture by the poorly lithified sediments at the toe of the accretionary prism (Byrne, Davis and Sykes 1988). Hsu et al., (2006) showed that the largest after-slip was observed at the upward termination of the coseismic rupture.

One of the most significant features of the slip pattern is the saddle in slip values between Nias and Simeulue and in the vicinity of the Banyak Islands (Figure 2.5). This saddle clearly separates the slip patch to the northwest, near Simeulue island, from that to the southeast, under Nias island. The approximate coincidence of the slip saddle with a major break in the hanging wall block of the megathrust is intriguing. Batee fault has been mapped in this vicinity based on seismic reflection profile, cutting across the forearc from south of the Banyak islands to the northern tip of Nias (Karig et al., 1980). They judged the right-lateral strike-slip offset of the continental margin across the fault to be about 90 km. (Sieh and Natawidjaja 2000) speculated, on the basis of bathymetric irregularities, that the fault continued in the offshore immediately north of Nias to the trench. Thus, it is plausible that the two principal patches of the 2005 earthquake are separated by a structural break in the forearc.

Whether this structure involves the megathrust itself, is unknown. But the coincidence of the proposed structure and the division of the 2005 rupture suggests the possibility that the megathrust has a tear or kink between Simeulue and Nias (Briggs et al., 2006). (Newcomb and McCann 1987) proposed, on the basis of field and tsunami reports, that the M_w 8.3-8.5 February 16, 1861, earthquake rupture extended from the equator to the Banyak Islands. If so, the southern Nias patch of the 2005 earthquake would be a rough repetition of the 1861 rupture. This has not yet been confirmed by paleoseismic work, but if true would provide an interesting contrast to the behavior of the 2005 Nias-Simeulue rupture, which started beneath the Banyak Islands and propagated bilaterally.

2.9.3 Rupture Velocity and Rise Time

Figure 2.10 summarizes the results that we obtained by varying the rupture velocity in joint inversion source models and the associated (a) geodetic misfit, (b) teleseismic waveform misfit, and (c) Rayleigh wave cross-correlation time shifts. The geodetic misfit gets lower for the lower rupture velocities. The rupture velocity of 1.5 km/s actually yields the best fit to the geodetic data (Figure 2.10a). Teleseismic data, on the other hand, are best adjusted for the 2-2.5 km/s rupture velocity range (Figure 2.10b). Rayleigh wave time shifts also favor a rupture velocity in the 2-2.5 km/s range (Figure 2.10c). An average rupture velocity of 3 km/s can be discarded, since it does not fit any of the datasets considered. Therefore we conclude that average rupture velocity has to be less than 2.5 km/s to be consistent with the observations.

The major difference between the slip models with different rupture velocities is that as the rupture velocity is fixed to a lower value, the portion of the fault plane around the hypocenter accumulates more slip. It is the difference in slip amplitudes near the hypocenter that leads to a better fit to the geodetic data for the case of v_r=1.5 km/s. Hence the observation that the model that best fits to the geodetic data has a slower velocity (1.5 km/s) than the models adjusted to the seismic data (2-2.5 km/s) suggests a non-uniform rupture velocity that starts slow at 1.5 km/s and then accelerates to 2.5 km/s. Nevertheless the average rupture velocity is in the range of 1.5-2.5 km/s.

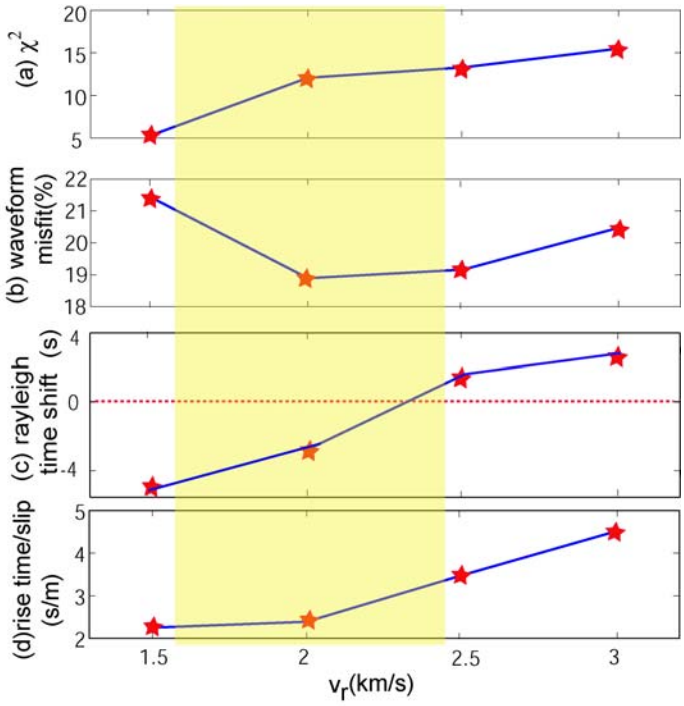

Figure 2.10: The fits of the fixed rupture velocity joint inversion models to the datasets and the plausible ranges for the dataset. (a) Geodetic misfit (χ^2) for the various fixed rupture velocity joint models. (b) Teleseismic waveform misfit. (c) Average Rayleigh wave cross-correlation time shifts in 300-500 s range. (d) Average time consumed for a 1 m slip to occur on the fault. The average value is calculated for all the subfaults that rupture 5 m or more. The plausible range of parameters is shown by the yellow rectangle.

Our estimate of rupture velocity is consistent with the average rupture velocity of 2.4 km/s inferred from the azimuthal variation of T-waves recorded at Diego Garcia in the Indian Ocean (Guilbert et al., 2005). A more detailed modeling of kinematic parameters requires more near-field strong-motion seismograms.

In Figure 2.10d, we report the average rise time for 1 m of slip as a function of assumed rupture velocity. For the plausible range of rupture velocities, this number is of the order of 2-3 s, showing that the rise times associated with this earthquake were relatively long. For the areas that slipped 10 m, the rise time is at least 20 s. For a comparison, the best observations of strong-motions during a large subduction earthquake are for the 2003 M_w 8.1 Tokachi-oki earthquake. The modeling of this earthquake from the near-field strong-motion seismograms

shows rise times of about 20 s and a maximum slip of 7 m for the largest asperity closest to the strong-motion stations (Honda et al., 2004) and about 10 s on the deeper part of the fault (Yagi 2004). The rise times are not as well constrained for the 2004 M_w 9.2 Aceh-Andaman earthquake; however, the seismic inversions show that the rise time functions might be even longer, over 30 s, for the largest asperity, which slipped 20 meters (Ammon et al., 2005). The typical rise times for continental events are generally estimated to be a few seconds (Heaton 1990). The best constrained continental earthquake is probably the 1999 M_w 7.6 Chi-Chi earthquake, for which abundant geodetic and near-field seismic data exist. The rise times from the largest two asperities of the Chi-Chi earthquake are only about 3 s (Ji, Helmberger and Wald 2003) despite co-seismic slip in excess of 12 m, as constrained from GPS and satellite imagery data (Yu 2001). The general observation of long rise times for slip during subduction megathrust earthquakes and rapid rise times during continental earthquakes may reflect a fundamental difference of frictional properties.

2.9.4 Evaluation of near-field strong-motion

Using the finite source models, we estimate ground motions in the 1 Hz to 5 mHz frequency band at the GPS site that had the greatest measured ground displacement, LHWA (Figure 2.9). Within the bounds of plausible rupture velocities and rise times, maximum particle velocities in the Nias-Simeulue earthquake are between 20 and 30cm/s, an order of magnitude lower than for the 1999 Chi-Chi earthquake. These values are compatible with near field recordings of strong-motions from earlier smaller subduction zone events. The peak ground velocity reported from the M_w8.1 Michoacan earthquake is about 20 cm/s (Anderson et al., 1986). The highest observed ground velocity, filtered lower than 1 Hz from the Tokachi-oki earthquake is higher — ~66 cm/s (Yagi 2004). Most of the stations for the Tokachi-oki earthquake are close to the down-dip end of the rupture, implied by negative vertical displacements on seismograms. Therefore the strongest motions could be higher than the ones recorded. It should be noted that despite the long rise times, the rupture velocity for the Tokachi-Oki earthquake is estimated to be 4.4 km/s (Yagi 2004), a much higher value than our estimations for the Nias-Simeulue earthquake, leading to higher observed ground motions. These conflicting results emphasize the importance of rupture velocity is in determining the amplitude of the near-field motions in the subduction events.

There are several factors which may have contributed to the relatively low particle velocities during the Nias-Simeulue earthquake. First is the purely geometrical difference between the Nias-Simeulue and Chi-Chi cases. The 6-second displacement pulse observed on the ground in the Chi-Chi earthquake occurred within a few kilometers from the rupture, whereas the 60-second displacement at LHWA during the Nias-Simeulue earthquake occurred about 20 km above the megathrust. Thus, the rise time at Chi-Chi was dominated by a small part of the fault immediately adjacent to the station at which the rise time was measured; but the pulse duration at LHWA during the Nias-Simeulue earthquake is an integrates affect of a larger (150 km by 30km) patch of rupture of the megathrust.

Another reason for the long rise time at LHWA is the low rupture velocity and long rise time on individual cells. If the rupture velocity was about 80% of the shear velocity and also the rise times were similar to Chi-Chi earthquake (~6 s on the big asperities), the predicted value of the peak particle velocity would reach 80 cm/s.

Yet another reason for the slow rise time at LHWA is the radiation pattern and rupture directivity. For crustal strike slip faults, directivity is known to be a major factor determining the amount and distribution of damage. In subduction zone earthquakes, rupture propagation is commonly toward the trench and along strike. The islands are above the slipping region. Therefore, the islands are not in the direction of the rupture, and consequently experience lower peak ground motions. However, even at the trench, our calculations show weak velocity pulses, since the trench is quite far away from the large offsets. A more detailed study of the strong-motions from great subduction earthquakes and their dependence on kinematic parameters requires near-field strong-motion seismograms.

2.10 Conclusions

The dip angle and seismic moment of the Nias earthquake is estimated to be 8^o to 10^o with corresponding moments of 1.24×10^{22} to 1.00×10^{22} N.m using moment and dip constrains from normal mode data and geodetic misfits. Despite the significant trade-offs between rise time and rupture velocity, the slip pattern of the Nias-Simeulue event is quite well determined, due to the constraints on moment and unique abundance of geodetic data above the source region.

Our analysis implies that the earthquake was caused by the rupture of two asperities which did not have significant slip near the trench. A big patch under northern and central Nias island, with maximum slip of about 15 m, a smaller patch under southern Simeulue island, and a slip gap between the two islands are common features of all our joint inversions (Figure 2.5). We estimate kinematic parameters by minimizing the time shift in the long-period seismograms and misfit to the dataset used in the inversion. We favor an average rupture velocity of 1.5 to 2.5 km/s (Figure 2.3d). If this is correct, then the rupture velocity is only 50%-60% of the shear wave speed of the 1D model, far lower than rupture velocities seen during the Chi-Chi and Tokachi-oki earthquakes, for which rupture velocity was typically about 80%-90% of the shear wave speed. Our modeling yields rise times for the Nias-Simeulue earthquake between 10-15 s, which is similar to other large subduction zone earthquakes.

2.11 Acknowledgement

My collaborators in this study were Vala Hjorleifsdottir, Teh-Ru Alex Song, Jean-Philippe Avouac, Don V. Helmberger, Chen Ji, Kerry Sieh, Richard Briggs, Aron Meltzner. This manuscript has benefited from helpful suggestions and comments by our reviewers, Roland Burgmann and David Wald.

Chapter 3: The 2007 Mentawai Earthquake Sequence on the Sumatra Megathrust : on Barriers and Cooperation Among Seismic Asperities

3.1 Abstract

On September 12, 2007 an M_w 8.4 earthquake followed by an M_w 7.9 event 12 hours later ruptured the Sumatra megathrust in the Mentawai Islands area. The joint analysis of geodetic and seismological data reveals the sequence ruptured a set of distinct asperities extending over the rupture area of the 1833, M_w 9.0 historical earthquake. The cumulative released moment amounts to only a fraction of that released in 1833, as well as of the deficit of moment that had accumulated since 1833 as a result of interseismic strain. This study shows the influence of permanent barriers on the extent of large megathrust ruptures, which can be a cause of some regularity of the seismic behavior, but also that the same portion of a megathrust can rupture in different patterns depending on whether asperities break as isolated seismic events or cooperate to produce a larger rupture. This variability arises probably mostly from the influence of non-permanent barriers, probably zones with locally lower pre-stress due to the past earthquakes. This mechanism has been quite effective at preventing the earthquakes of 2007 to grow as big as the previous historical events. The state of stress on that portion of the Sumatra megathrust was not adequate for the development of a single major large rupture at the time of this seismic crisis. However, the slip deficit that has accumulated since the 1833 and 1797 events remains large, and so is the potential for a large megathrust event in the Mentawai area.

3.2 Introduction

The 2004 M9.2 giant earthquake which ruptured the Sunda subduction zone from northern Sumatra to the north Andaman Islands came as a reminder of our poor understanding of the seismic and tsunami hazards related to subduction zones (Ammon et al., 2005) (Chlieh et al., 2007; Lay et al., 2005; Subarya et al., 2006). The interplate motion across a subduction zone can be taken up by either aseismic slip or seismic slip (where slip at a given

point of the interface occurs during seismic events characterized by duration of seconds to minutes, and a sliding velocity of typically a few km/s) (Ruff and Kanamori 1983). Aseismic slip dominates at depths greater than about 40 km (Pacheco, Sykes and Scholz 1993), but both modes of slip contribute at shallower depths leading to heterogeneous stress build up in the interseismic period (Dmowska and Lovison 1992). The analysis of geodetic and paleogeodetic measurements of interseismic strain suggests that the Sunda megathrust indeed consists of a patchwork of creeping and locked areas (Chlieh et al., in press); Figure 3.1). The large patches that remain locked are presumably the areas where large interplate earthquakes rupture (Burgmann et al., 2005; Suwa et al., 2006). For example, strong coupling is observed in the rupture area of the 2005, M_w 8.7, Nias earthquake (Briggs et al., 2006; Konca et al., 2007), a patch that had already ruptured in 1861 in an event similar to that of 2005 (Newcomb and McCann 1987). Coupling is low in the Batu Islands area (around the equator), where only moderate earthquakes are known to have occurred, and high in the Mentawai Islands area (between about 2º S and 5º S), where M > 8.7 earthquakes occurred in 1797 and 1833. These observations indicate that the pattern of interseismic strain accumulation determines the characteristics of large megathrust ruptures to some degree. Nonetheless, it is clear that successive earthquakes in the same area often differ in terms of their rupture extent and magnitude (Thatcher 1990) and that the relationship between co-seismic strain release and interseismic strain might not be that simple. The recent sequence of large earthquakes which occurred in the strongly coupled Mentawai Islands area that had produced M_w ~9 earthquakes in 1833 and 1797, is an illustration of this. As detailed below, this sequence released a moment much smaller than that was released in the previous historical events and did not release much of the deficit of moment that had accumulated since then.

Hereafter, we describe in detail the September 12, 2007 sequence of earthquakes which started with an M_w 8.4 event, followed by an M_w 7.9 12 hours. We use a variety of geodetic data (GPS measurements, field measurements of uplift, SAR interferometry), and seismological records to derive finite-source models. We finally discuss the following outstanding questions: How does the pattern of a megathrust that is locked during the interseismic period compare with the rupture area of large earthquakes? How does co-seismic slip compare with slip deficit accumulated during the interseismic period? How similar are successive large interplate eartquakes that rupture the same area of a megathrust?

3.3 Datasets

3.3.1 GPS Data

The earthquake sequence occurred well within the area monitored by the continuously recording GPS stations of the Sumatra Geodetic Array (SuGAr). The sampling rates, 1 second at 3 stations and 120 seconds at all other stations, make it possible to distinguish the co-seismic displacements attributable to the various major shocks. Inspection of the time series show significant displacements at most stations at the time of the 8.4 and 7.9 on September 12. A major M_w 7.0 aftershock occurred near southern Sipora Island about 16 hours after the M_w 8.4 mainshock and also caused measurable displacements on September 13 at a subset of local stations (PKRT, PPNJ). The displacements assigned to each event, and their cumulative effects were determined from 120 seconds time series. The cumulative displacements can be estimated more accurately than those assigned to the individual events due to the short period of time separating the events (12 hours and 4 hours).

All horizontal displacements are trenchward (Figure 3.2). The maximum cumulative horizontal displacement, 1.5 m, was measured at station BSAT on South Pagai Island. Except at the few stations where the effect of the 7.0 event was significant, the co-seismic displacement associated with the 8.4 and 7.9 earthquakes add, within uncertainties, to the cumulative displacement derived from daily solutions. The time series show no clear pre-seismic signal, besides that related to interseismic strain, and a clear postseismic signal analogous to that observed following the M_w8.6 Nias-Simeulue earthquake (Hsu et al., 2006). Horizontal displacements accrued by up to 50% in the month following the mainshock, but the largest stations (BSAT, PRKB) remain less than 30% the co-seismic offset measured from the daily solution.

Details on the GPS processing and determination of co-seismic displacements are given in chapter 3.7. The data can be visualized and downloaded from the Caltech Tectonics Observatory web site (http://www.tectonics.caltech.edu/sumatra/data).

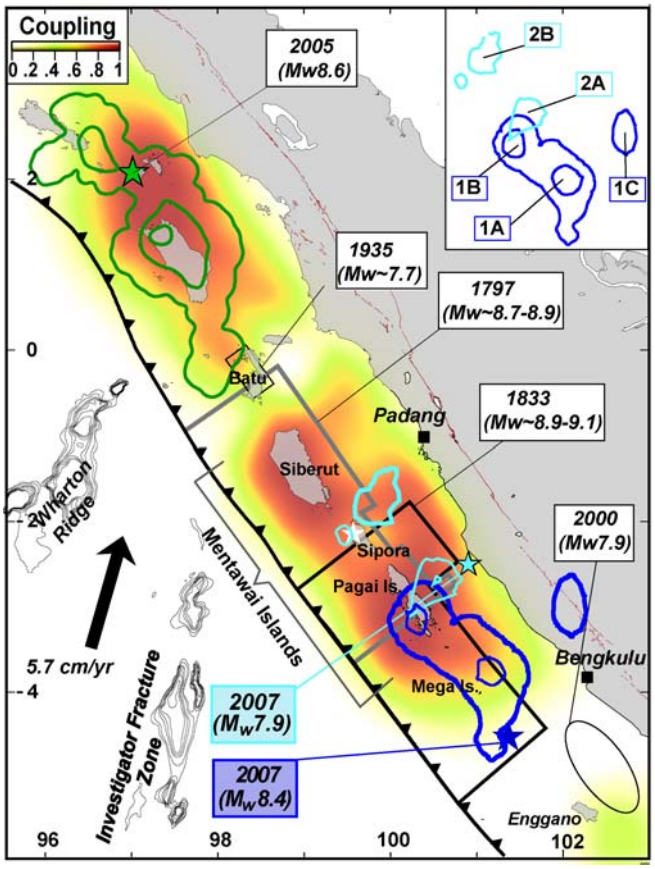

Figure 3.1 Interseismic coupling and rupture areas of large interplate earthquakes on the Sunda megathrust offshore Sumatra. The oblique convergence rate of 5.7mm/yr across the Sunda trench Offshore Sumatra is partitioned between 43 mm/yr of thrust motion on the megathrust and 23mm/yr of strike-slip faulting mainly accommodated by the Great Sumatra Fault. Dip-slip motion on the megathrust results from seismic and aseismic slip. The pattern of coupling, defined as the ratio of interseismic slip rate to plate convergence rate, was derived from the modeling of geodetic and paleogeodetic measurement of interseismic strain (Chlieh et al., in press). The area north of 2°N has no data so the coupling coefficient at this region reflects the lack of resolution. The slip distributions of M_w8.6 Nias-Simeulue earthquake (Briggs et al., 2006; Konca et al., 2007) is shown with 5 meter contour lines. Slip distributions of 2008, M_w 8.4 and Mw 7.9 earthquakes are shown with 1 meter contour lines. The rupture areas of the M_w~8.7, 1797 and M_w~9 1833 were derived from the modeling of a sparse dataset of paleogeodetic measurements of co-seismic uplift (Natawidjaja et al., 2006). The location of the 2000 earthquake, which is mostly an intraslab rupture (Abercrombie, Antolik and Ekstrom 2003), is also shown for indication. The labels of various asperities are displayed in the inset.

3.3.2 Field Measurements of Uplift

The Mentawai Islands area is rich in *Porites* coral heads which can be used for measuring emergence or submergence relative to a tidal datum (Briggs et al., 2006; Scoffin and McLean 1978; Taylor et al., 1987; Zachariasen et al., 2000). The highest level of survival (HLS) of *Porites* corals off the west coast of Sumatra typically lie ~4 cm above annual low tide (Briggs et al., 2006). Because it is unclear how quickly after an uplift event the coral dies down to its new HLS, we chose to compare the pre-earthquake HLS to post-earthquake annual lowest tide (ALT) to determine uplift and subsidence. The field survey took place form September 30 to October 10. We surveyed the water level at each site and used a tidal model (Agnew 1997) to estimate the ALT at each survey site relative to the water level at the time of measurement. The uplift or subsidence at the site is the difference between the pre-earthquake HLS and the computed elevation of post-earthquake ALT, corrected by 4 cm to account for the difference between HLS and ALT (Briggs et al., 2006). Significant uplift was measured at Mega islands, South and North Pagai Islands and at the southern tip of Sipora Island. The maximum uplift, 1.5m, was measured at Mega about 70 km northwest of the epicenter. The uplift decreases from 1 meter under South Pagai to 10 cm under North Pagai Island. The uplift at the southern tip of Sipora Island is on the order of 30 cm (inset in Figure 3.2a).

3.3.3 InSAR data

Four independent L-band interferograms were processed from ALOS PALSAR images (http://www.palsar.ersdac.or.jp/e/index.shtml) using ROI_PAC(Rosen et al., 2004). Coherence is generally good and deformation is well resolved, highlighting the main advantage of L-band over C-band in areas where the vegetation is dense (see chapter 3.7 for more information about the data and processing). The images were unwrapped yielding a measure of the Line Of Sight (LOS) displacement field, i.e., along the vector pointing toward the satellite. This LOS vector points about 38° from vertical toward an azimuth of about N78°E. The unwrapped interferograms were resampled with variable grid size using a resolution-based algorithm (Lohman and Simons 2005) and are shown in Figure 3.2b. The post-earthquake images were acquired between 4 days and 43 days after the day of the earthquake. The pre-earthquake images were acquired in the month before, except for track 445 which was acquired 8 months before the earthquake sequence (Table 3.1). In view of the GPS time series,

the preseismic signal in these data can be neglected. The postseismic signal could represent as much as 30% of the signal measured on Siberut (track 450) and is probably a much smaller fraction of the signal measured from the other tracks which were all acquired less than 20 days after the mainshock.

3.3.4 Seismological data

We selected teleseismic waveforms from the IRIS network to assure a good azimuthal coverage. The broadband seismograms were bandpass filtered from 1.5 s (P waves) and 3 s (SH waves) to 200 s. We have used 16 P and 19 SH waveforms for the M_w 8.4 earthquake, and 19 P and 17 SH waveforms for the M_w 7.9 earthquake. The duration of the waveforms used for modeling the earthquake was 120 seconds for both the M_w 8.4 and M_w 7.9 earthquakes. See chapter 3.7 for more details.

3.4 Finite source models

3.4.1 Method

An optimization based on simulated annealing algorithm was used to obtain the best-fitting models by searching bounded parameter spaces of slip amplitude, rake angle and the rupture velocity using both teleseismic and geodetic data (Ji, Wald and Helmberger 2002a). The best fitting model is determined from the minimization of a goodness-of-fit criterion that quantifies the fit to the seismological and to the various geodetic datasets accounting for the data uncertainties. Because the formal uncertainties assigned to the various datasets are not easily comparable and might ignore some sources of uncertainties, we have renormalized the uncertainties. The normalized uncertainties assigned to any type of data were computed from the standard deviation of the misfits between the considered subset of data and the predictions of the best-fitting model derived from the joint inversion. This is achieved through a few iterations since the uncertainties enter the goodness-of-fit criterion. The megathrust is assumed to be planar and with a constant dip angle of 15° approximately equal to the dip angle determined from the CMT. The fault plane is subdivided into 16km by 16km elementary subfaults (12km by 10km in the case of the M_w 7.9 event). The rupture velocity is allowed to vary between 2.1 km/s and 2.8km/s and the rake angle is allowed to vary between 80° and

130°. Details of the inversion procedure and normalization of uncertainties are given in Chapter 3.7.

3.4.2 Cumulative slip model

We have first determined models representing the cumulative effects of the seismic sequence derived from the modeling of the geodetic data: i.e. the cumulative GPS displacements, coral uplifts and InSAR range changes. These data are measurements of displacements over different periods of time and therefore include a variable amount postseismic deformation. Most data were acquired less than a month after the mainshock. In view of the GPS times series we estimate that over that period the cumulative geodetic moment must have accumulated by 20%. The model obtained from only the cumulative cGPS displacements (measured from the offset of the time series including the M_w 8.4 and M_w 7.9 event) is the least contaminated by postseismic relaxation (Figure 3.6). It suggests a relatively patchy slip distribution with a released geodetic moment of 7.3 $\times 10^{21}$N.m. When the GPS data are combined with the InSAR and the field data, the spatial resolution is improved but some contamination by postseismic deformation is introduced. The resulting model (Figure 3.2) has a total moment of 7.5 $\times 10^{21}$N.m which is only marginally different from the one derived from the GPS measurements only. So the source model derived from the combination of all the geodetic data is probably a better constrained representation of the co-seismic slip distribution than that derived from the GPS data only, although they do not differ much. This source model is also very similar to the cumulative model obtained by adding the M_w 8.4, M_w 7.9 and M_w 7 co-seismic source models described below (Figure 3.6b). This shows that the effect of the post-seismic data is not prevailing in our models which include field and InSAR measurements and that the patchiness of the slip distribution is most likely real.

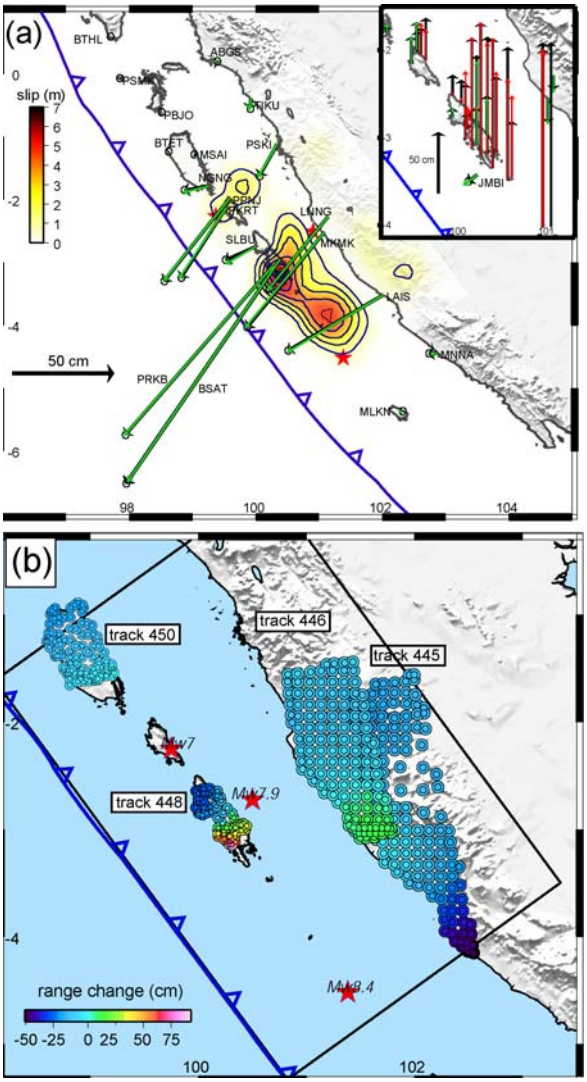

Figure 3.2 Geodetic deformation and cumulative slip distribution due to the M_w 8.4 and 7.9 earthquakes of September, 12, 2007. (a) Cumulative-slip model derived from the inversion of the geodetic and inSAR data. Observed (black) and modeled (green) horizontal displacement vectors at the SuGAR GPS stations are shown with normalized error ellipses. Inset shows the vertical GPS displacements and field measurements of coral uplift (black) and the fits from the model (green for GPS, red for black). (b) Fits to the InSAR data. Each data point is represented by a color-coded circle, where the outer circle is data and inner circle is the synthetic.

The obtained source model (Figure 3.2) shows a rupture area that extends continuously from the epicentral area, offshore Bengkulu, to South Pagai continuously, and a disconnected slip patch below Sipora Island. Another, though less prominent, slip patch is found north Bengkulu. This is a robust feature of the model and it is evident from both track445 and track446 of InSAR data (Figure 3.2b) and horizontal to vertical ratio of LAIS station (Figure 3.2a). We have tested that any smoother slip distribution would yield a significantly worse fit to the data. On the contrary, the goodness-of-fit criterion does not improve significantly if the weighting of the smoothness of the slip distribution is decreased. In this model the slip peaks to a maximum of 8 meters under South Pagai Island (Figure 3.2) and to local maxima of 6 m between the epicenter and Mega Island. The maximum slip beneath Sipora Island is 2.5 m. The total moment is 7.5 10^{21} N.m, equivalent to an M_w 8.5 earthquake. The normalized uncertainties are estimated to be about 1cm for the GPS measurements, 11cm for the field measurements and 1.5cm for the inSAR measurements. The misfits to the geodetic data are shown in Figure 3.12. This shows that the geodetic data can be reasonably well fit from a model that assumes that all the deformation resulted from slip on the megathrust.

3.4.3 Source models of the M_w 8.4 and M_w 7.9 earthquakes

We derived a source model of the M_w 8.4 and M_w 7.9 earthquakes based on the modeling of the teleseismic waveforms, GPS measurements, and a selection of field data and InSAR data. To select the field data relevant to the modeling of each event we first carried on an inversion of only the teleseismic and GPS data and used these preliminary models to determine the zone of influence of each of these events. Cleary the ruptures area of these two events abut each other beneath the Pagai Islands. Therefore, the uplift measurements from the Pagai Islands (field measurements and PALSAR track 448) and from the Sumatra mainland coastal area (PALSAR track 446) reflect the cumulative effect of the two events. The displacements measured within PALSAR track 445 and vertical displacement measurements at Mega Island from uplifted coral heads (Figure 3.2) are clearly attributable to the M_w 8.4 shock. Also track 445 includes only 4 days of post-seismic slip; therefore, we chose to incorporate it in the mainshock model. These data were therefore inverted jointly with the GPS measurements and the teleseismic records of that earthquake.

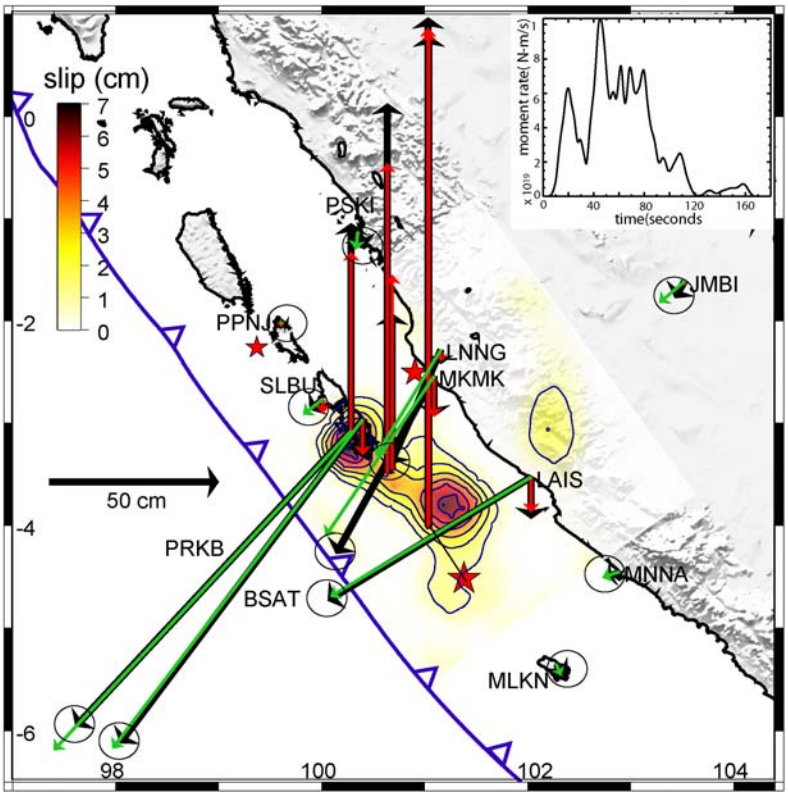

Figure 3.3 Source model of the M_w8.4 earthquake. Map view of slip distribution obtained from the joint inversion of the teleseismic waveforms, GPS, field measurements of uplift and InSAR data. Observed (black) and predicted (green for horizontal, red for vertical) displacements with error ellipses are shown at the GPS stations and at a selection of sites where uplift measured in the field is unambiguously attributed to the M_w 8.4 earthquake. Red star is the location of epicenter. Moment rate function is shown in the inset.

The source model of the M_w 8.4 earthquake shows unilateral northward rupture which initiated about 70km south of Mega Island (Figure 3.3). The slip distribution shows three main asperities, defined here loosely as patches with large co-seismic slip although the original definition was more specific (Lay, Kanamori and Ruff 1982). One is located east of Mega Island with a peak slip of 6 meters (1A in Figure 3.1), one beneath South Pagai Island, with a peak slip of 7 meters (1B in Figure 3.1), and a deeper one beneath Bengkulu coastal area with a 2 meter peak slip (1C in Figure 3.1). The total moment corresponding to this model (~5. 10^{21} N.m) is consistent with the CMT moment magnitude. The rupture is not very impulsive with rise times of the order of 5-10 seconds (chapter 3.7, Figure 3.9). The source-time function

(inset in Figure 3.3) indicates that the initiation is not very impulsive: the moment rate increases smoothly over the first 8 s. The source-time function also exhibits a total duration of about 100 s with the first asperity rupturing between 20 s and 40 s and the second asperity releasing the largest proportion of the total released moment between 50 s and 80 s. The seismic signature of the deep slip patch (1C) is less clear. If this patch is removed, the fit to the seismic waveforms and the source-time function are only marginally modified (chapter 3.7, Figure 3.10). However, this deep slip patch is required to fit the co-seismic uplift at the cGPS station LAIS (Figure 3), as well as the track 445 InSAR data which was acquired only 4 days after the M_w 8.4 shock. The LAIS station on the Bengkulu coast recorded only 10 cm subsidence while it moved 70 cm towards the trench. The only plausible way to explain this horizontal and vertical displacement is to invoke some slip on megathrust on the down-dip side of this station (chapter 3.7, Figure 3.11). The InSAR data help constrain the shape and location of this slip patch (track 445 and 446 of Figure 3.2b). Assuming a low dip angle of only 15 degrees, this slip patch would lie at a depth of about 90 km. More realistic megathrust geometry would place it at a more plausible depth of about 120 km. Since the sampling at LAIS station is 120 s, slip on this asperity most probably occurred during the seismic phase. However, when we remove this deep patch from our model and recalculate the moment rate (chapter 3.7, Figure 3.10), we notice that this deep patch does not contribute much to the details of the moment-rate function. We conclude that this slip-patch is real and ruptured during the 8.4 earthquake, although it did not contribute much to the seismic radiation (it cannot be a rough, high-speed rupture).

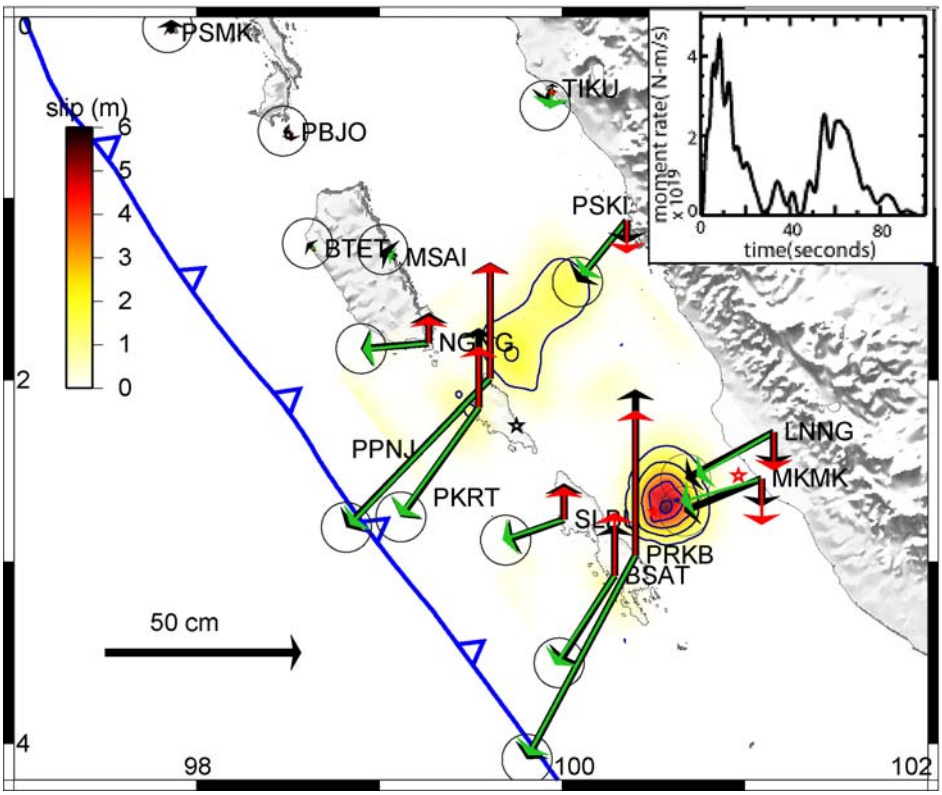

Figure 3.4 Source model of the M_w 7.9 earthquake. Map view of slip distribution obtained from the joint inversion of the teleseismic waveforms, GPS, field measurements of uplift and InSAR data. Observed (black) and predicted (green for horizontal, red for vertical) displacements are also shown at the GPS stations. Red star is location of epicenter. Moment release rate function is shown in inset. Geodetic data are listed in chapter 3.7 and Figure 3.8 shows observed and predicted teleseismic waveforms.

The M_w 7.9 event also ruptured unilaterally to the north, releasing a total moment of 1.1 $\times 10^{21}$ N.m in about 80 seconds. The earthquake initiated at the down-dip zone of the northern end of the M_w 8.4 event that had ruptured 12 hours earlier. Two distinct asperities that are 130 km apart can clearly be distinguished (Figure 3.4). The seismic waveforms require the first subevent, located along the eastern coast of South Pagai Island, to be extremely impulsive, with a short rise time of a few seconds at most, and a highly peaked slip distribution close to the epicenter (Figure 3.4, Figure 3.8). The second subevent is located 130 km to the northwest, off the north-eastern coast of Sipora Island. There is no evidence for significant slip in between these two asperities.

3.5 Discussion

3.5.1 Interseismic Strain can Reveal Permanent Barriers

The September 2007 sequence ruptured a number of distinct asperities on the megathrust which fall approximately within a patch that had remained strongly locked in the interseismic period (Figure 3.1). This observation suggests that the extent of megathrust rupture might be bounded by creeping areas which would act as permanent barriers to rupture propagation. One interpretation is that the portions of the megathrust that creep in the interseismic period would be obeying a rate-strengthening friction law preventing earthquake nucleation and inhibiting seismic rupture propagation (Scholz 1990). This might be the controlling factor of the down-dip extent of megathrust seismic rupture, but it may also influence the along-strike extent of large megathrust ruptures as well. The creeping portion of the megathrust at the southern end of the 2007 rupture in the Enggano area is possibly such a permanent barrier, similar to the one near the Batu Islands (Figure 3.1). In any case, the pattern of interseismic strain can help evaluate the maximum possible extent of large megathrust ruptures.

3.5.2 Similar rupture areas but different asperities in 1833 and 2007

The asperities ruptured by these earthquakes also fall approximately within the rupture area of 1833 earthquake (Figure 3.1). This gives a unique opportunity to find out how similar the corresponding co-seismic slip distributions are and whether they reflect ruptures of the same set or of a subset of permanent asperities.

The comparison of coral uplifts from the 1833 event shows that the patterns and amounts of slip in 1833 and 2007 ought to be significantly different. Co-seismic uplifts in 1833 range between 1 and 2.5m from S. Pagai Island to Sipora Island (Natawidjaja et al., 2006). These are much larger than those observed in 2007 at close-by locations, and suggest much larger co-seismic slip, even if some significant amount of postseismic slip could be included in the paleogeodetic estimates. This is consistent with the cumulative geodetic moment released by the earthquakes sequence in 2007, 7.5 10^{21} N.m, representing only a fraction of the 10-55 10^{21} N.m moment assigned to 1833 event (Chlieh et al., in press) (Figure 3.5). The coast of North Pagai Island was significantly uplifted 2.5m in 1797 earthquake, and 0.8m in 1833, suggesting that significant uplift occurred beneath this island in both 1797 and 1883 earthquakes

(Natawidjaja et al., 2006). This area is clearly a low-slip patch in 2007, as indicated by the modest horizontal and vertical displacements recorded at SLBU (22cm and 7cm, respectively). It acted more like a barrier (Aki 1984) in 2007. Thus, we infer that the pattern of asperities is not the same from one event to the other, although they rupture approximately the same portion of the megathrust.

3.5.3 Dynamic or static triggering, seismic or aseismic slip?

Both the 8.4 and 7.9 earthquakes consist of sub-events which ruptured quite distant asperities that show up in the source-time functions and slip-distributions. For the M_w 7.9 earthquake, the two asperities are separated by 100 km spatially and 40 seconds in time. Considering the low slip in the area in between these asperities, it is probable that, in both cases, the second asperity was triggered by the S waves generated by the first asperity, although standard subshear rupture propagation cannot be ruled out. On the contrary, the 12 hour delay between the 7.9 and the 8.4 is more consistent with triggering by static stress change.

There is also clear indication that M_w 8.4 rupture induced some slip in the deep zone that was mostly creeping in the interseismic period (asperity 1C in Figure 3.1). Because this slip patch is quite isolated, we exclude that it would be due to the propagation of the rupture in the rate-strengthening zones as is observed in numerical simulations (Lapusta and Rice 2003; Tse and Rice 1986). It could either reflect seismic rupture of a rate-weakening portion of the megathrust embedded in a dominantly creeping zone, or be an example of triggered aseismic transient. Deep aseismic transients on megathtust have been observed elsewhere (Pritchard and Simons 2006) and near-seismic rupture velocity were found to be possible within the rate-and-state friction theory of fault behavior (Liu and Rice 2005; Perfettini and Ampuero 2008) . This example is the first obvious observation of such deep slip patch being triggered during an earthquake.

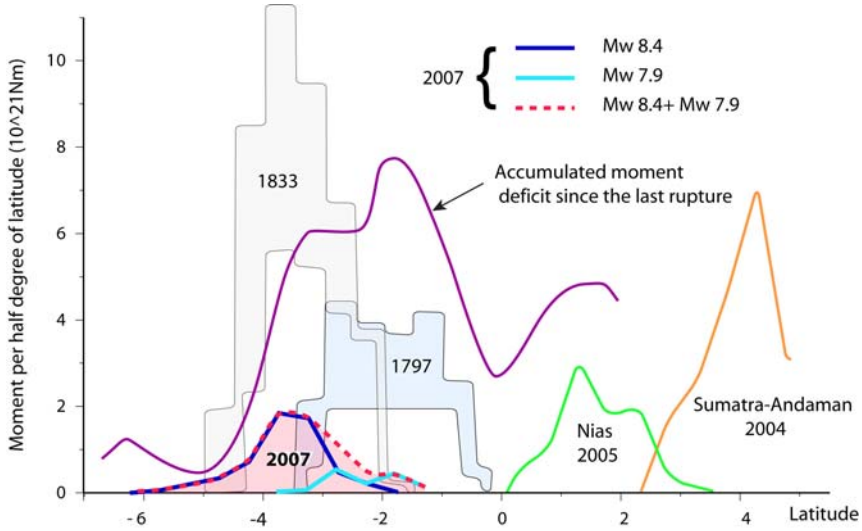

Figure 3.5 Latitudinal distribution of moment released due the large earthquakes on the Sunda megathrust from 1797 to end of 2007 and accumulated deficit of moment along the Sunda megathrust offshore Sumatra. For the 1833 and 1797 earthquakes, the curves show upper and lower bounds on the moment release as estimated from paleogeodetic measurements. Given the limited temporal resolution of the paleogeodetic data, it is not possible to estimate accurately the amount of postseismic slip eventually included in that estimate. It could probably be as much as 25%. For comparison, after slip in the few years following the following the 2004 and 2005 earthquakes released up to 25% of the co-seismic moment. The purple curve shows the accumulated moment deficit since the last rupture derived from the modeling of interseismic strain accumulation (Figure 1, model F-f of Chlieh et al., in press). The values were obtained by summation within 0.5°-wide bins and therefore represent integrals over half a degree of latitude.

3.5.4 Testing the time-predictable and the slip-predictable model

It is possible to estimate the deficit of moment that has accumulated since the last historical ruptures of the Sunda megathrust (namely the 1797, 1833 and 1861 earthquakes) assuming that the pattern of interseismic locking of the plate interface has remained constant over the whole interseismic period (Figure 3.5). It turns out that the 2007 sequence released only a fraction of the moment deficit that had accumulated since the 1833 earthquake. Moreover, even larger deficit moment that has accumulated north of the Pagai Islands, remains virtually untapped by the 2007 sequence, although the accumulated interseismic moment exceeds the moment released in 1797 earthquake.

The 2007 sequence re-ruptured the 1833 rupture area, despite the fact that interseismic strain had not yet recovered the amount of strain released in the previous event. But the recent sequence did not extend much into the 1797 rupture area where the interseismic strain has recovered more than the amount of strain released in 1797. These observations show that the amount of moment released in the 2007 sequence does not relate simply to the deficit of moment accumulated since the previous rupture. It also shows that the the interseismic period separating the 1833 and 2007 sequence was somewhat too short (by 0 to 150yr) than the time needed for the recovery of the strain released by the previous rupture. In other words, neither the time-predictable model nor the slip-predictable model (Shimazaki and Nakata 1980) seem to apply well in the case of the 2007 Sumatra earthquakes.

3.5.5 Why did not the 2007 earthquakes grow bigger?

A striking feature of the 2007 earthquake sequence is that it ruptured an area comparable to the rupture area of the 1833, M_w ~9 .0 event, but did not release as large a moment as that previous event and only a fraction of the deficit of moment that had accumulated since. The spatiotemporal complexity of the rupture might explain why the 2007 earthquake did not grow bigger. Indeed, it seems that the sequence ruptured a set of distinct asperities that did not cooperate well. If two neighboring asperities on the same fault plane rupture jointly they are expected to cooperate to each release more moment than if they had ruptured independently(Rundle and Kanamori 1987). This is because the static stress change induced by one asperity increases the Coulomb stress on the other, hence the elastic stress to be released during the rupture, provided that the friction drops to the same dynamic value during the seismic rupture. If we look at the spatiotemporal evolution of the rupture, it is clear that this kind of cooperation did not operate well during the 2007 sequence. For example, slip on the second asperities (2B in Figure 3.1) started only once slip on the first asperity (2A) asperity was over. So the reloading of asperity 2A due to rupture of asperity 1B did not contribute to any additional seismic slip. This might be because the intervening area between the 2 asperities did not produce much slip and acted as a barrier to the rupture propagation. The portion of the megathrust beneath N. Pagai Island experienced little co-seismic slip, as evident for the small displacement at SLBU but is probably not a permanent barrier since very significant slip occurred there during both the 1833 and 1797 earthquakes. Actually the N. Pagai area is above

the portion that experienced the largest cumulative slip, estimated to be 17 m (Natawidjaja et al., 2006), if the slip from 1797 and 1833 earthquakes are summed together. This area may therefore have acted as a barrier in 2007 because of a locally lower stress level before the earthquake left over from previous earthquakes. Another possibility would be that this area would be a permanently creeping area which would have produced large amount of afterslip following the 1797 and 1833 events. Although the interseismic coupling pattern suggests a locally lower degree of locking in this area (Figure 3.1) the hypothesis of a nonpermanent barrier seems more likely to us.

Little coupling between the rupture of asperities 1B and 2A is also evident from the 12 hour time lag between their ruptures. In that case, the cause of the lack of cooperation between these two asperities is more enigmatic, given that they lie so close. One may speculate that a narrow zone with low pre-stress due to the slip distribution related to the 1833 and 1797 events may have acted as a barrier there, or that there would be a creeping zone too narrow to show up in the pattern of interseismic strain. In any case it seems that the static Coulomb stress increase on asperity 2A due to the M_w 8.4 earthquake, was enough to trigger a delayed rupture of this asperity, a feature predicted by the earthquake nucleation models based on rate-and-state friction laws (Dieterich 1996). It is interesting to note that, on the contrary, the dynamic stresses induced by the M_w 8.4 earthquake failed in triggering rupture of asperity 2A.

3.6 Conclusions

By analyzing jointly geodetic and seismological data we have been able to describe the details of the earthquake sequence that ruptured the Sumatra megathrust in the Mentawai Islands area in 2007. Overall, the rupture area was confined to an area bounded by permanent barriers related to creeping portions of the megathrust (Chlieh et al., 2007; Cross and Freymueller 2007; Freymueller and Beavan 1999; Pritchard and Simons 2006; Suwa et al., 2006). Such barriers, which are found to influence the down-dip as well as the lateral extent of megathrust ruptures can be imaged from the modeling of interseismic strain, except possibly those lying in stress shadows along the up-dip portion of the plate interface (Burgmann et al., 2005). The complex spatiotemporal pattern of the 2007 rupture is probably key factor for the much smaller slip compared to previous historical earthquakes in the area. 2007 ruptures did not release much of the deficit of moment that had accumulated since the last rupture. The

sequence essentially ruptured a set of asperities, which triggered each other through static and dynamic interactions, but did not cooperate well because of intervening barriers. Some of these barriers are most probably not permanent and are related to the distribution of slip due to past earthquakes. This adds to the view that seismic asperities are probably not permanent features (Park and Mori 2007) but rather move around from one rupture to the other so that within the area that are locked in the interseismic period, co-seismic slip adds to the equal long term slip rate. Such a pattern emerges also in dynamic fault models (Ben-Zion and Rice 1993; Cochard and Madariaga 1996), although it seems that, in reality, permanent barriers produce a seismicity pattern less irregular than the one observed in these experiments. An interesting aspect of the 2007 sequence is also that it seems to have induced some very early aseismic slip at depths deeper than the locked fault zone, possibly triggered by the dynamic or static stress increase. This could reflect a patch with rate-weakening friction embedded in a zone dominated by rate-strengthening friction, or be a case of rapid aseismic transient.

3.7 Supplementary Information

3.7.1 GPS data and processing

The data processing was carried out using GAMIT/GLOBK version 10.31. Total of 9 days of observations were used covering from September 8 to Sept 16, 2007. The data are processed in daily sessions if no quake took place and subdaily sessions if quake events took place. For each session, a regional network is formed consisting of the regional sites and selected nearby global sites. The global sites are: COCO, DGAR, GUAM, IISC NTUS PERT and TIDB. The data sampling is 120 sec. IGS final orbits and IERS final earth orientation parameters were used with tight constraints. Standard corrections were applied including solid earth tide, polar tide, and ocean tides. Tropospheric delay parameters were estimated at one hour interval. After completing individual daily/subdaily sessions using GAMIT, the loosely constrained solutions were grouped into 4: one before the 1st quake, one after the 1st quake and before the 2nd, one after the 2nd and before the 3rd, and one after the 3rd. They were then fed into GLOBK combined with SOPAC final global solutions in order to tie the solutions to the ITRF2005 global reference frame.

3.7.2 Measurements of uplift from emerged coral heads

Coral microatolls of the genus *Porites* are sensitive natural recorders of lowest tide levels (Briggs et al., 2006; Scoffin and McLean 1978; Taylor et al., 1987; Zachariasen et al., 2000), they are ideal natural instruments for measuring emergence or submergence relative to a tidal datum. Massive *Porites* coral heads grow radially upward and outward until they reach an elevation that exposes their highest corallites to the atmosphere during lowest tides. This subaerial exposure kills the uppermost corallites in the colony, thus restricting future upward growth. The highest level to which a coral can grow is termed the highest level of survival (HLS). If a coral microatoll is then uplifted or subsides, its morphology preserves information about relative water level prior to the land level change (Briggs et al., 2006; Taylor et al., 1987).

When coseismic uplift occurs, those portions of the microatoll colony raised above lowest tides die, but if lower parts of the coral head are still below lowest tides, its uppermost living tissues demarcate a new, post-earthquake HLS (Taylor et al., 1987). Although the HLS of *Porites* corals off the west coast of Sumatra has been shown to typically lie ~4 cm above annual low tide (ALT, the lowest low tide of any given year) (Briggs et al., 2006), it is unclear how quickly after an uplift event the coral dies down to its new HLS. Consequently, we elect to compare the pre-earthquake HLS to post-earthquake ALT to determine uplift and subsidence.

To determine the post-earthquake ALT, we surveyed the water level at each site during our visit. We then used a computational tidal model to estimate how much lower ALT should be at each survey site relative to the water level at the time of measurement. The uplift or subsidence at the site is the difference between the pre-earthquake HLS and the computed elevation of post-earthquake ALT, corrected by 4 cm to account for the difference between HLS and ALT (Briggs et al., 2006). Our tidal calculations are based on harmonic tidal constituents extracted from a regional satellite-based model for Indonesia (Egbert and Erofeeva 2002), using the software package NLOADF (Agnew 1997; Meltzner et al., 2006).

The coral data shows that the maximum uplift from the sequence is under Mega Island with about 1.5 meters of uplift. The uplift decreases from 1 meter under South Pagai to 10 cm under North Pagai Island. The uplift on the Sipora Island is on the order of 30 cm (Figure 3.1b).

3.7.3 InSAR: data and processing

We use level 1.0 PALSAR images from the ALOS satellite (L-band, 23.6cm) which is operated by the Japanese Space Agency (JAXA). Four independent L-band interferograms (Table 3.1) were processed using the JPL/Caltech software ROI_PAC (version 3.0) (Rosen et al., 2004). The topographic phase contribution was removed using a 3 arc.sec (~90 m) digital elevation model from the Shuttle Radar Topography Mission (SRTM) (Farr et al., 2007). The interferograms were next unwrapped to get Line Of Sight (LOS) displacements, i.e. along a direction that is pointing approximately N78°E with an incidence angle of 38° from vertical. Typical PALSAR raw data in the Fine Beam Single (FBS) polarization mode has a row width of ~20000 pixels, exactly twice that of Fine Beam Double (FBD) images (Shimada et al., 2007a). In order to make a mixed-mode interferogram (FBS2FBD) for track 445, the FBD was up-sampled by FFT (Sandwell et al., 2007). Even in heavily vegetated areas, coherence is generally good and deformation is well resolved, highlighting the main advantage of L-band over C-band: i.e. less temporal decorrelation due to its capability to penetrate more deeply in vegetation. The track 448 pair, in which coherence degrades rapidly in areas of rugged terrain in the south part of South Pagai Island, is explained by the large perpendicular baseline (506 m, Table 3.1). Because most interferograms do not extend far enough from the area with significant ground displacements, possible orbital errors were not corrected for a priori. Instead, we allow for a ramp correction (1s order polynomial) in the LOS displacement field that is solved for during the joint inversion.

The intereferograms were unwrapped using the SNAPHU algorithm (Chen and Zebker 2002). The unwrapped interferograms were resampled with variable grid size using a resolution-based algorithm (Lohman and Simons 2005) and are shown in Figure 3.2b.

Table 3.1. Information about the interferograms computed from ALOS PALSAR images from ascending tracks

Region	Track	Frame numbers	Acquisition date 1	Acquisition date 2	Mode [1]	$B_{\perp}$(m) [2]
Bengkulu	445	7	29-Jan-07	16-Sep-07	FBS2FBD	141
	446	2	18-Aug-07	03-Oct-07	FBD2FBD	268
Pagai	448	1	06-Aug-07	21-Sep-07	FBD2FBD	506
Siberut	450	1	09-Sep-07	25-Oct-07	FBD2FBD	58

[1] FBS: Fine Beam Single Polarization (HH, 28 MHz bandwidth); FBD: Fine Beam Dual polarization (HH and HV, 14 MHz) (Shimada et al., 2007b).

[2] $B_{\perp}$ is the perpendicular baseline, that is, the component of the orbital separation perpendicular to the line of sight.

Table 3.2. Misfits and normalized uncertainties for the models of events and datasets

Model	Moment (N.m)	Misfit	GPS (cm)			Coral	InSAR
			σ_e	σ_n	σ_z		
Cumulative (GPS only)	7.3×10^{21}	-	0.9	1.	0.9	-	-
Cumulative (all data)	7.5×10^{21}	-	0.9	1.1	1.0	11.15	1.48
M_w 8.4	5.15×10^{21}	0.14	2.4	2.2	4.1	7.4	3.6
M_w 7.9	1.13×10^{21}	0.25	2.6	2.6	2.3	-	-
M_w 7	4.7×10^{19}	-	1.7	2.2	1.5	-	-

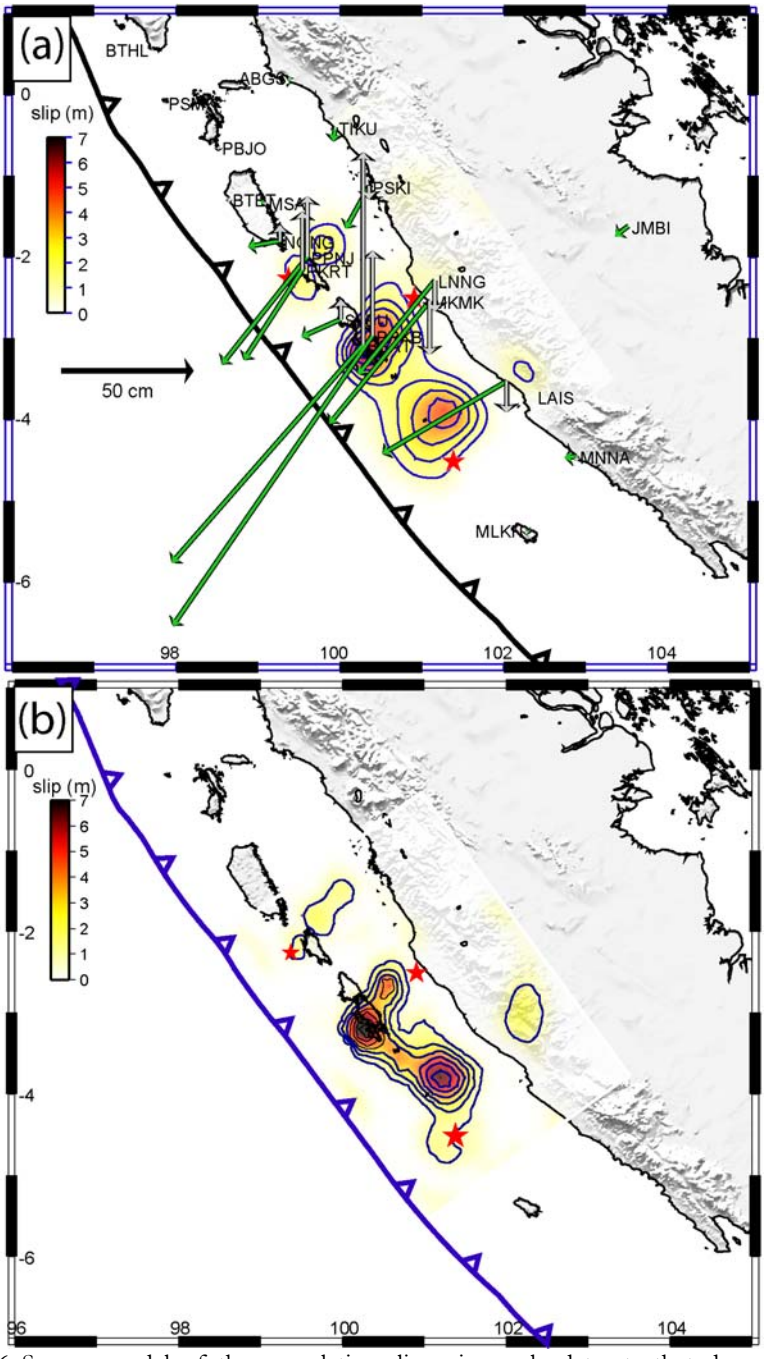

Figure 3.6 Source model of the cumulative slip using only datasets that do not include significant post-seismic deformation. (a) Cumulative-slip model derived from the inversion of the cGPS data only. Observed (black) and modeled (green for horizontal and gray for vertical) displacement vectors at the SUGAR GPS stations. (b) Cumulative slip from addition of coseismic models of M_w 8.4 and M_w 7.9 earthquakes.

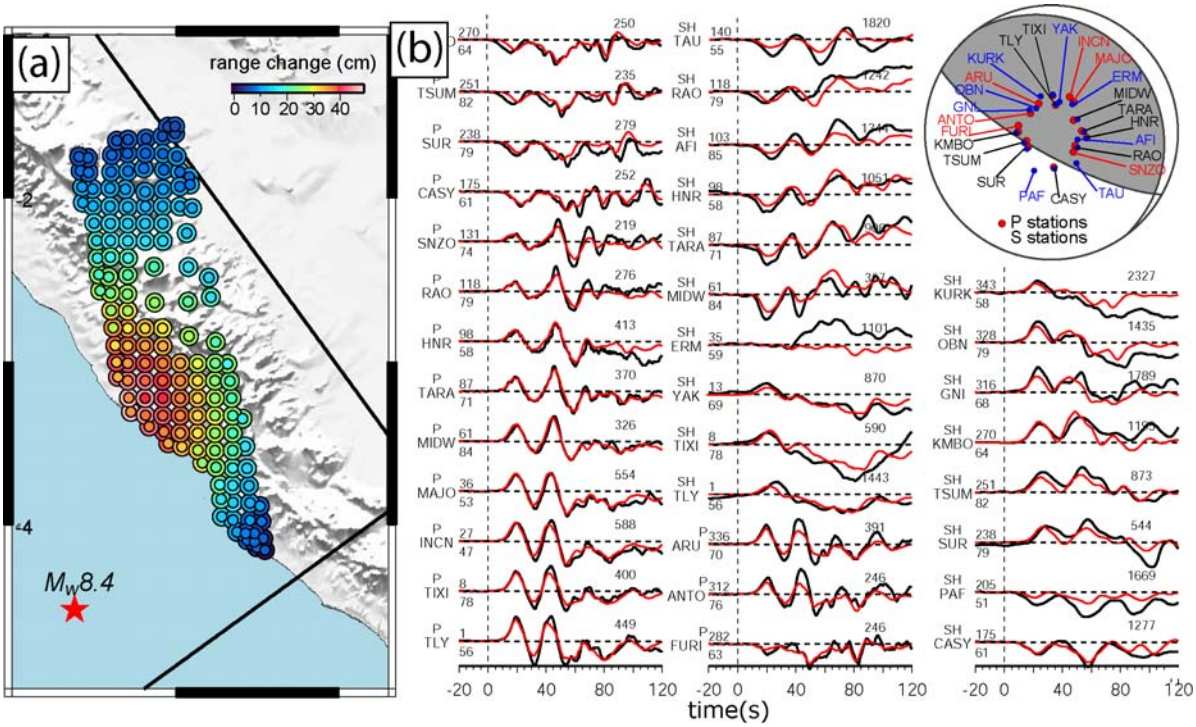

Figure 3.7 Fits to the data from modeling of the M_w 8.4 earthquake. (a) Observed and modeled LOS displacements to the Insar data. Only the southernmost track (ref), where the effect of the 7.9 earthquake can be assumed negligible was used to constrain this event. (b) Observed (black) and synthetic (red) teleseismic *P* and *SH* waveforms. Station name, azimuth, and distance are indicated on the left of each trace. The maximum displacement is shown at the top right of each trace in microns.

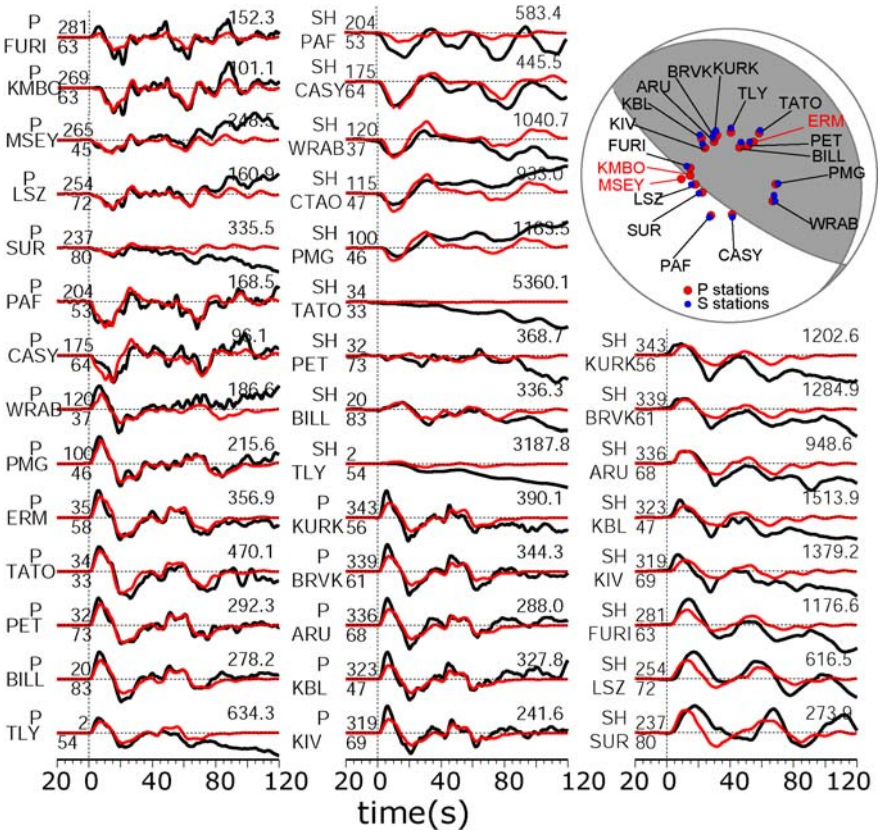

Figure 3.8 Source model of the M_w 7.9 earthquake. Observed (black) and synthetic (red) teleseismic *P* and *SH* waveforms. Station name, azimuth, and distance are indicated on the left of each trace. The maximum displacement is shown at the top right of each trace in microns.

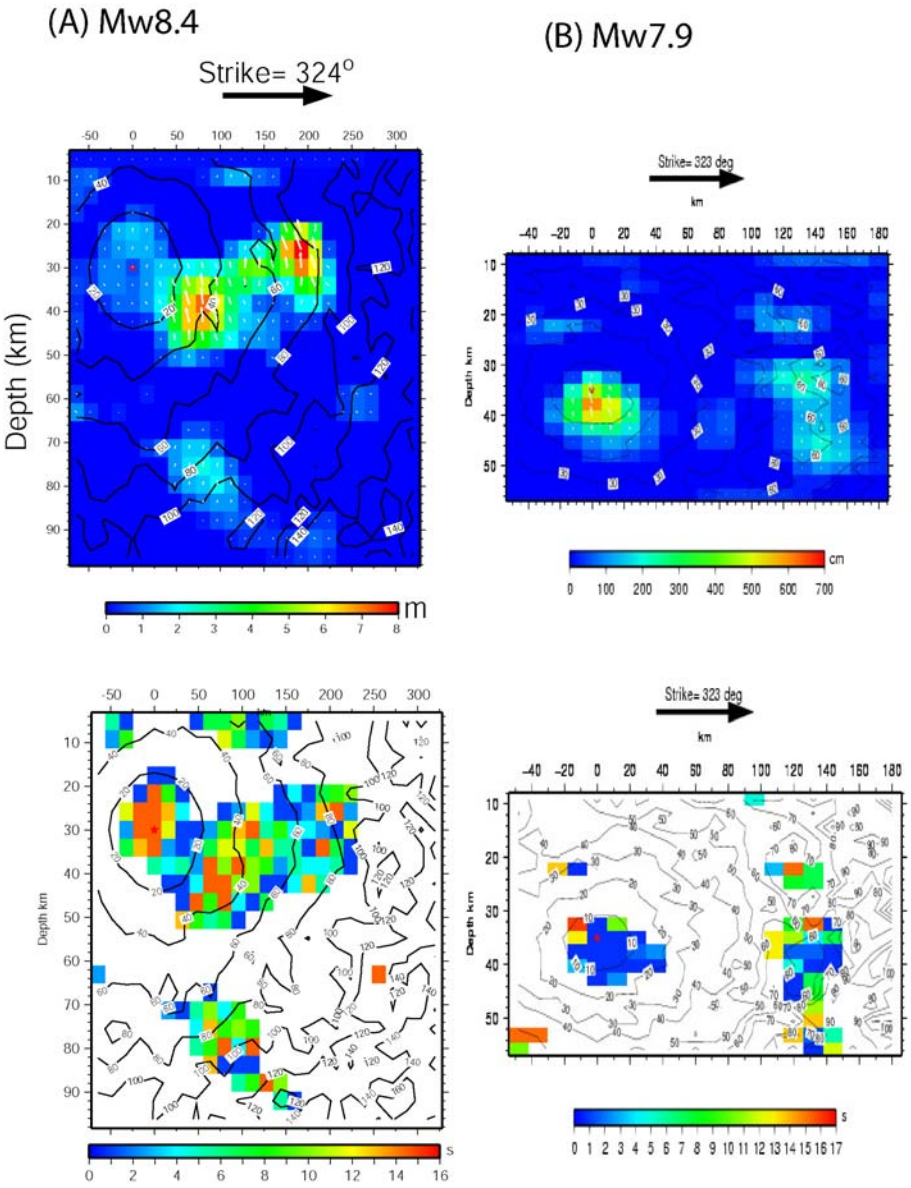

Figure 3.9 Rise time vs. slip for 8.4 and 7.9 earthquakes are shown.

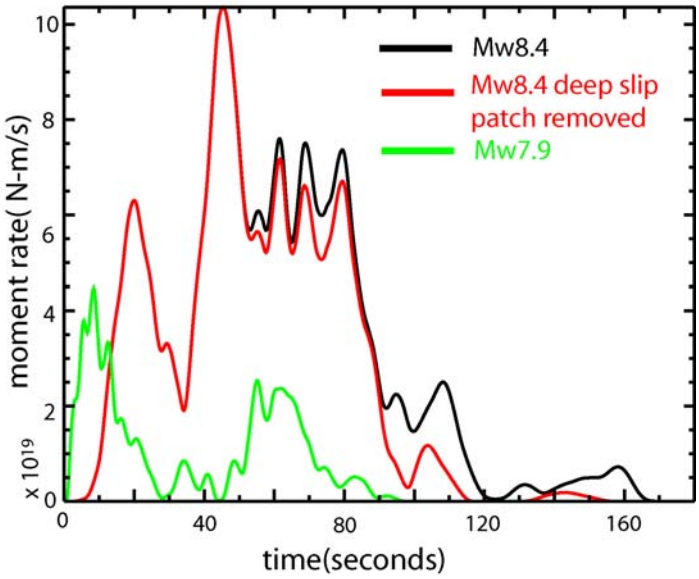

Figure 3.10 Moment rate for the M_w 8.4 and M_w 7.9 events. The (red) shows the M_w8.4 earthquake where the portions deeper than 65 km are removed.

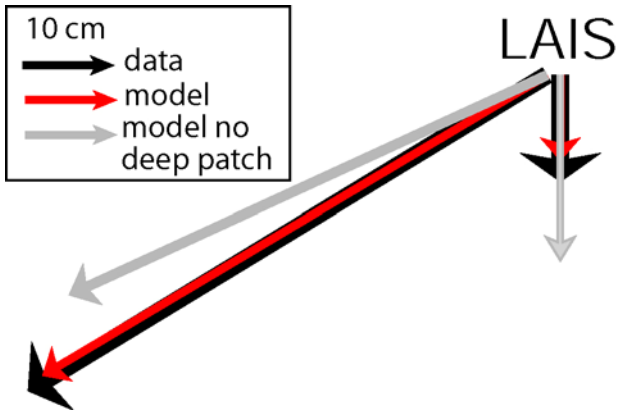

Figure 3.11 Fits to the LAIS station with and without the deep patch. "Model no deep patch" is the model where the all the slip deeper than 60 km was removed, leaving only slip to the southwest (trenchward side) of the station. Without any down-dip slip, fitting the horizontals with the right amplitude and angle requires the vertical subsidence to be much larger than what the data shows.

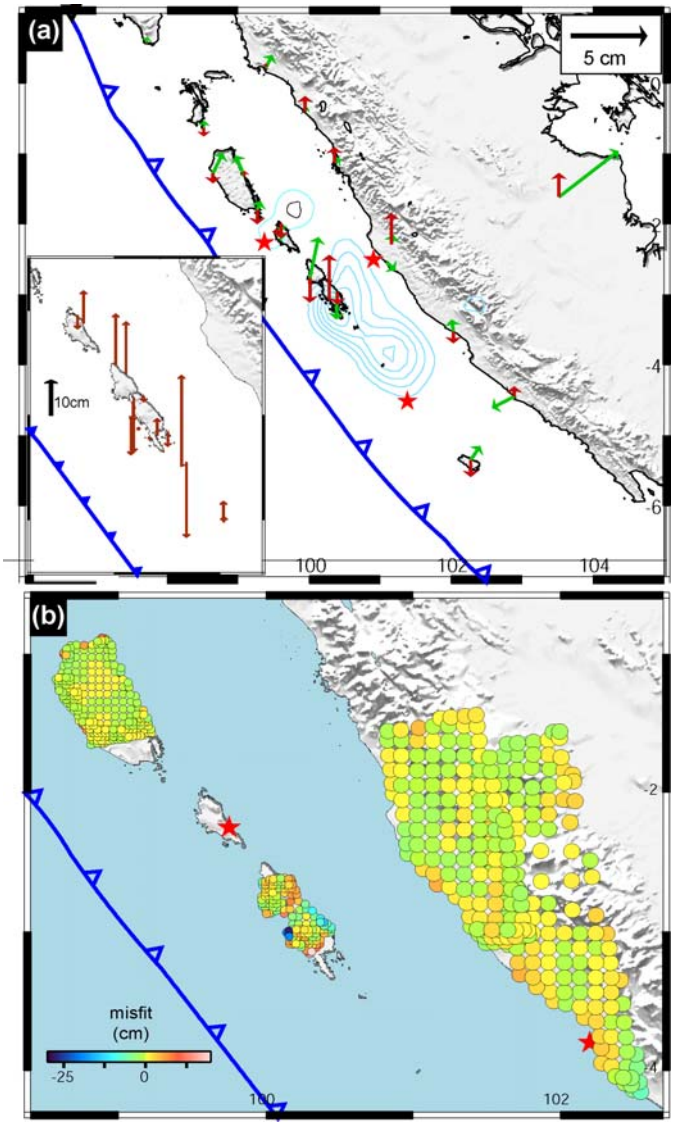

Figure 3.12 Geodetic data residuals (data – synthetic) from the cumulative model shown in Figure 3.2. (a) GPS and coral misfits. Horizontal GPS misfits are shown in green and verticals in red. The inset shows the misfit to the coral data. (b) Misfits to the InSAR data.

3.8 Acknowledgement

My collaborators in this study were Jean-Philippe Avouac, Anthony Sladen, Aron Meltzner, Kerry Sieh, Peng Fang, Zenghong Li, John Galetzka, Jeff Genrich, Mohamed Chlieh, Yehuda Bock, Eric Fielding, Chen Ji, Don V. Helmberger

Chapter 4: Rupture Process of 1999. M_w 7.1 Duzce Earthquake from Joint analysis of SPOT, GPS, InSAR, Strong-Motion and Teleseismic data

4.1 Abstract

We analyzed the rupture process of 1999 M_w 7.1 Duzce earthquake using geodetic and seismic data. Applying sub-pixel cross-correlation of SPOT images acquired before and after the event, we mapped a continuous fault trace over 55 km; 15 km longer than the field reports. We investigated the spatiotemporal evolution of the earthquake using improved fault geometry with constraints on surface offsets based on satellite imagery, incorporated GPS and InSAR data and four strong-motion stations in the vicinity of the rupture. Our joint modeling shows a very stable slip distribution that does not depend on rupture velocity constraints. We show that no constant rupture velocity can explain the strong-motion data. Due to constraints from fault geometry and geodetic data, the rupture velocity has to vary rapidly. The rupture starts slow, accelerates to supershear speeds toward east and subsequently slows down. Supershear rupture is local and only toward the east of the hypocenter. Teleseismic data is consistent with the joint near-field model when 2 s time shift is applied to their hand-picked arrivals. This implies that the weak beginning of the earthquake is not observable at teleseismic distances. This appears to be a common problem with teleseismic modeling and leads to more compact models with major slip around the hypocenter than the actual phenomenon. We performed teleseismic inversion models comparing four-segment fault geometry based on satellite imagery to one-segment geometry based on CMT solution. The four-segment model gives better predictions of near-field ground motions.

4.2 Introduction

Resolving the rupture process of earthquakes is fundamental to understanding the earthquake physics. Near-field seismograms have been extensively used when available since the Imperial Valley earthquake and provided crucial information about the rupture process of earthquakes (Hartzell and Helmberger 1982b; Hartzell and Heaton 1983; Olson and Apsel

1982). Developments in geodesy improved the resolution on fault geometry and provided abundant static data and subsequently led to improvement in understanding the rupture details. Using multiple plane fault geometries, near-field and far-field seismograms and available near-field geodetic data, many features of earthquakes and near-field motions have been studied (Delouis et al., 2002; Hernandez, Cotton and Campillo 1999; Ji, Helmberger and Wald 2003; Ji et al., 2004).

The 12 November 1999 M_w 7.1 Duzce Earthquake occurred three months after the 17 August 1999 M_w 7.4 Izmit earthquake and ruptured the Duzce segment of the North Anatolian Fault Zone (NAFZ). The M_w 7.4 Izmit and the M_w 7.1 Duzce earthquakes are the most recent of the western migrating right-lateral earthquakes along NAFZ in the 20^{th} century (Barka 1996; Pondard et al., 2007). The field studies suggested a 40 km rupture extending east from the re-ruptured eastern end of the M_w 7.4 Izmit Earthquake (Akyuz 2002; Pucci et al., 2006; Pucci et al., 2007) (Figure 4.1a). Burgmann et al., (2002) studied the GPS and InSAR data and came up with a 49 km fault dipping 50^o-60^o to the north. A particularly interesting aspect of the Duzce earthquake was the proposed supershear rupture speeds suggested from S-P differential time (Bouchon et al., 2001) and strong-motion waveform modeling (Bouin et al., 2004).

Compact source area, existence of near-field recordings and geodetic data, field studies of the fault map and offsets, as well as available SPOT images that are utilized in this study make Duzce earthquake an ideal case for using multiple datasets to study faulting and various tradeoffs of earthquake kinematics.

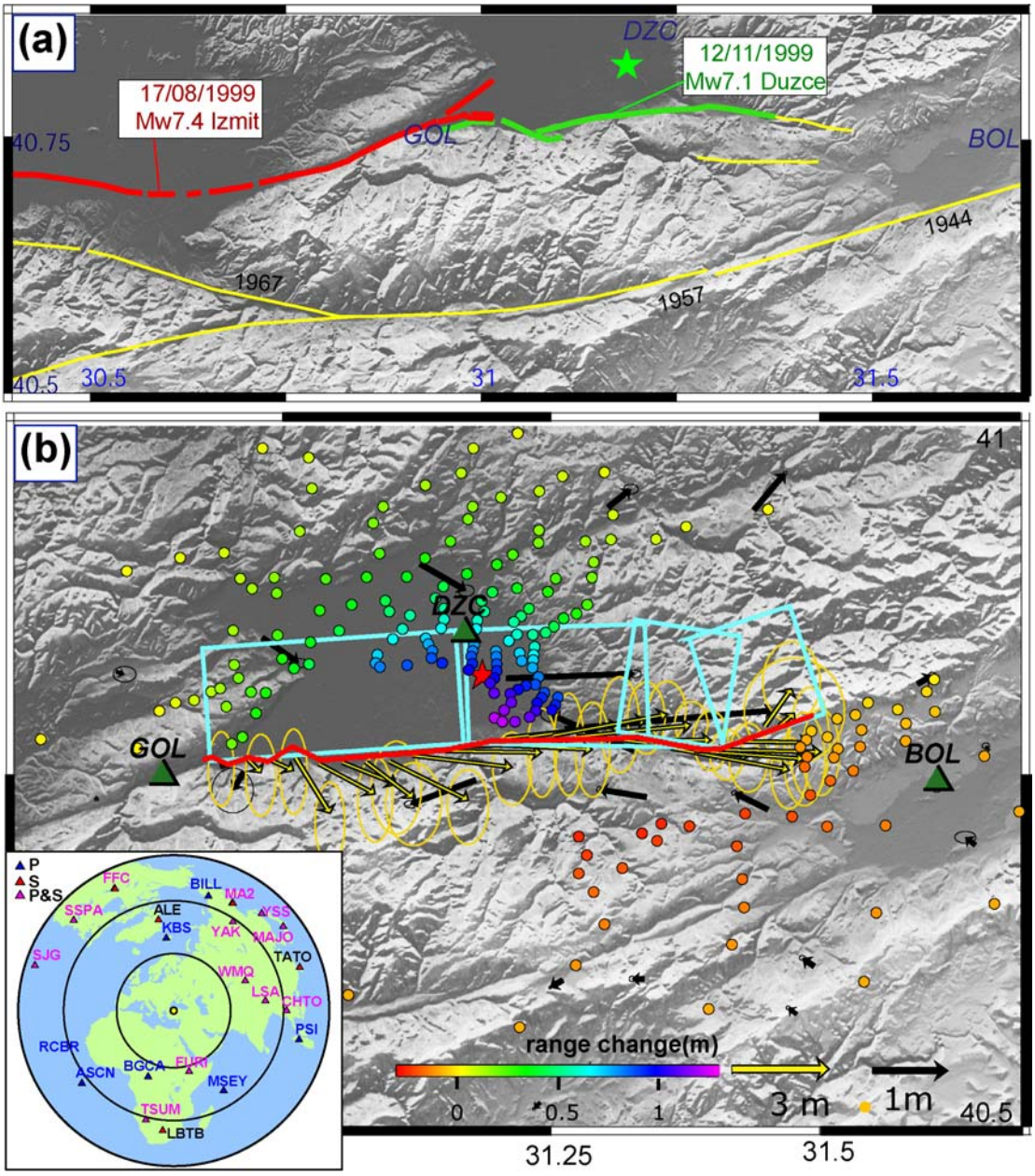

Figure 4.1 (a) Map of the study area. The map of eastern end of M_w 7.4 Izmit earthquake and M_w 7.1 Duzce earthquake are displayed. The southern (Mudurnu) strand of NAF is also shown with the event dates from the 20th century earthquakes. (b) The map of the Duzce earthquake region and datasets used in this study. The surface offset obtained from SPOT image cross-correlation is shown in red and the offset vectors are shown in yellow along with error estimates. The edges of the four-segment fault geometry created based on SPOT imagery are displayed in cyan. GPS displacements are shown with black arrows. Each resampled InSAR data point is marked as a circle color coded according to the range change

value. The three near-field stations are represented with green triangles. The inset shows the locations of the teleseismic stations used in this study.

There is no study considering the geometrical complexities of faulting and surface offsets as well as utilizing all available geodetic data and modeling near field strong-motion data. When only seismic data are used, the slip locations, amplitudes and rise times can trade off with rupture velocity (Konca et al., 2007). Moreover, the slip models obtained from strong-motion data should be consistent with surface exposure of the fault, as well as the static displacement data.

By combining all the available data, and in addition using optical imagery to confine fault geometry and surface offsets, we address the following remarkable questions. How does the fault trace and surface offsets from satellite imagery compare to the field measured values? By building more accurate fault geometry, can we obtain better fits to the geodetic data? Using an accurate fault geometry and rupture length, and constraining surface offsets and slip using geodetic data, can we assess more about the nature of the rupture velocity using strong-motion data? Can we clarify the existence and extent of proposed supershear rupture velocity toward east? Is the near-field model of the earthquake consistent with teleseismic data? Can we predict near-field motions using teleseismic data? Do the constraints from optical imagery on fault geometry and surface offset lead to better prediction of strong-motion predictions and damage assessments?

Initially, we focus on obtaining an accurate fault rupture map with surface offsets using SPOT imagery and compare our satellite obtained fault map with the field studies. Next, using the fault geometry built based on satellite imagery, and utilizing new and existing geodetic data along with the strong-motion data, we will study the rupture process of the Duzce earthquake. We also show predictions of teleseismic data from the modeling of all the near-field data. Finally, we examine whether accurate fault geometry obtained from satellite imagery can help us estimate strong-motions better, to test the satellite image cross-correlation as a future real-time application.

4.3 Fault Trace and Offsets: Sub-Pixel Cross-Correlation of Satellite Images

Sub-pixel cross-correlation of optical images before and after the earthquakes has been shown to be a particularly useful way to obtain fault trace and surface offsets leading to improvement in constructing fault geometries of large crustal earthquakes (Avouac et al., 2006; Michel and Avouac 2002). Because of abundant field observations (Pucci et al., 2007) and available SPOT images before and after the event, the M_w 7.1 Duzce earthquake proves to be a very good example where SPOT images can be used to refine fault rupture and be compared to the field offset measurements.

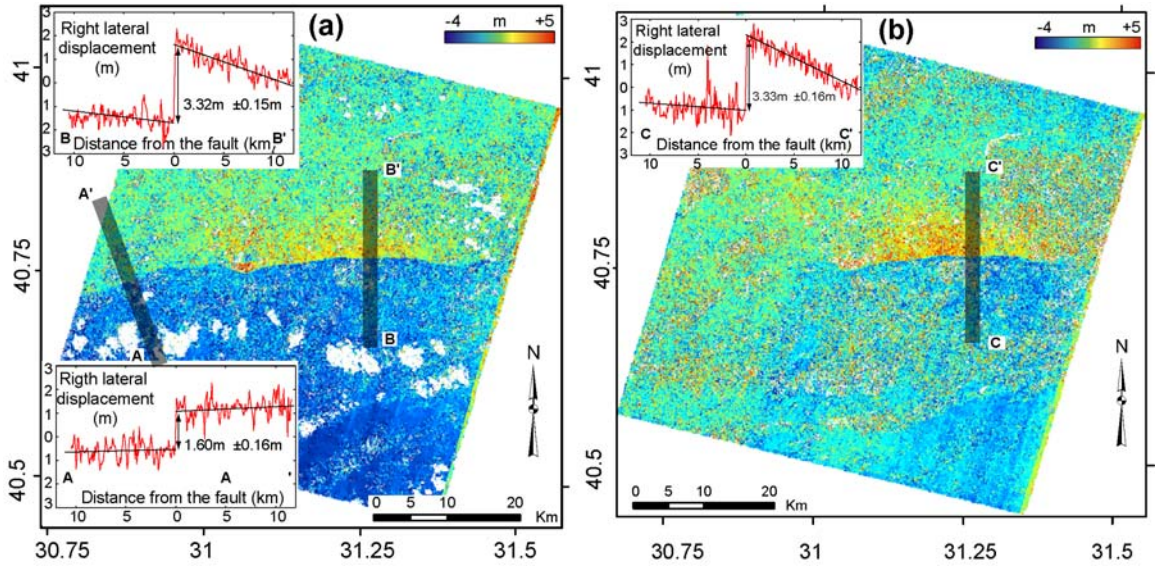

Figure 4.2 The cross-correlated SPOT images. (a) Cross-correlation of SPOT images from June 6, 1999, and July 12, 2000, covering the co-seismic motions of both M_w 7.4 Izmit and M_w 7.1 Duzce earthquakes. (b) Cross correlation of SPOT images from October 10th 1999, and July 12th 2000, covering only the Duzce earthquake. Three profiles of right lateral displacement are also shown. B-B' and C-C' are the profiles through same geographical location.

In this study, three SPOT images are used to study the Duzce earthquake. The first image was acquired 2 months before the Izmit earthquake, the second image was acquired 47 days after Izmit earthquake and 40 days before Duzce earthquake, and the last image was obtained 9 months after the Duzce earthquake (Table 4.1). These three images are resampled and orthorectified using DEM from SRTM 3 arcsec (90 meters) (Leprince et al., 2007). Then the

images before and after the earthquake were cross-correlated. The correlation analysis was done with 32x32 pixels windows size. Steps of 8 pixels between adjacent correlations yielded offset maps sampled at every 80 m.

The cross-correlation results of images 1 (before both events) and 3 (after both events) and images 2 (between two events) and 3 are shown in Figure 4.2a and Figure 4.2b, respectively. The cross-correlation of image 1 and 3 clearly shows the Duzce offset as well as the eastern end of the Izmit offset (Figure 4.1a, Figure 4. 2a) while the 2 and 3 cross-correlation shows the Duzce rupture only (Figure 4. 2b). The profiles taken at the center of Duzce rupture from both images (B-B' in Figure 4. 2a and C-C' in Figure 4.2b) show clear right-lateral offset that agree within couple of centimeters (Figure 4.2, inset) demonstrating the accuracy of this method in obtaining the map of the fault zone and fault offset.

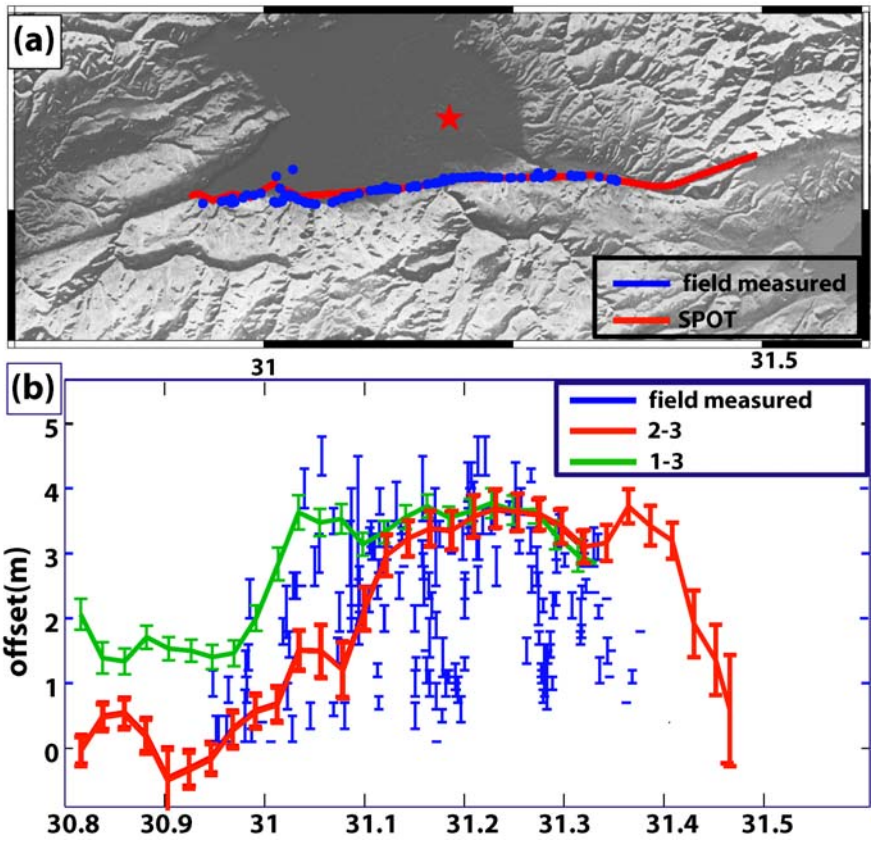

Figure 4.3(a) Comparison of surface fault rupture trace, blue dots are from field measurements of Pucci et al., 2007, red trace is from SPOT image cross-correlation (b) Comparison of right lateral offsets obtained by field studies (blue) and SPOT cross-correlation method (red and green). Red and green curves show the offset calculated from the cross-correlation of the image pairs 2-3 (spanning the time of Duzce earthquake only) and 1-3 (including both Izmit and Duzce earthquake ruptures), respectively.

Table 4.1 | Information about the SPOT images used in this study

Image number	Image date	Satellite-Resol.	Incidence
1	21-06-1999	SPOT 1 - 10m	+11 degrees
2	03-10-1999	SPOT 1 - 10m	+10.4 degrees
3	12-07-2000	SPOT 1 - 10m	+10.4 degrees

Table 4.2 | Geometry, dimensions and locations of the fault model

Segment	Strike	Dip	Depth Extent (km)	West End	East End
1	266	65	19	30.93°-40.76°	31.17°-40.77°
2	268	65	19	31.17°-40.77°	31.34°-40.78°
3	279	65	19	31.31°-40.78°	31.41°-40.77°
4	252	65	19	31.41°-40.77°	31.50°-40.79°

Table 4.3 | Velocity Model used for teleseismic and geodetic data

Top Depth (km)	Vp (km/s)	Vs (km/s)	Density (kg/m3)	Qp	Qs
0	4.69	2.71	2.43	200	100
1	4.78	2.76	2.45	200	100
2	4.94	2.85	2.49	400	200
3	5.15	2.97	2.53	400	200
4	5.38	3.11	2.58	500	250
5	5.64	3.25	2.63	500	250
7	5.87	3.39	2.67	600	300
9	6.06	3.50	2.72	600	300
11	6.17	3.56	2.75	800	400
13	6.23	3.60	2.77	800	400
15	6.25	3.61	2.78	800	400
20	6.33	3.65	2.80	800	400
25	6.55	3.78	2.86	800	400
30	6.86	3.96	2.94	1000	500
35	7.20	4.15	3.04	1000	500
38	8.05	4.39	3.30	1000	500

Table 4.4 | The list of strong-motion, GPS and InSAR models that have various rupture velocities (V_R), and the associated errors

Model name	V_R toward east of hypocenter	V_R toward west of hypocenter	Waveform Error	χ_r^2 (GPS)	χ_r^2 (InSAR)
V_R2	2 km/s	2 km/s	0.263	1.77	0.3
V_R3	3 km/s	3 km/s	0.261	1.70	0.27
V_R4	4 km/s	4 km/s	0.261	1.69	0.27
V_R5	5 km/s	5 km/s	0.262	1.89	0.30
V_R2.5-4	2.5-4 km/s	2.5-4 km/s	0.206	1.78	0.27
V_REf_Ws	2.5-4km/s	2.5-3 km/s	0.208	1.70	0.23

The field studies that mapped the fault trace and measured offset using fences, creeks, channels and walls (Pucci et al., 2006; Pucci et al., 2007) enable us to compare the fault trace and ground displacement that are obtained from SPOT images. This comparison shows that the fault map obtained from satellite imagery agrees very well with the field measured fault map (Figure 4.3a). Moreover, the SPOT images show 15 km longer rupture to the east, with a change of strike toward north-east. This strand could have been hard to see in the field due to rough topography.

The prior models of the strong-motion data based on a single plane and shorter fault had problems with abrupt end to the slip to the east, and a possibility of an additional eastern rupture segment was suggested (Bouin et al., 2004). Burgmann et al., (2002) also argued that rupture might be extending further east than the field studies suggested based on the GPS and InSAR data, but the location, extent and strike of this additional rupture was not determined. This study sheds light on to the eastern termination of the rupture which proves to be crucial in studying the rupture process.

The comparison of SPOT offsets with field measured offsets is shown in Figure 4.3b. This comparison demonstrates that along the center of the fault, where maximum offset was observed, the field and SPOT values are consistent. The SPOT offsets are enveloping the field measurements smoothly, while field measurements are rapidly varying spatially. The main reason for the high variability of slip in field measurements can be due to shallow distributed shear which can vary along the fault and lead to underestimation of field measurements made based on discontinuities (Haeussler et al., 2004; McGill and Rubin 1999; Simons, Fialko and Rivera 2002). On the other hand, the SPOT measurements can provide results that are smoother than the actual displacements due to the finite pixel size (90m) and cross-correlation method.

At the eastern end, the SPOT offsets decrease further to the east, presenting a longer rupture as mentioned before. At the western end, the SPOT measured offsets from the cross correlation of images 2 and 3 (including only Duzce earthquake) seem to be less than the field offsets. This could be due to overestimation in the field observations caused by addition of co-seismic and post-seismic slip of Izmit earthquake to the coseismic Duzce rupture. This

argument is supported by the fact that the cross-correlation of image pairs 1 and 3 (including both earthquake times) seem to agree very well with the field observations (Figure 4.3b).

We built a four-segment fault model obtained based on the SPOT surface faulting map (Figure 4.1b, Table 4.2). Burgmann et al., (2002) studied the dip of the Duzce fault using GPS and InSAR data. This study shows that the dip angle is in the range of 50°-65° with 54° as the best fit value. In this study, we define the fault plane by requiring that the fault has to meet the surface expression at the right place and has to pass through the hypocenter, which is well defined thanks to the dense local short period network (Aktar et al., 2000). This technique gives a dip angle of 65°, which is in the range of possible dips and is appropriate for explaining all the available data.

4.4 Datasets

4.4.1 Geodetic data

We have utilized former geodetic and seismic studies of the Duzce earthquake. In particular, 50 3-component survey-type GPS stations were used (Figure 4.1b). The InSAR data was obtained from ERS satellite images collected at 14 September 1999 and 22 November 1999 and resampled to 234 points (Figure 4.1b). The InSAR data is primarily sensitive to east-west displacement, which makes it very appropriate for the study of the primarily right-lateral east-west trending Duzce rupture. These geodetic datasets are previously described in detail Burgmann et al., (2002) and Ayhan, Burgmann and McClusky (2001).

We built the four-segment fault model based on the SPOT obtained fault map. We also constrained the slip on the shallowest sub-faults close to the surface using the offsets obtained from SPOT images (Figure 4.1b).

4.4.2 Seismic data

Three strong-motion stations close to the fault as well as one station 65 km to the west of the rupture were used (Figure 4.1b, Figure 4.11a). Three of these stations belonged to General Directorate of Disaster Affairs and 1 was installed by a French-Turkish team. This data was integrated once to obtain velocity and band-passed from 1 second to 50 seconds. This dataset is explained in detail by Bouin et al., (2004). Teleseismic data was selected from IRIS network. We have used 19 *P* and 15 *SH* waveforms based on their simplicity and azimuthal distribution

(Figure 4.1b, inset). The broadband seismograms were band-pass filtered from periods of 1 second to 50 seconds.

4.5 Inversion method

We employed a simulated annealing algorithm to fit the wavelet transform of the seismograms and reduced chi-square to the geodetic data to model the data from the Duzce earthquake (Ji, Wald and Helmberger 2002a). The Green's functions for geodetic and teleseismic data were calculated using the elastic layer in Table 4.3 from (Sekiguchi and Iwata 2002) that was modified from (Mindavelli and Mitchell 1989). For the strong-motion data, we used different 1-D velocity structures for each station based on Bouin et al., (2004) since stations are in different geological settings.

We used 4 km by 3 km sub-faults along strike and dip, respectively. Dip is set to be 65^{o} and range of rake angle is between 160^{o} and 220^{o}. The rupture velocity was allowed to vary, and will be discussed in detail later.

4.6 Joint models of Strong-Motion, GPS and InSAR data with Surface Offset Constraints

4.6.1 Slip Models

We have performed inversions using all the available near field data. We have tested models with various fixed and varying rupture velocity constraints (see Table 4.4 for a list of the models). Figure 4.4a shows the resulting slip models with constant rupture velocities listed in Table 4.4. The slip pattern we have obtained is similar to those by Bouchon et al., (2001) and Bouin et al., (2004). However, since we use a four-segment fault model with extended rupture to the east, there are differences. Most of the slip is to the east of hypocenter. The western portion of the slip seems to be very shallow, and does not extend to depths of more than 5 km.

It is important to note that there is hardly any variation in slip models when different rupture velocity constraints are used (Figure 4.4a). This is a clear indication that the existence of abundant geodetic data as well the constraints on the shallow slip from SPOT images stabilizes the obtained slip model. The only variation that is still observable is the changes in

associated rise times (the time it takes for slip to occur at a point on the fault) when rupture velocity is changed (Figure 4.4b).

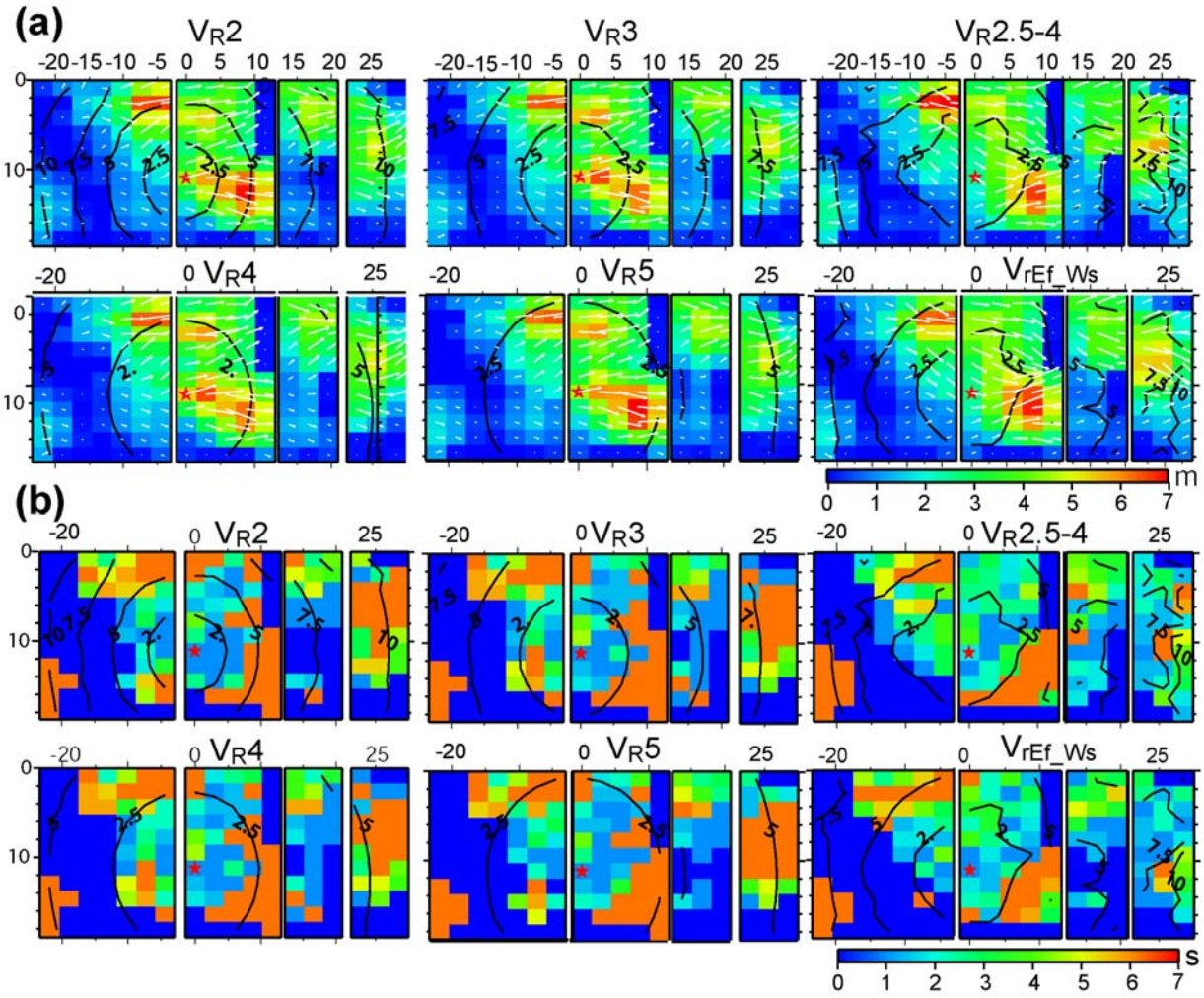

Figure 4.4 (a) Slip and (b) rise time distributions on the fault for inversion assuming various rupture velocity constraints. Rise times are shown for the sub-faults that slip more then 0.5 meters, since the ones that slip less can not be constrained reliably. The rupture front contours are drawn for every 2.5 seconds. V_rEf_Ws is the model where rupture velocity is 2.5-3km/s to the west and 2.5-4km/s to the east.

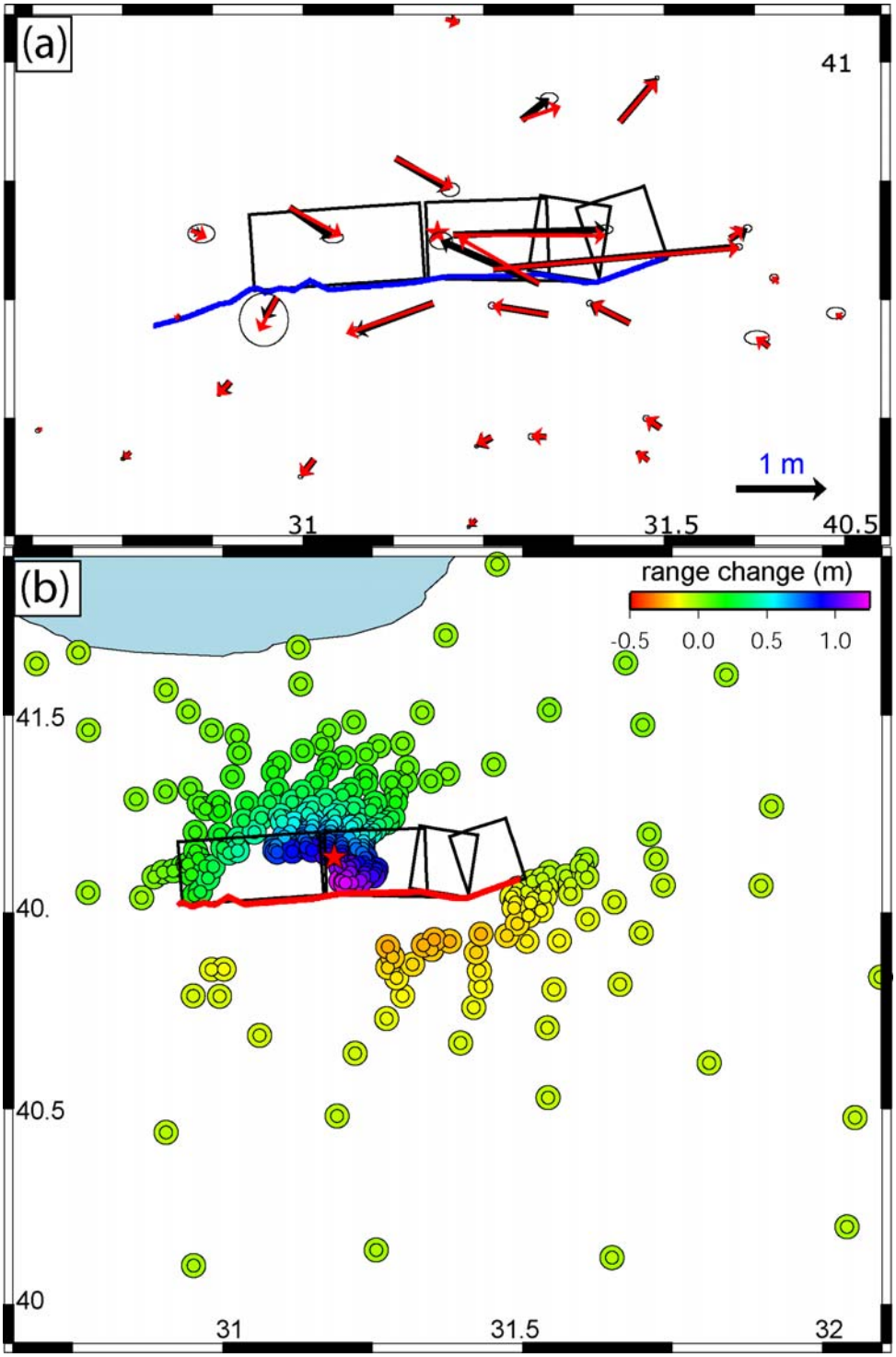

Figure 4.5 Fits to the (a) GPS data where the black arrows are the data and red arrows are synthetics (b) InSAR data. Each data point is represented by a color coded circle, where the outer larger circle give the value for data and inner circle is the model prediction. The fits are

from the model V_REf_Ws tabulated in Table 4.4. Other models have almost identical fits to the static data.

Since the slip models are very similar, their misfits to the geodetic data are also comparable. Overall the reduced χ^2 of both InSAR and GPS datasets are close to 1 (Table 4.4), *i.e.* the fits to these datasets are good (Figure 4.5). The Weighted Residual Sum of Squares (WRSS) defined as $(\boldsymbol{d}_{obs} - \boldsymbol{d}_{mod})^T \boldsymbol{cov}^{-1} (\boldsymbol{d}_{obs} - \boldsymbol{d}_{mod})$ is 255 for GPS and 55 for InSAR data. These WRSS values are significantly lower than previous geodetic study (321 for GPS and 224 for InSAR data) by Burgman et al., (2002). This demonstrates that our four-segment geometry is appropriate to explain both the geodetic and seismic data, and details of the fault geometry improve the fits to the geodetic data.

4.6.2 Rupture Kinematics: Supershear or Not?

Supershear rupture speeds have been proposed for crustal strike-slip faults since the recordings of strong-motion instruments starting with 1979 Imperial Valley Earthquake (Archuleta 1984) where seismic records were explained by local supershear rupture speed. Strong-motion records of the M_w 7.4 Izmit earthquake were also studied and supershear rupture velocities toward the east of the hypocenter were suggested from waveform modeling (Bouchon et al., 2000; Sekiguchi and Iwata 2002) and S-P differential arrival time (Bouchon et al., 2001). Bouchon and Vallee (2003) studied regional surface waves of 2001 Kunlun Earthquake and came up with supershear rupture speed. (Dunham and Archuleta 2004) have shown that a dynamical model with supershear rupture speed could explain a near-field record with two separate pulses from 2002 Denali earthquake. The lab studies of cracks and sliding experiments have also demonstrated experimental verification of sub-Rayleigh to supershear transition of rupture speed (Rosakis, Samudrala and Coker 1999; Xia, Rosakis and H 2004). Theoretical and numerical studies had suggested that rupture speed for a shear crack can be higher than the shear wave velocity or below Rayleigh wave velocity depending on the cohesive strength on the fault (Andrews 1976; Burridge, Conn and Freund 1979).

In the case of Duzce earthquake, Bouchon et al., (2001) have observed that the S-P differential arrival time in station BOL to the east of the Duzce rupture was much shorter than expected for a subshear rupture. By comparing the distance and the arrival times of P and S

waves, Bouchon et al. (2001) concluded that the average rupture velocity was 4.3km/s toward east and 3km/s to the west. Bouin et al., (2004) updated the analysis of S-P differential time with an updated hypocenter and came up with 4km/s and have shown that a single fault plane with constant rupture velocity of 4 km/s to the east and 3 km/s to the west of the hypocenter is sufficient to explain the strong-motion and GPS data. Studying the strong-motion data with a single fault plane (Birgoren, Sekiguchi and Irikura 2004) have also suggested faster velocities (4.8 km/s) toward east of the hypocenter compared to west (2.9 km/s). Using empirical Green's functions to analyze high frequency strong-motion generation, (Birgoren, Sekiguchi and Irikura 2004) have come up with lower rupture velocity toward east (3.5 km/s).

Our slip models with various rupture velocity constraints have very similar misfits to the geodetic data. However, the misfits to the strong-motion data do vary with different rupture velocity ranges (Table 4.4). None of the constant rupture velocity models have preferably better fit to the strong-motion data. When all available data is taken into account, we infer that there is no "best fit" constant rupture velocity.

On the other hand, the variable rupture velocity models V_R2.5-4 (V_R 2.5 to 4 km/s) and V_REf_Ws (V_R east fast, west slow) fit the strong-motion data much better. This is not surprising since there is less constraint on the rupture velocity; hence there is more freedom in the model. However, fits to the strong-motion data show that most of the higher misfit of these constant rupture velocity models is due to the station BOL (Figure 4.6a). BOL is the station to the east of the fault, and former studies of supershear rupture observations were based on this station. A careful examination of frequency content of the near-field records from BOL and the shape and timing of the initial phase and stopping phase clearly indicates that a variable rupture velocity is required to explain the horizontal components of the seismogram at BOL. V_R2.5-4 can have both supershear and subshear rupture speeds all along the fault, while V_REf_Ws is allowed to have supershear rupture speeds only toward the east from the hypocenter. The fact that both models fit the BOL station waveforms with similar quality shows that supershear rupture to the west of the hypocenter is not necessary. This observation is consistent with former studies of this event (Birgoren, Sekiguchi and Irikura 2004; Bouchon et al., 2001; Bouin et al., 2004). The major difference is that we have used strong-motion data with additional constraints and more realistic fault geometry. With all these constraints, our models where only supershear rupture was allowed toward east (3.5km/s-4.5

km/s) and subshear toward west (2.5km/s-3km/s) could not explain the records of BOL. For the eastern part of the fault a range of rupture velocities that varies from subshear to supershear is required to fit the waveforms at BOL. We have also tested models where the slip was allowed to be extremely rough to explain the BOL data, but roughness in slip was not sufficient to fit the waveform from this station.

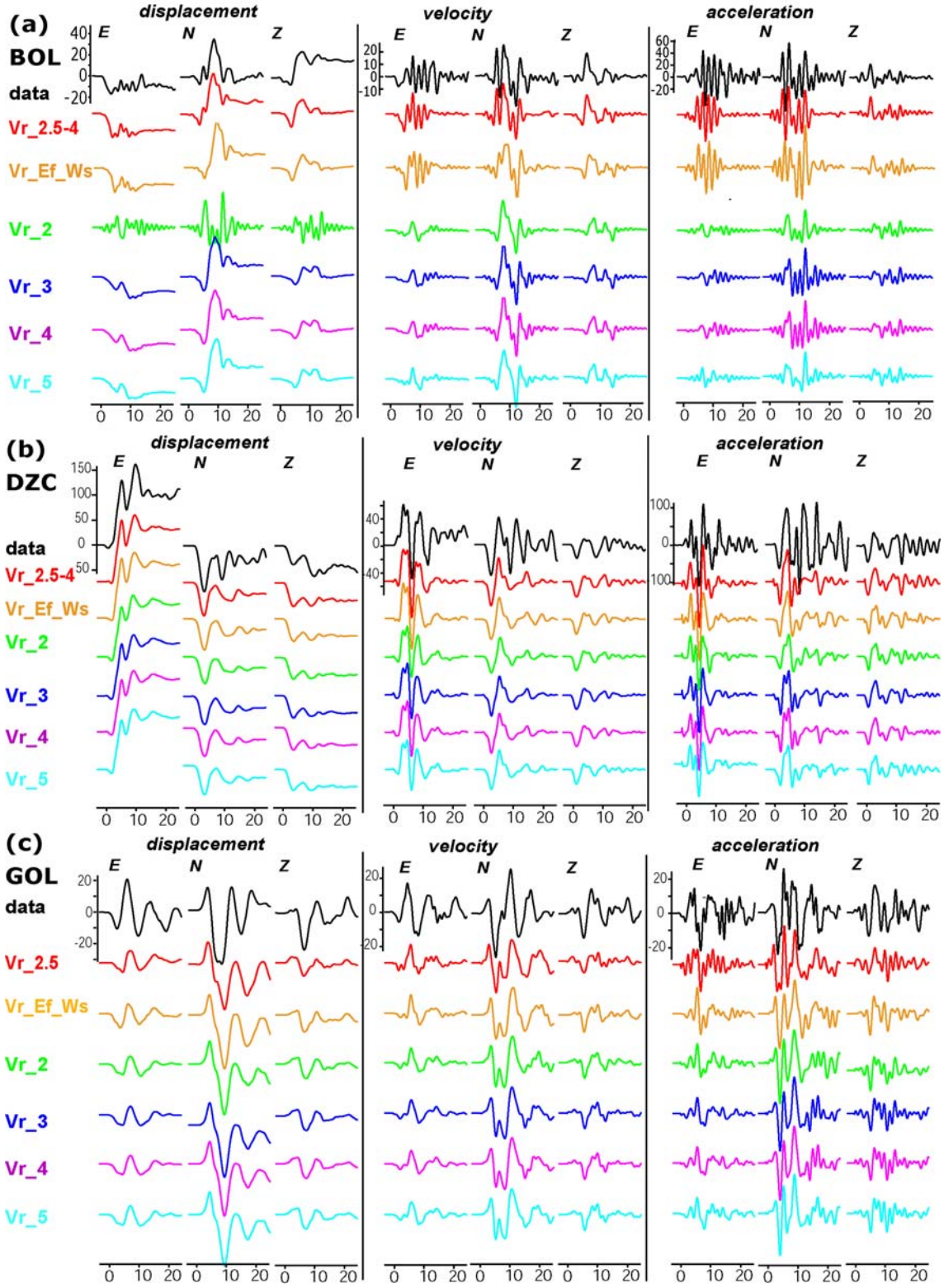

Figure 4. 6 Fits to the strong-motion stations (a) BOL, (b) DZC (c) GOL, see Figure 1b for the station locations. See Table 4 for the explanation of model labels.

The fits to the two other near-field stations, DZC and GOL are shown in Figure 4.6b-4.6c. We chose not to show the fits to the data from GOL station since it is further away, and does not give much information about the rupture. In any case, all of the models fit this station well. The fits to the near-field stations DZC and GOL are of the same quality independent of the rupture velocity constraint. This can be due to local trade-offs between rupture velocity and rise time. The most significant difference between using different rupture velocities is that the rupture front should arrive to stations at different times from the hypocenter. Since the strong-motion stations that recorded Duzce earthquake did not have GPS clocks or reliable timing, absolute arrival time is not part of the strong-motion waveform modeling. The waveform modeling without absolute timing can only resolve the differences of seismic waves arriving after the arrival time. For the stations that are right on the fault, the waveforms record a very local story of the rupture; therefore, rupture velocity does not play a significant role in the shape of the waveform except the actual arrival time. So the waveforms from stations right on top of the fault zone are more sensitive to the details of the rupture's behavior at the local site and the local structure. Since BOL station is off the fault, and affected by broader area of the fault zone, it is more sensitive to the variations in rupture velocity. Moreover, since the slip pattern is constrained from geodetic data; the trade-offs in rise time are not sufficient to explain the observed waveform arrivals at BOL. These constraints produce a particular sensitivity to the rupture velocity. Hence the observed sharpness in waveform, the amplitudes and the frequency content of the seismogram at BOL require rapidly varying rupture velocity toward east.

Based on these arguments, we infer that the rupture speed is highly variable to the east. Variability in rupture velocity has been reported where appropriate dataset was available and rupture velocity variation was allowed in rupture studies (Bouchon et al., 2002; Cotton and Campillo 1995a; Hartzell and Heaton 1983; Ji, Wald and Helmberger 2002c; Olsen, Madariaga and Archuleta 1992), and is also evident in the case of Duzce earthquake. Figure 4.7 shows the map view of our best fit (V_REf_Ws) model with time contours and shows the accumulated slip in 2 second time intervals as the rupture propagates (b). In the first two seconds of the earthquake, the rupture accumulates moderate amount of slip just to the east of the hypocenter, from 2 to 4 seconds there is more slip but rupture velocity is around 3 km/s. Significant slip accumulation and acceleration of the rupture to the east occurs in 4-6 second

window, where locally rupture velocity is more than 4 km/s, while the western segment does not accumulate much slip. In the 6-8 second window the rupture already reaches to 29 km to the east. Then the rupture stops, while mostly shallow portions of the fault still keep on sliding in up to 12 seconds.

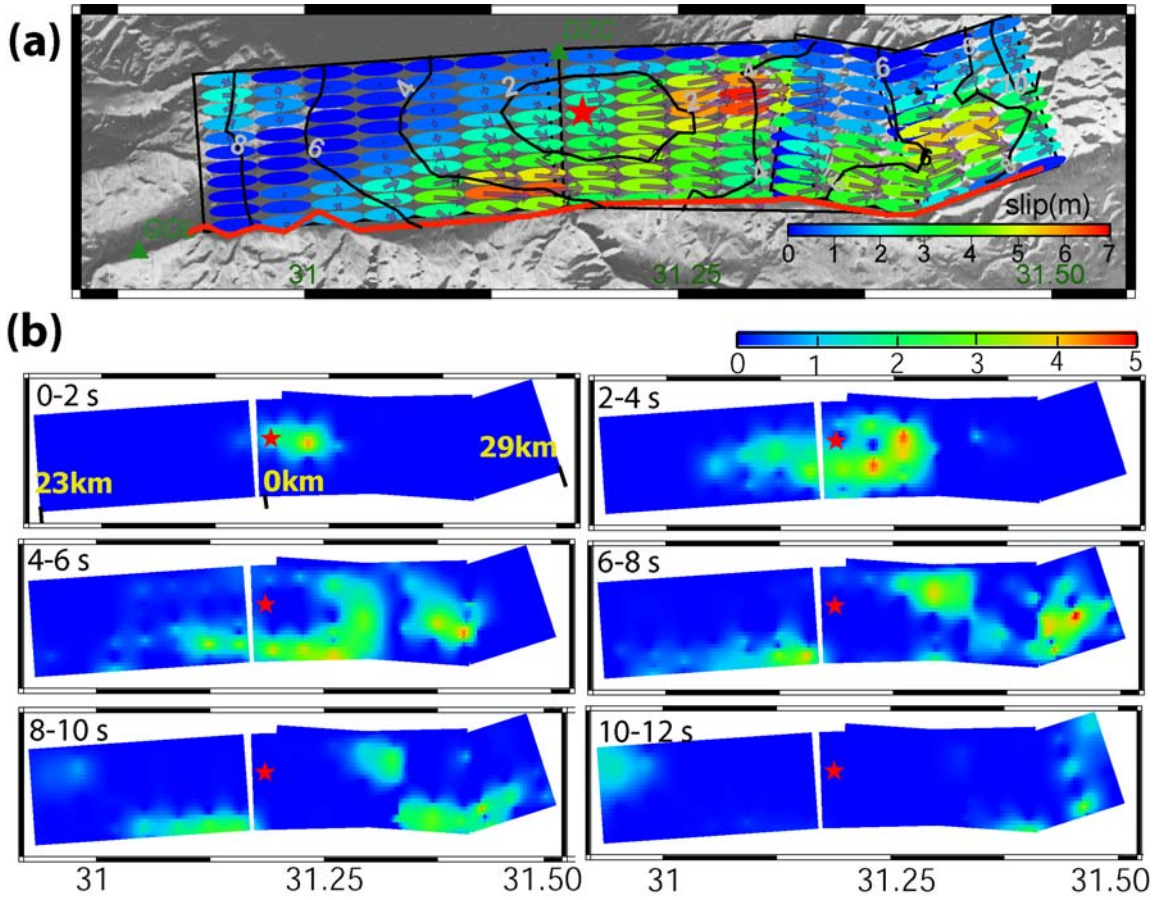

Figure 4.7 (a) Map view of preferred model with rupture contours every two seconds. (b) Map view of slip accumulated in 2 second time windows.

Overall the rupture speed is around 3.7-3.8 km to the east, while it is around 3 km/s to the west. Considering that the slip is confined to top 11 km, and S velocity is around 2.5 to 3.5 km down to these depths (Table 4.3), we confirm that supershear velocities have occurred to the east during the Duzce earthquake. In addition, rapid variations in rupture velocity are required to explain all the available data.

It should be noted that although the analysis is done with the most available data and most accurate geometry, using 1-D velocity model for our models can affect the results and

our inferences. However, the amplitudes, timing of the pulses, frequency content and the total duration of the record at BOL are not likely to be explained with changes in the velocity model alone, considering the compactness of the rupture pattern. Although changes in velocity structure do exist, fast rupture velocity is necessary to fit the seismograms at periods greater than 1 second.

4.7 Prediction of teleseismic data from the near-field Data

One of the focuses of this study was to integrate all the available data into the study of the Duzce earthquake. Since we were interested in the variations of rupture speed and details of the near-field seismograms, we refrained from including teleseismic data into the exploration of rupture speed. Instead, we predicted the far-field seismograms from our four-segment model of the strong-motion, GPS, InSAR and surface offsets to test whether near-field modeling is consistent with the far-field seismograms (the model VREf_Ws was chosen as the best fit model). This test shows that we can predict the teleseismic data from the geodetic and strong-motion models reasonably well (Figure 4.8). While the predicted waveforms from near-field data have similar waveforms, their timing appears to be misaligned compared to the handpicked arrival times of the waveforms. On average, the predicted teleseismic waveforms are 2 seconds later than the data. Figure 4.8 shows the data and near-field model predictions that are already shifted 2 seconds forward in time.

This observation implies that when earthquakes with small initial slip around the hypocenter are studied using teleseismic waves only, they will be missing the energy from the less energetic initiation of the rupture, since this energy is too little to reach to teleseismic distances. Therefore, in the case of the Duzce earthquake hand-picked arrival times of the teleseismic waves are not coming from the hypocenter, rather it is coming from a more seismic energy producing portion of the rupture that occurs later. This phenomenon has been observed before in the 1989 Loma Prieta earthquake, where both near-field and teleseismic data existed (Wald, Helmberger and Heaton 1991).

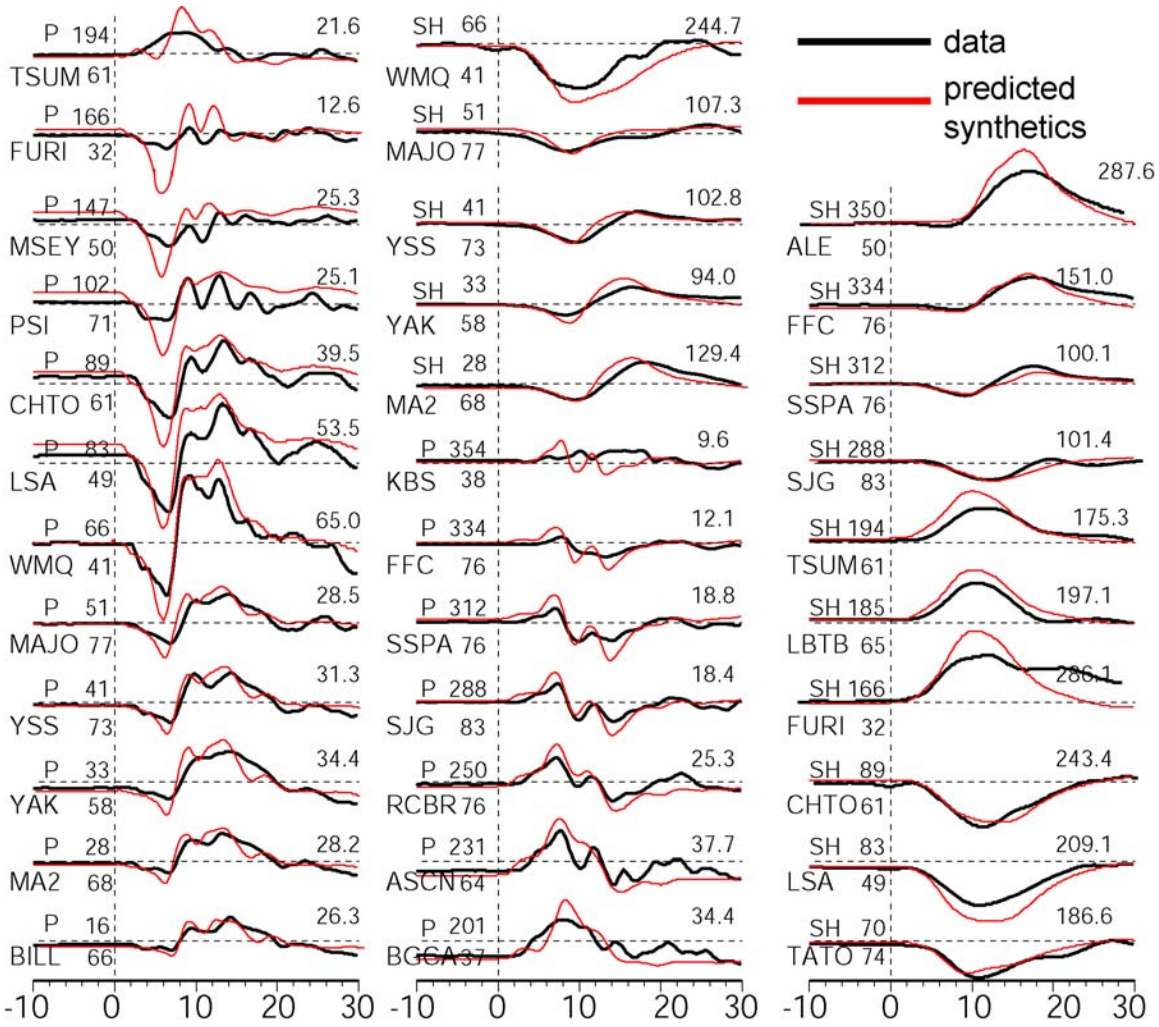

Figure 4.8 The teleseismic data (black), and forward predicted synthetic waveforms (red) from the modeling of strong-motion, GPS, InSAR and surface offsets using four-segment geometry. The data is already shifted 2 seconds to be aligned with synthetics.

Consequently, for the events where the hypocentral area does not accumulate much slip, models based on picking teleseismic arrivals will be more compact with more slip at and around hypocenter. A typical example of this kind of model is shown in Figure 4.9a (third model from top) where handpicked arrival times and strike and dip from Harvard CMT solution was used to model the Duzce earthquake.

4.8 Strong-Motion Estimation using Teleseismic Data and Utilizing Satellite Imagery

In this section we test whether using sub-pixel cross-correlation of images can contribute to the rapid estimation of strong-motions as a future application to improve rapid finite-fault studies after a large earthquake. Satellite imagery provides useful information about the details of the surface break from co-seismic slip. Knowing where the surface rupture is important since it helps refining geometry and estimating damage. If in the future these satellite images can be obtained and processed close to real-time after a large crustal earthquake, they can be utilized for more complicated rapid rupture models.

In order to test the effect of implementing satellite images to rapid teleseismic models, we compare the teleseismic models of Duzce earthquake using four-segment model including surface slip constrains with four-segment finite fault model built by using global CMT (http://www.globalcmt.org) solution (strike 268^{o}, dip 54^{o}) along with the given hypocenter. Figure 4.9a shows the teleseismic model based on CMT solution, Figure 4.9b shows the four-segment model without surface constraints and 9c shows the four-segment model with the surface constraints. When we compare these teleseismic models with the best fit strong-motion and geodetic joint model (Figure 4.7a), it is clear that the teleseismic model that matches best with near-field model is the four-segment model with the surface constraints (Figure 4.9c). All three models fit the teleseismic data very well (Figure 4.10). Figure 4.11 shows the predictions of strong-motion from the three teleseismic models of Figure 4.9. In order for these predictions to be more realistic, we have calculated them with a single Green's function using the model of (Mindavelli and Mitchell 1989) from Table 4.4, since in rapid estimations, station corrected Green's functions would not be available. The comparison shows that the stations to the west of the hypocenter (GOL and SKR) are predicted with much higher quality when four-segment SPOT based geometry is used (Figure 4.11). The data from DZC, right around the hypocenter, is predicted with similar quality with all three models. None of the models can explain the peculiar records from BOL station. This is not surprising since modeling the data from BOL requires very detailed near-field modeling as seen in this study. The addition of surface constraints does not improve the predictions significantly for the case of Duzce earthquake.

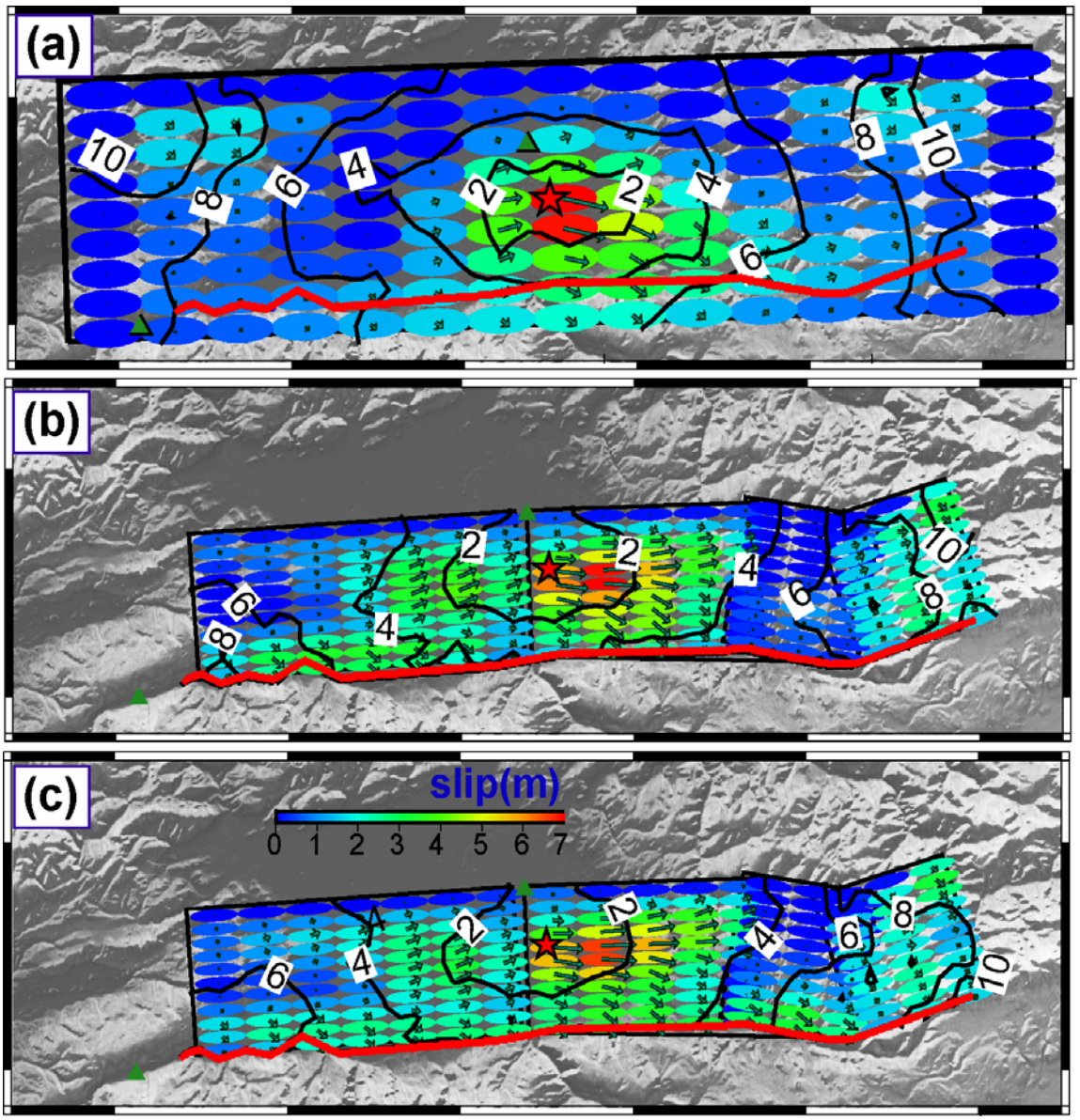

Figure 4.9 The map view of models (a) four-segment teleseismic inversion from top to bottom.(b) four--segment geometry, teleseismic inversion, and (c) four-segment geometry, teleseismic inversion with surface constraint

Overall, predictions of strong-motions from teleseismic data are possible; and additional constraints from satellite imagery can be very useful. The model with additional information from SPOT images improves the model significantly. However, far-field data cannot resolve the details of earthquake dynamics and rupture propagation; therefore the details of these

seismograms cannot be expected to fit perfectly. Moreover, the rapid estimations have to rely on a predetermined velocity model, which is not always suitable to explain all the sites of strong-motion data.

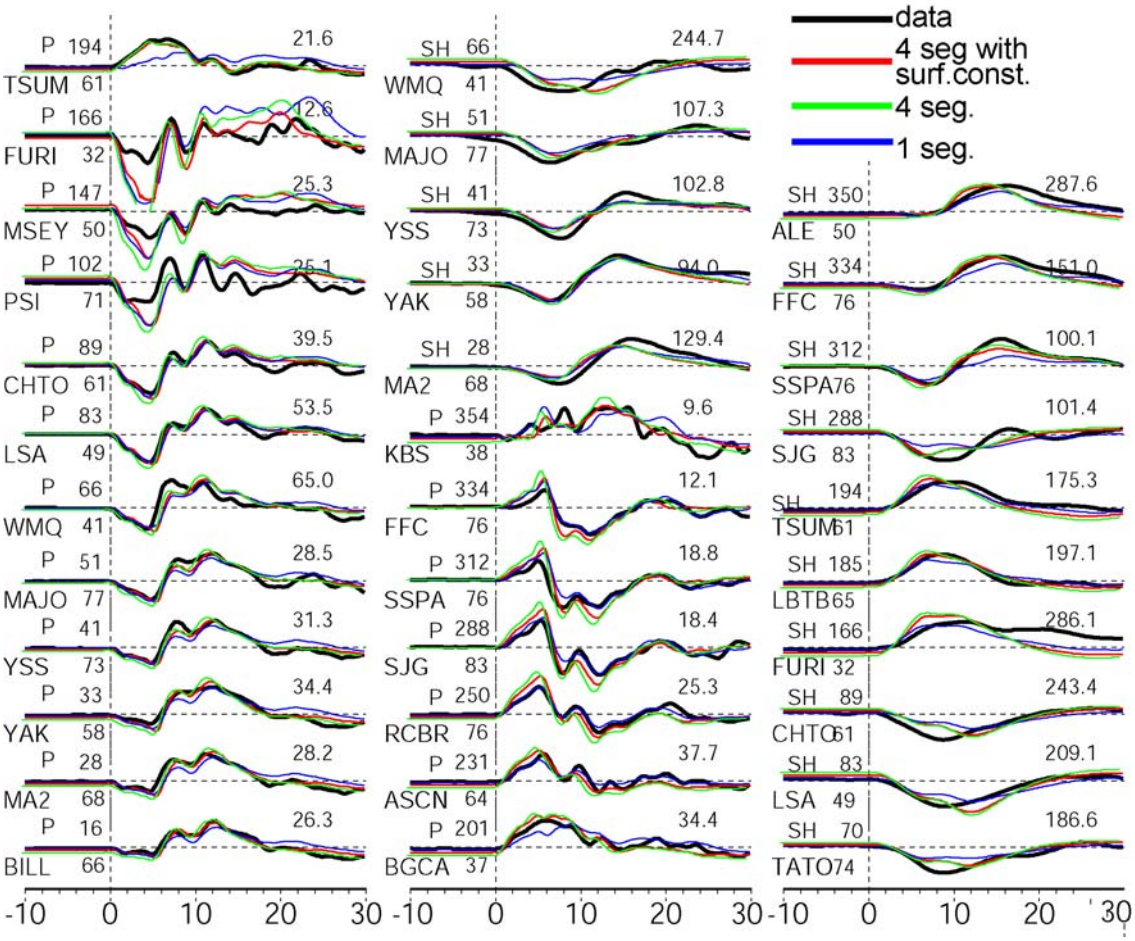

Figure 4.10 Fits to the teleseismic data for the three teleseismic models in Figure 4.9.

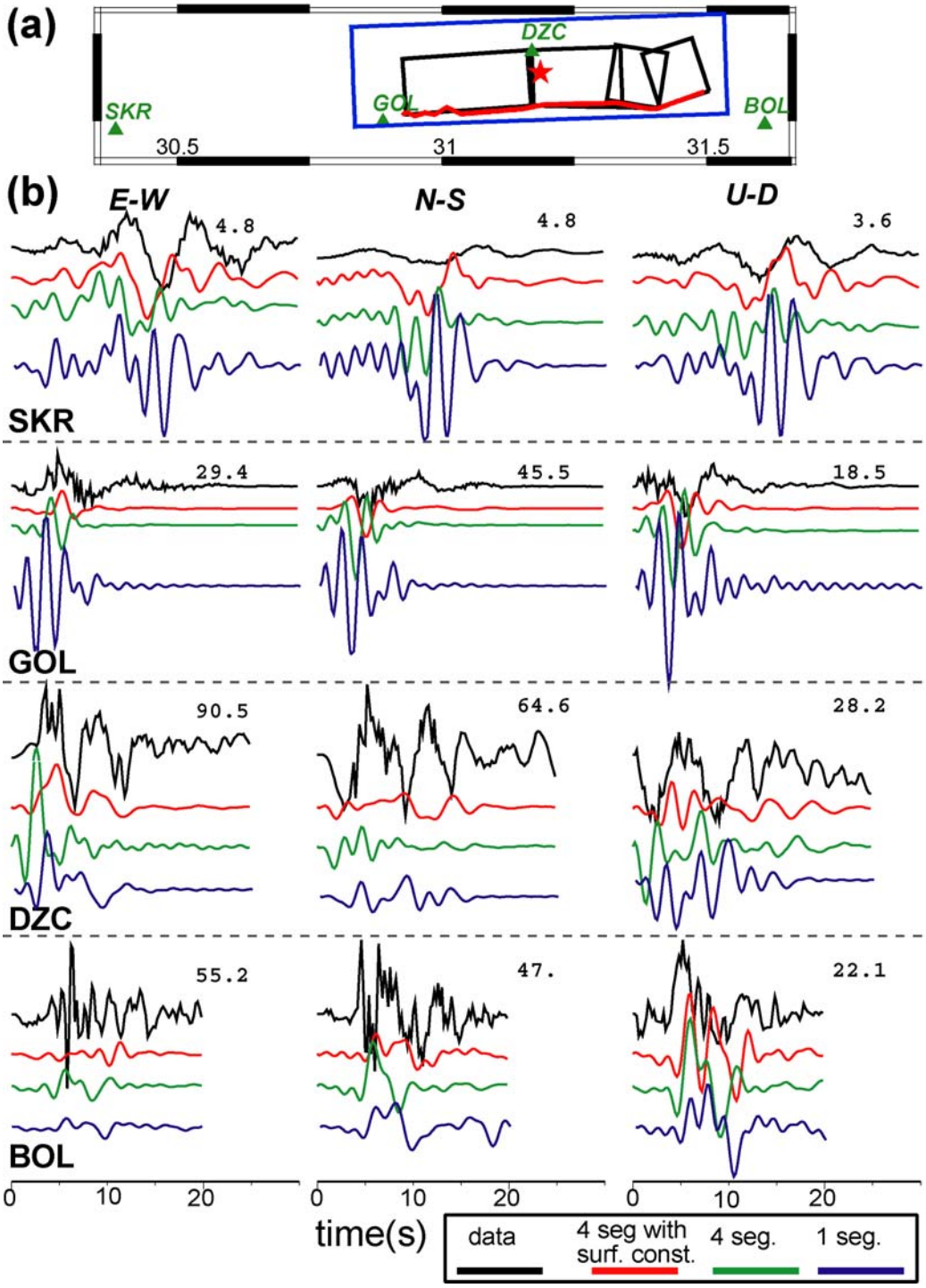

Figure 4.11 (a) The geometry of the 2 models and the locations of strong-motion stations (b) Predictions of strong motion data from one-segment and four-segment models.

4.9 Conclusion

We have successfully obtained the fault map of Duzce earthquake by using SPOT images before and after the event. SPOT obtained fault map agrees with the field studies; in addition, an extra strand of rupture to the east has been discovered. The offsets from SPOT images agree with the field studies, except the western end where post-seismic of Izmit earthquake might have contributed and eastern end where additional rupture was observed with SPOT images.

By using four-segment fault geometry and constraining the surface offsets using satellite imagery, we modeled the Duzce earthquake using strong-motion, GPS and InSAR data. We have constrained the rupture velocities to various values and ranges. Our results show that due to constraints from the geodetic data, using different rupture velocity constraints do not change the obtained slip on the fault significantly. None of the constant rupture velocity models can explain the record from BOL station. The only way to explain this data is to let the eastern strand of the fault have variable rupture velocity from sub-shear to supershear rupture speeds. The western part of the fault does not need to have supershear rupture speeds. Our preferred model shows that the rupture starts slow toward east, accelerates to supershear speed and slows down again toward the end of the fault, while it is always subshear toward west.

The teleseismic data were estimated from the joint models of near field data successfully. However, 2 seconds time shift had to be applied to the recorded seismograms with respect to their handpicked arrival time to align with the synthetic waveforms. The beginning of the earthquake does not create seismic energy that is observable in the far field; hence the teleseismic arrivals are not actually coming from the hypocenter. This leads teleseismic models to become more compact than the actual slip.

We have estimated near-field ground motion data from the far field data using handpicked arrival times and 1-D velocity structure. We have compared the models where the geometry was constrained with satellite imagery with constraints of surface offsets with the geometry from global CMT catalog. Although all the models fit the teleseismic data with similar quality, the model with more realistic geometry and surface offset constraints look most similar to the near-field model of the Duzce earthquake. Estimations of near field seismograms

are also improved with utilization of satellite imagery. In the near future, using satellite imagery for rapid hazard and source estimations might prove to be an important addition to the real time earthquake studies.

4.10 Acknowledgement

My collaborators in this study were Sebastien Leprince, Jean-Philippe Avouac and Don Helmberger.

CHAPTER 5: THE 2005, M_W 7.6 KASHMIR EARTHQUAKE: SUB-PIXEL CORRELATION OF ASTER IMAGES, SEISMIC WAVEFORM AND SAR ANALYSIS

5.1 Abstract

We analyze the M_w7.6 Kashmir earthquake of October 8, 2005, using sub-pixel correlation of ASTER images to measure ground deformation, and modeling SAR imagery data along with seismic waveforms. The surface rupture is continuous over a distance of 75 km and cuts across the Hazara syntaxis reactivating the Tanda and the Muzaffarabad faults. North of Muzaffarabad the surface rupture coincides approximately with the Main Boundary Thrust, on the southwestern flank of the syntaxis, although the two faults have opposite dip angles. The rupture terminates abruptly at the hairpin turn of the Main Boundary Thrust Fault, showing a strong structural control. The fault surface offset is 4 m on average and peaks to 7 m northwest of Muzaffarabad. The rupture lasted about 25s and propagated up-dip and bilaterally by ~2 km/s, with a rise time of 2-5 s. The shallowness and compactness of the rupture, both in time and space, provide an explanation for the intensity of destructions. We compare the teleseismic models with and without the geometry and offsets to the SAR models. We infer that Satellite image correlation put constraints on teleseismic models, which lead to more coherent models with the geodetic data. This kind of analysis could be achieved as soon as a post-earthquake image is available and would provide key information for early assessment of damages.

5.2 Introduction

The M_w 7.6 earthquake, which struck Northern Pakistan and Kashmir on October 8, 2005 claimed 80,000 lives. This is to date the most devastating earthquake to have occurred along the Himalayan arc. Some earthquakes in the twentieth century have probably approached or exceeded M_w 8, in particular the 1934 Bihar-Nepal and the 1905 Kangra earthquakes (Bilham 2004), but they did not cause as many casualties as the 2005 event (Figure 5.1). This is a sad

reminder that seismic vulnerability has risen critically over the last few decades due to the growth of the population in the region and probably insufficient awareness of seismic hazard (Bilham, Gaur and Molnar 2001).

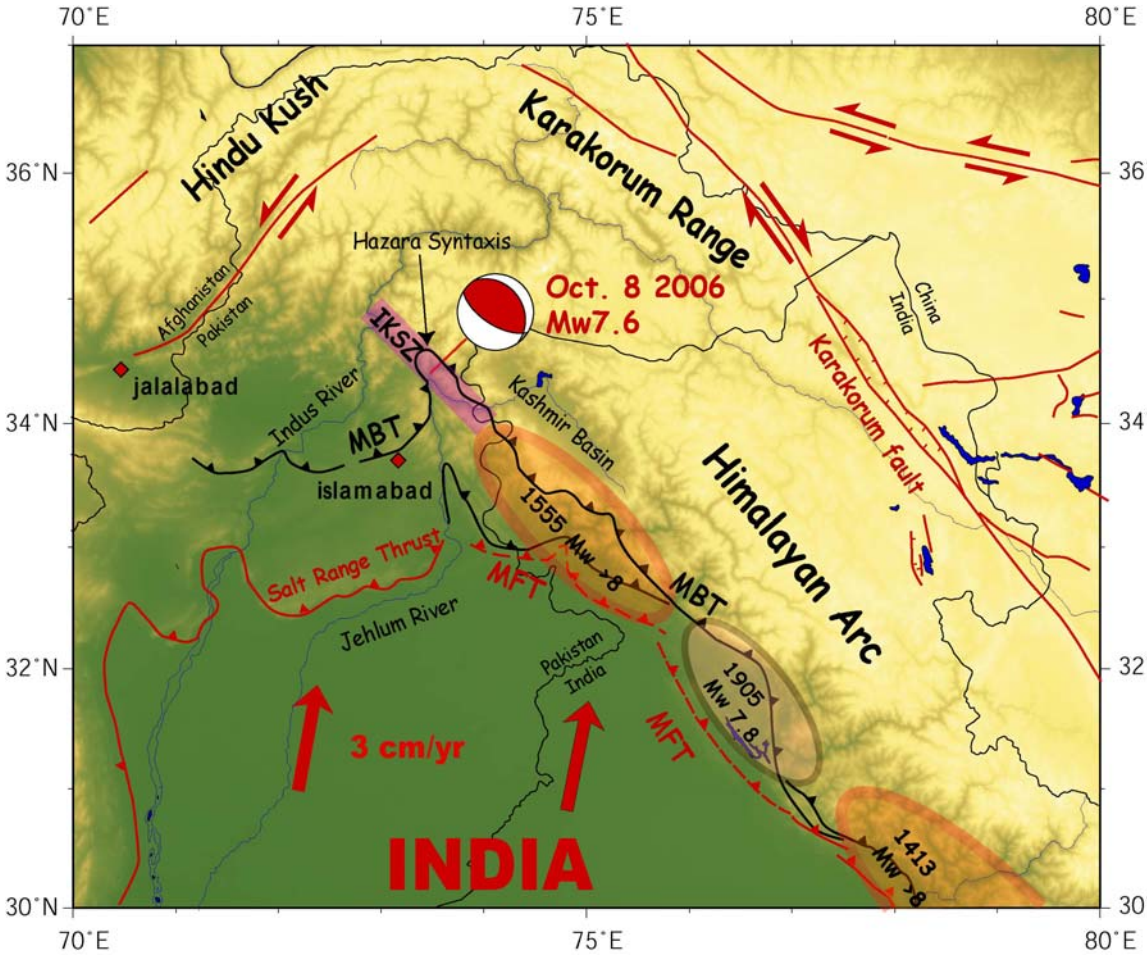

Figure 5.1 Tectonic setting of the October 28 2005 Kashmir earthquake. Rupture areas of major Himalayan earthquakes documented from historical studies (Bilham 2004) and paleoseismic investigations (Kumar et al., 2006). Shaded ellipses show estimated locations of ruptures in 1413, 1555 and 1905. Major active faults, modified from (Yeats et al., 1992) and (Kumar et al., 2006), are shown in red. Dashed lines indicate approximate location of blind thrust faults. Velocity of peninsular India relative to stable Eurasia computed from the Euler pole of the Indian plate determined by (Bettinelli et al., 2006). MFT: Main Frontal Thrust fault. MBT: Main Boundary Thrust fault. IKSZ: Indus Kohistan Seismic Zone (Seeber, Armbruster and Quittmeyer 1981).

Here, we report investigations of ground deformation in the epicentral area using optical images, SAR images and by combining this information with an inversion of teleseismic body waves. Our analysis of this particular event brings important information on the characteristics of Himalayan earthquakes, sheds light on the active tectonics of the western syntaxis, and opens the way to a new approach for early assessment of damages.

5.3 Remote sensing analysis

We measured ground deformation in the epicentral area from the sub-pixel correlation of ASTER images acquired on November 14, 2000 and October 27, 2005 (Figure 5.2). We use a new procedure (Leprince et al., 2007) adapted from a previous approach that had been designed specifically for processing SPOT images (Van Puymbroeck 2000) and which has been applied to a few events since (Binet and Bollinger 2005; Dominguez, Avouac and Michel 2003; Feigl et al., 2002; Michel and Avouac 2002). A similar approach has been recently applied to ASTER images on the Kokoxili earthquake, yielding mitigated results (Schiek and Hurtado 2006).

The images are orthorectified on a common 15m resolution grid using a DEM computed from a stereo pair of ASTER images. Offsets are then measured from the local cross-correlation of the two orthorectified images. Uncertainties on the imaging system, in particular on the satellite orbit and attitude, and on the topography can lead to apparent offsets unrelated to ground deformation. The satellite viewing parameters are optimized to minimize these artifacts. This process partially removes the deformation at long wavelengths, which trade-off with satellite viewing parameters, but significantly enhances the performance of the sub-pixel correlation technique for the measurements of deformation at short wavelengths (Leprince et al., 2007). The resulting offset field is therefore a reliable measurement of ground displacement at shorter wavelengths (typically a few kilometers).

Our measurements reveal a clear discontinuity which can be traced over a distance of about 75km in the offset field both on the north-south (Figure 5.2) and east-west components. Despite the five-year interval between the two images, the correlation is good, except at locations where major landslides were triggered by the earthquake. We analyzed a second pair of ASTER images (AST_L1A.003:20030303221 of April 30, 2001, AST_L1A.003:20031782375 of November 19, 2005) to evaluate the possible continuation of

the rupture to the southeast, and found that the fault trace can not be traced beyond the area covered by the first pair of images.

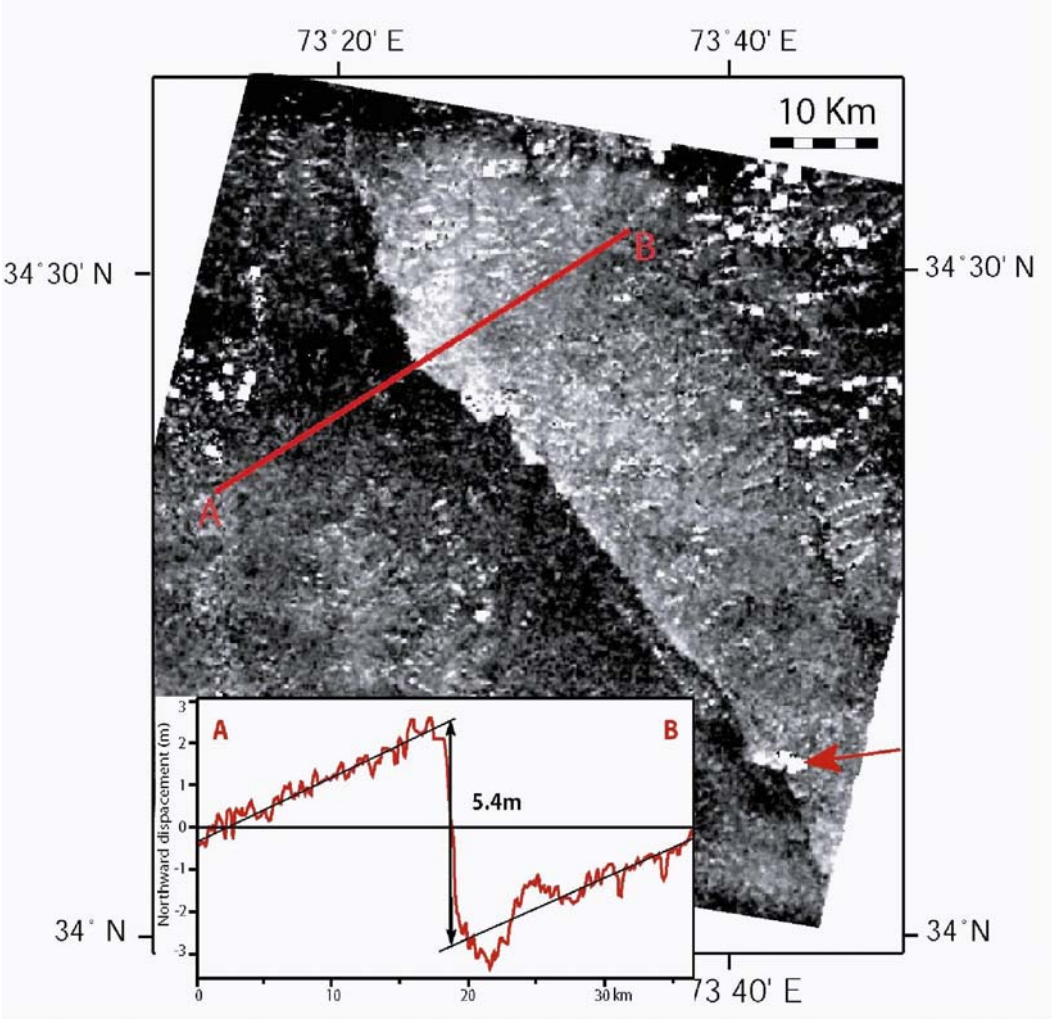

Figure 5.2 Displacements measured sub-pixel correlation of ASTER images. Northward ground displacements (white to the south, black to the north), determined from the correlation of ASTER images, with a 15-meter ground resolution, taken on November 14, 2000 (AST_L1A.003:2003527667) and October 27, 2005 (AST_L1A.003:2031572195). The image was obtained with a sliding 32x32 pixels correlation window and 8-pixel step. Ground resolution on the correlation image is 120m. No measurement is assigned to white points, where the correlation is lost or where outliers (where the measured ground displacement was found to exceed 10m) have been filtered out. Correlation is lost mainly due to landslides or variation of the snow cover. For example, the red arrow points to an area where the correlation is lost due a major landslide. The inset shows the profile of the NS component of ground displacement obtained by stacking all measurements within a 9 km wide swath centered on profile AB

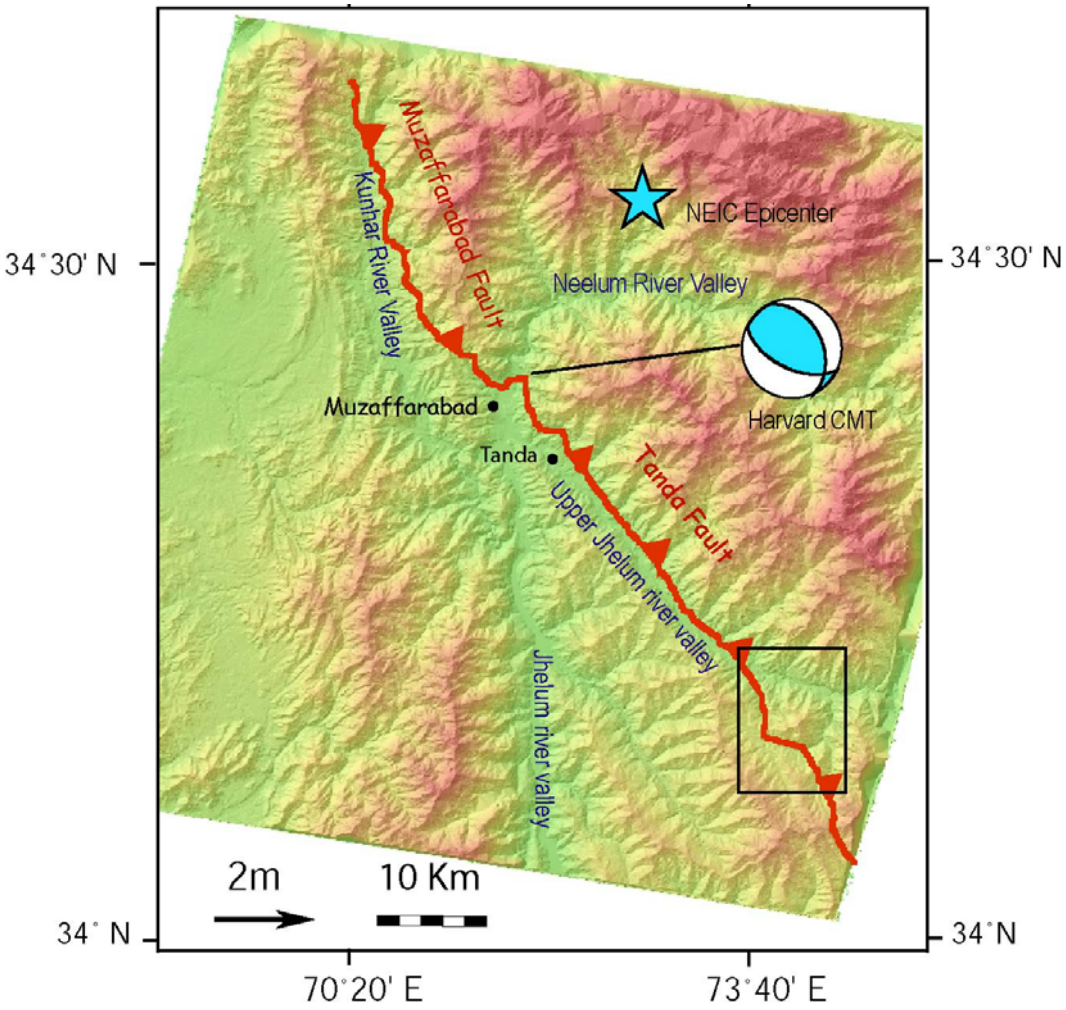

Figure 5.3 Surface fault trace mapped form the discontinuity of the offset field (Figure 5.2). The rupture geometry across the Neelum river and south of the Jehlum river valley (Box) indicates a shallow, ~10º, dip angle near the surface.

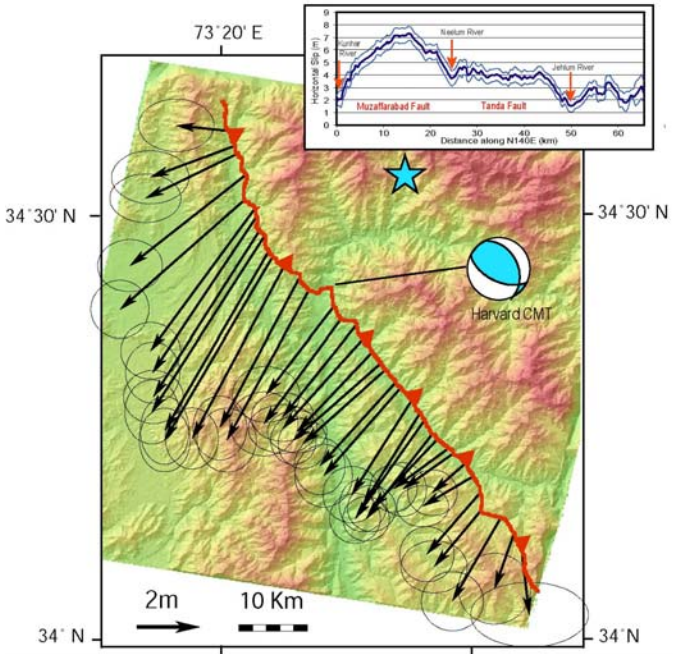

Figure 5.4 Surface offsets mapped form the discontinuity of the offset field. The inset shows the horizontal offset along the fault.

The horizontal slip vector on the fault can be measured accurately from profiles run across the fault trace (Figure 5.2 inset). The discontinuity is sharp, with deformation localized within a zone no wider than a few hundred meters. It clearly indicates that the rupture reached the surface, as confirmed by field investigation (Yeats and Hussain 2006) and also inspection of high resolution optical images. Along the upper Jhelum valley the fault trace is remarkably linear and follows the northeastern flank of the valley for about 30km north of Muzaffarabad along the previously mapped Tanda fault (Nakata et al., 1991; Figure 5.3). The fault trace curves and becomes more irregular where it joins the Muzaffarabad fault and cuts across the Kunhar valley. The irregularity of the fault trace to the north is mainly due to the roughness of the topography. The spatial variation of intersection of the fault trace with the topography shows a northeast dip angle. In particular, the fault trace makes a clear "v" across the Neelum river valley (Figure 5.3), and where it cuts across a topographic ridge southeast of the upper Jhelum river valley (box in Figure 5.3). From these geometries the near surface dip angle appears to be about of 10º.

Horizontal slip vectors were determined about every 2 km along the fault trace from the discontinuity of ground displacement measured along profiles run across the fault (Figure 5.4). The amplitude of the horizontal slip vector reaches a maximum of 7.15+/-0.4m about 10 km northwest of Muzaffarabad (Figure 5.4). We observe a local minimum at the junction between the Tanda and the Muzaffarabad faults. Surface slip varies quite significantly along the Muzaffarabad fault and tapers abruptly at the northern end of the rupture with a steep gradient of about one meter per kilometer over a distance of about 5 km. Along the straight fault segment of the Tanda Fault the horizontal slip is nearly constant, around 4 ± 0.8 m. As the rupture approaches its crossing of the Upper Jhelum river, slip diminishes to just 1.5m, again at a rate of about one meter per kilometer. In the hills further south, slip magnitude rises as high as 3.5m, but has much more variability. The rupture is nearly pure dip-slip as the azimuth of horizontal slip motion is on average N41ºE, nearly perpendicular to the 138º E average strike of the fault trace.

5.4 Seismological Analysis

The Global CMT solution, determined from the modeling of the long period surface waves yields a northeast dipping fault plane striking N133 º E, with a rake of 123 º, and a dip angle of 40º (http://www.globalcmt.org/) (Figure 5.4). The corresponding seismic moment is 2.94 10^{20} N.m. Given the relatively shallow hypocentral depth, the dip angle is not well constrained from the long period surface waves. For comparison, the focal mechanism determined by the USGS from body waves indicates a fault strike of 133º E, a rake of 140º, and dip angle of 29º (http://neic.usgs.gov). These source parameters are consistent with the N138 º fault strike and imply a somewhat larger strike-slip component of slip than the surface slip vectors determined from the remote sensing analysis. They do however require a dip angle larger than that inferred from the geometry of the fault trace at the surface, suggesting that the fault dip angle increases with depth.

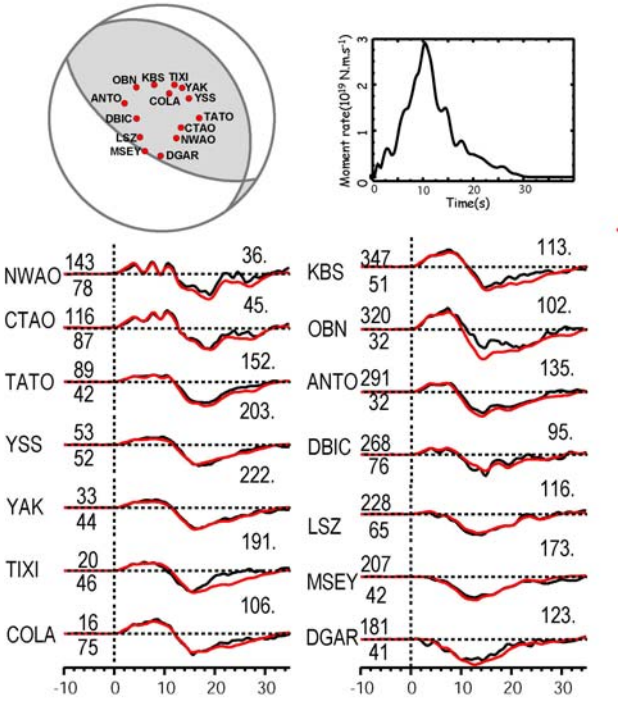

Figure 5.5 Modeling of teleseismic waveforms (P waves) using the source model derived form the joint inversion of waveforms and surface slip. Measured (black) and modeled (red) seismograms. The location and the stations with respect to the focal mechanism representation of the finite source model is shown on top left. The moment release time function is shown on top right.

We have determined a finite source model from the modeling of teleseismic waveforms, in the 0.01-1Hz frequency band, following the procedure of (Ji, Wald and Helmberger 2002a). Fault geometry with two fault segments, a 60 km long southern segment striking 320°, and a 15 km long northern segment striking 343° was constructed based on the surface break derived from our remote sensing analysis. The slip vectors on the subfaults closest to the surface were constrained to fit the surface slip measurements to within 2σ. We selected a set of P-wave records providing the best possible coverage in azimuth and distance (Figure 5.5). We tested various dip angles between 25° and 40° and found that the polarity of the P and S wave first motions were best adjusted with a dip angle of 29°, consistent with the USGS determination, but about 10 degrees less than global CMT solution. We used the USGS epicenter, which is accurate to about 20km, to estimate the rupture initiation depth. Given the fault geometry, as defined from the fault trace at the surface and the best fitting dip angle, this assumption implies a hypocentral depth of 11 km. The best fitting model shows a simple source with a relatively compact high-slip zone spanning the Tanda and Muzaffarabad faults and mostly up-dip of the nucleation point (Figure 5.6). The preferred model has a nearly constant rupture velocity of about 2 km/s and a short rise time between 2 s and 5 s (Figure 5.6). Forcing rise times to be longer than 5s degrades the solution (the misfit to the waveforms increases from 17.5% to 20.8%), despite the trade-off with rupture velocity. The focal mechanism representation of our finite source model is close to the Harvard CMT (Figure 5.6), and the released moment is 2.82×10^{20} N.m, only 4% smaller. This shows that our source model is consistent with the source model derived from the surface waves.

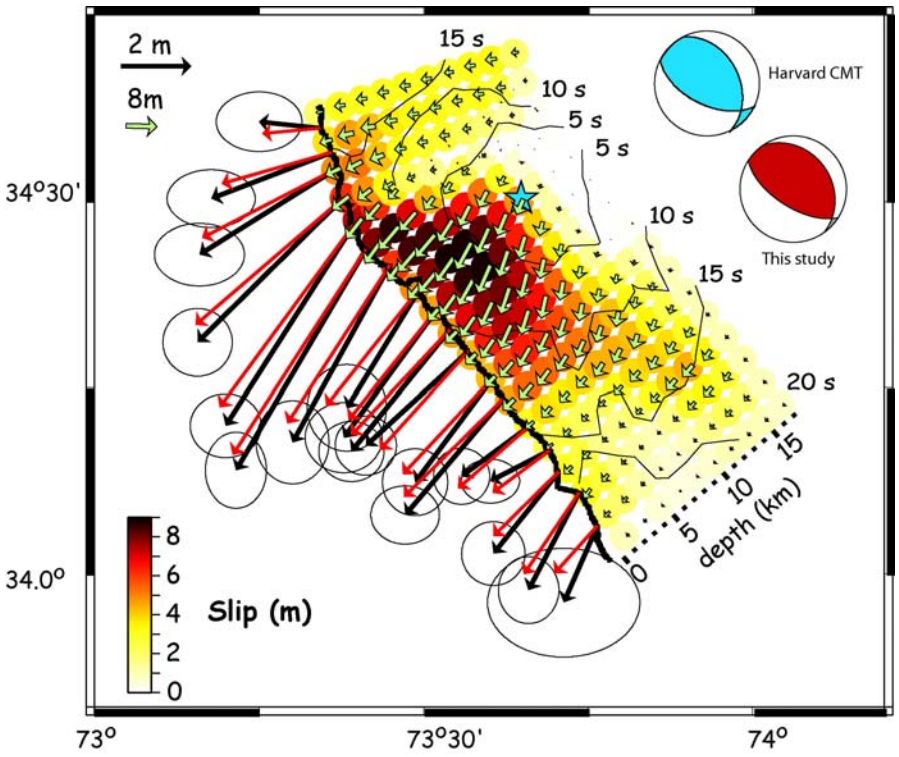

Figure 5.6 Slip distribution with isochrones derived from the seismic waveforms and surface slip distribution. The fault geometry consists of two planar fault segments following the fault trace, subdivided in the horizontal and down-dip direction in 2km by 3km cells. The star shows the location of the nucleation points, on the fault plane, assumed to coincide with the USGS epicenter. Seismic waveforms and surface displacements are computed in a layered half space with a 1-D crustal model interpolated from CRUST2.0 (Bassin, Laske and Masters 2000). Horizontal slip vectors measured along the surface fault trace (black arrows with 2σ uncertainty ellipses) are compared to the theoretical displacements (red arrows) computed using the method of (Xie and Yao 1989). Green arrows show slip vectors on the fault plane at depth. The double-couple component of the seismic moment tensor computed from the summation of the seismic moment of each subfault of our model (red) is compared with the Harvard CMT (blue).

5.5 Discussion

5.5.1 Performance of the sub-pixel correlation of optical images

Despite the 5 year time difference between the two ASTER images, their sub-pixel correlation has provided a detailed description of the surface slip distribution with accuracy

not achievable by other techniques. Near the near fault zone, our technique performs better than SAR interferometry because the coherence of SAR is often lost due to too high strain or the effect of ground shaking, or because the fringe rate exceeds the limit of one pixel-per-fringe. Cross-correlation of SAR amplitude is an alternative approach (Michel 1999), but in the present case the accuracy is not as good as what we have obtained with the optical images (Fujiwara et al., 2006; Pathier et al., 2006). The correlation of SAR amplitude images does however provide constraints on the vertical component of displacements which are not accessible from optical images. Compared to field investigations, our technique provides the two components of horizontal surface slip, whereas the component of displacement normal to the fault trace is generally difficult to measure in the field, and also, it takes into account deformation off the main fault trace that is generally missed during field surveys.

5.5.2 Characteristics of the seismic rupture

The 2005 Kashmir earthquake appears to be a simple shallow crustal event with a relatively compact slip distribution, a standard sub-shear rupture with a rather short rise time. The up-dip propagation of the rupture together with its steep dip angle and shallow distribution of slip must have contributed to the heavy damages in the near-field. This event shares some similarities with the 1999, Chichi M_w 7.6 earthquake, for which a well constrained slip model has also been obtained from the joint analysis of geodetic and seismic waves (Ji et al., 2001) and which ruptured a thrust fault along the western foothills of Taiwan in a tectonic setting very similar to that along the Himalayan front. In both cases, the rupture nucleated on the bottom edge of the asperity, and was restricted at depth shallower than about 15km on relatively steep thrust faults. The shallow depth of the slip distribution is consistent with the view that deformation becomes dominantly aseismic at depth greater than about 15 km due to the transition from stick-slip to stable frictional sliding as temperature rises above 250-300 ºC (Avouac 2003; Scholz 1990). The short rise time of just 2-3s, is also a characteristic of both the Kashmir and the Chichi events, and seems typical of intracontinental events as shown from other case examples of joined inversion of seismic waveforms and geodetic data (Delouis et al., 2002; Hernandez, Cotton and Campillo 1999; Ji, Helmberger and Wald 2003). By comparison, subduction events have similar rupture velocities, but seem to be characterized by much longer rise times, and hence produce less severe ground shaking (Konca et al., 2007). Finally, we

notice that the Kashmir earthquake nucleated near the junction between the Tanda and the Muzaffarad faults.

The Kashmir earthquake creates an opportunity to search for how addition of various datasets can contribute to the earthquake model. Common practice for rapidly modeling large earthquakes involves building one-segment fault plane geometries based on the hypocenter from USGS and strike and dip from global CMT (http://www.globalcmt.org/). Therefore, we start with modeling the Kashmir earthquake using teleseismic P-waves from the IRIS data center with a single plane geometry based on Global CMT solution (strike 334°, dip 40°, length 80km). This model has a compact source area, rupturing up-dip with some directivity toward south. However, the fault geometry does not match the observed field offsets from ASTER data (Figure 5.7a).

Next, we model teleseismic P waves using a 2-segment fault geometry based on image cross-correlation, instead of geometry based on global CMT solution (Figure 5.7b). Since the hypocenter is the same, the dip angle has to be modified to fit the surface exposure of the fault. This model is also a too compact slip distribution which does not fit the rupture length and the observed surface offsets neither to the north, nor to the south of the hypocenter.

Subsequently, we model seismic waves with 2-segment geometry with constraining the slip on the shallow subfaults based on the observed horizontal offsets, this model is the same model in Figure 5.6. When the surface constraints are introduced, the solution has much more shallow slip, and the slip around the hypocenter is less. The fits to the seismic data are of same quality (Figure 5.8a-c).

Finally, using 2-segment geometry with constraints on the surface offsets, we model teleseismic data along with SAR data jointly. Since the source region had very rough topography, typical SAR interferometry was not applicable, so the SAR images before and after the earthquake were cross-correlated using the same method that we have used for sub-pixel cross-corrrelation of ASTER images (Pathier et al., 2006). Three image pairs (2 ascending and 1 descending) were used. We have only studied the displacements in range direction. The details and fits to the SAR data are shown in Figure 5.9. This joint model shows that to the south, most of the slip is very shallow. To the north, slip is more distributed with some deep slip; however, the rupture ends quite abruptly (Figure 5.7d).

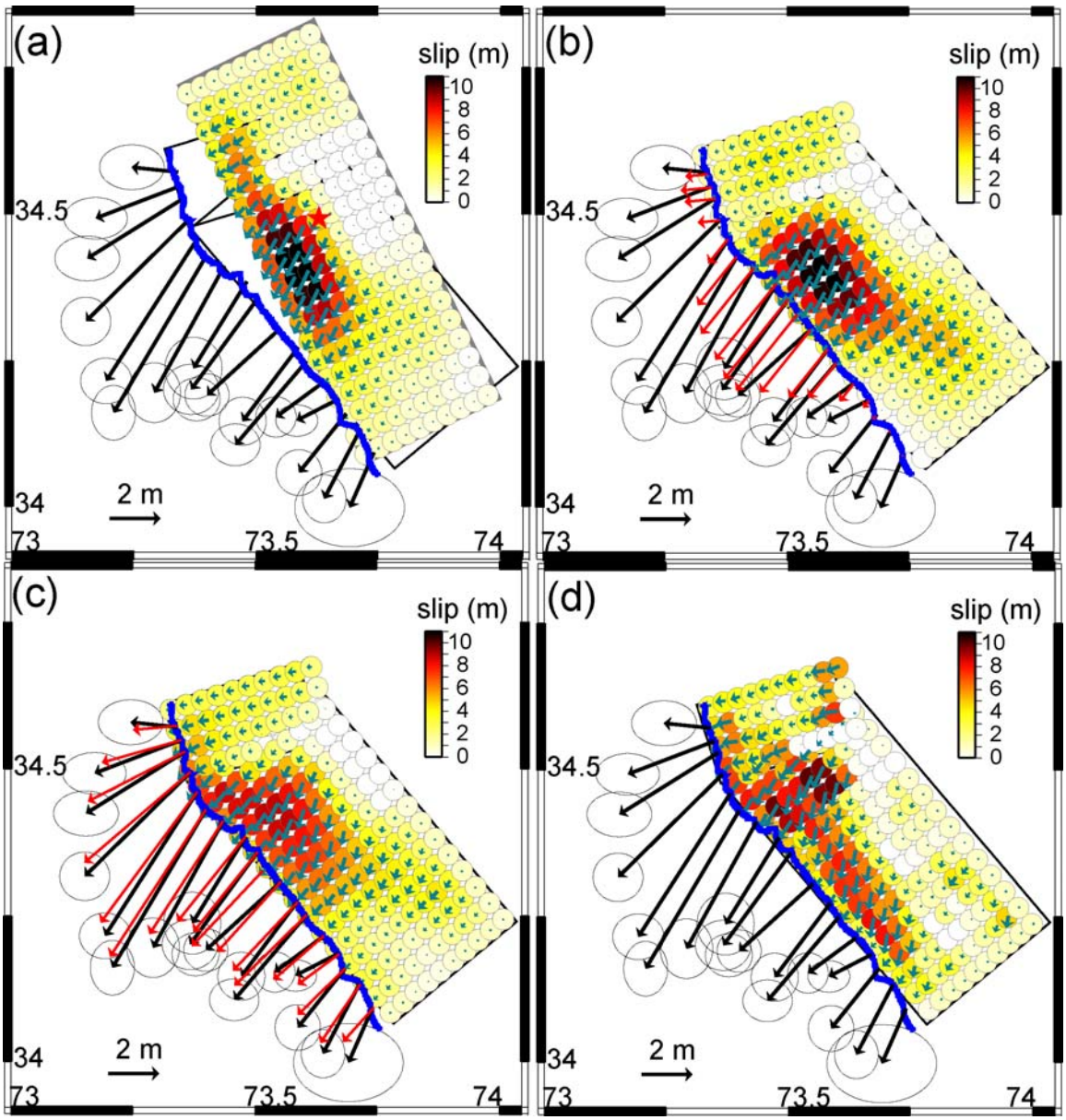

Figure 5.7 Map view of slip models. (a) Model of teleseismic data with geometry based on global CMT solution. (b) Model of teleseismic data with 2-segment geometry based on ASTER data. (c) Model of teleseismic data with 2-segment geometry based on ASTER data with constrains on surface slip. (d) Model of teleseismic and SAR data using 2-segment geometry with constrains on surface slip.

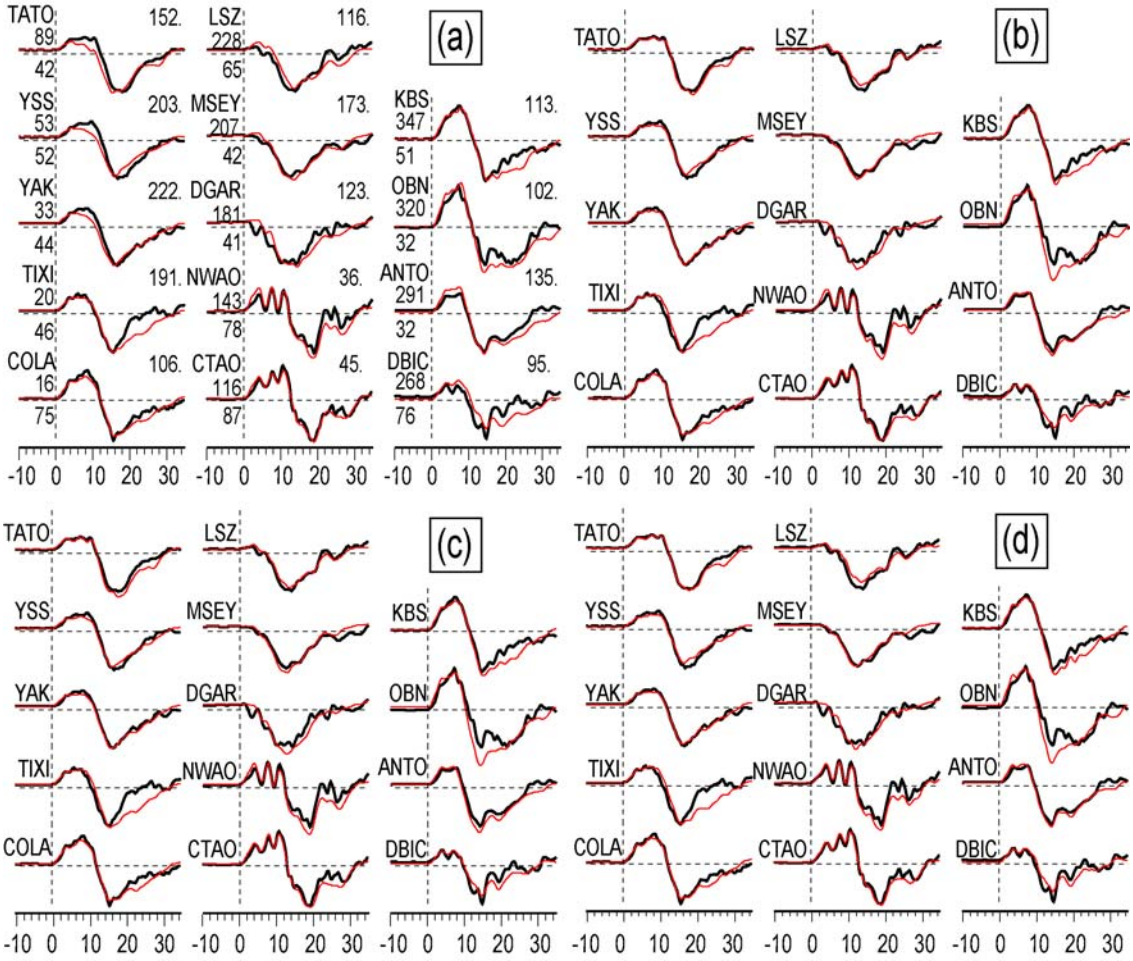

Figure 5.8 Teleseismic data fits from models in Figure 5.7. (a) Model of teleseismic data with geometry based on global CMT solution.. (b) Model of teleseismic data with 2-segment geometry based on ASTER data. (c) Model of teleseismic data with 2-segment geometry based on ASTER data with constrains on surface slip. (d) Model of teleseismic and SAR data. Measured (black) and modeled (red) seismograms are shown for the stations shown in Figure 5.5.

Figure 5.8 shows the fits of the models in Figure 5.7 to the teleseismic data. All models fit the teleseismic data with similar quality. There are classes of models that can explain the teleseismic data. In order to obtain more accurate models, additional constraints are crucial. It is important to note that the model of teleseismic data with the fault geometry and surface offsets constrained from optical imagery (Figure 5.8c) looks similar to the model that also includes three SAR image offsets (Figure 5.8d). The constraints make teleseismic model similar

to the geodetic model. As a result, we infer that the image cross-correlation can add crucial information to source studies when earthquakes have significant surface slip. If in future, the satellite images from earthquake areas can be studied close to real time, models of damage estimation and shake maps can be significantly improved.

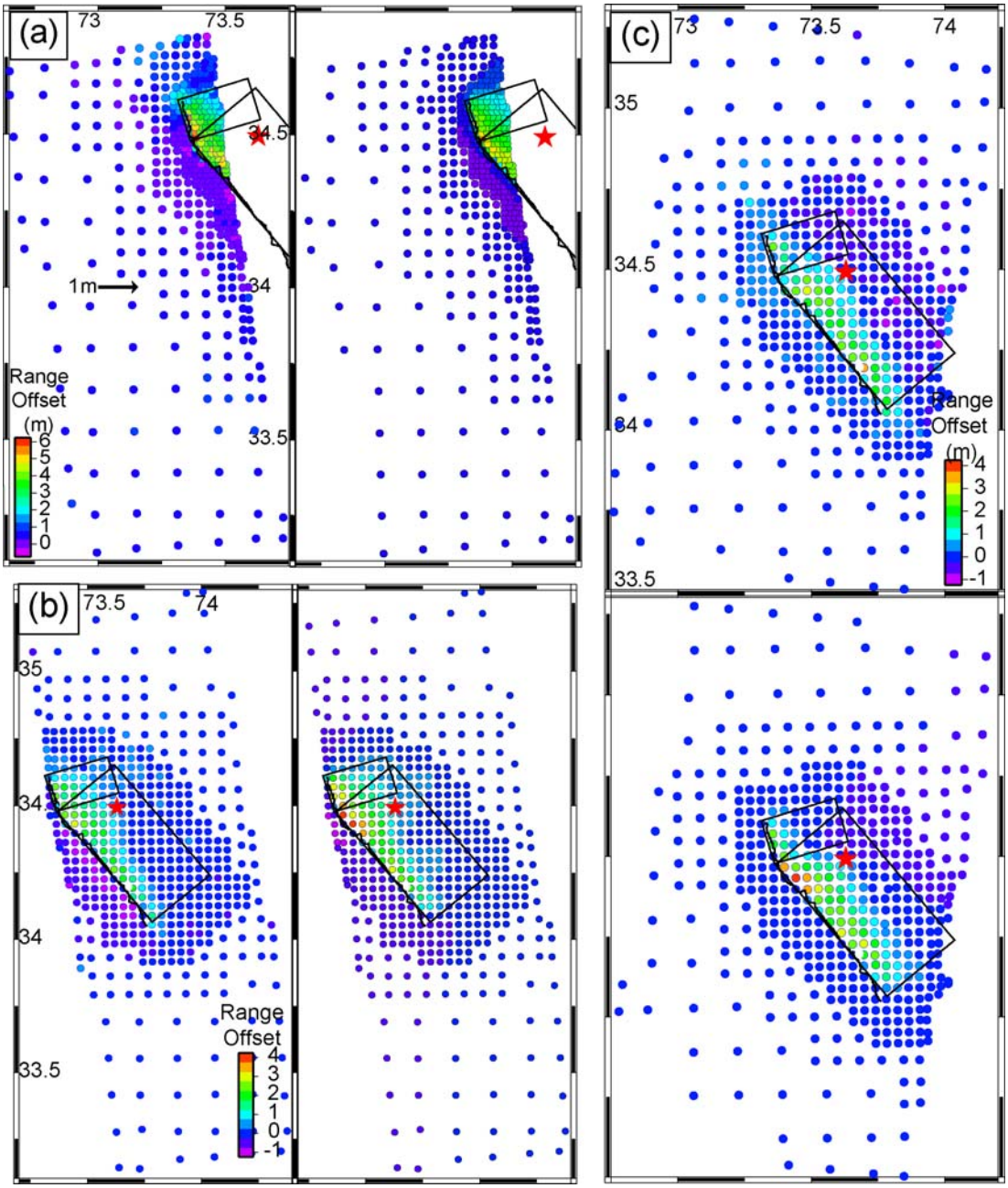

Figure 5.9 Fits to the InSAR data (a)ascending track 270, data (left) and synthetics (right); (b) ascending track 499 data (left) and synthetics (right); (c) descending track 499 data; (top) and

synthetics (bottom). Ascending tracks are primarily in up and west and descending direction is toward up and east.

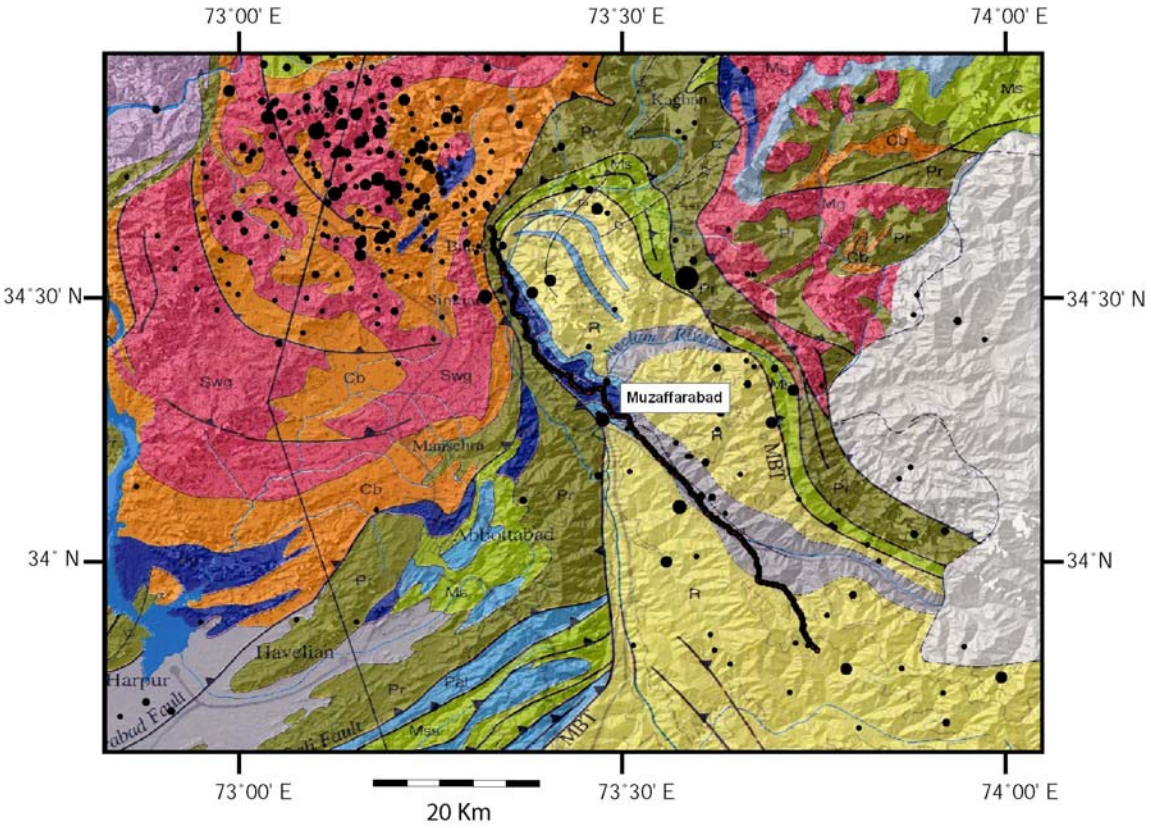

Figure 5. 10 Comparison of ruptured fault trace with bedrock geology. Geological map from Searle et al., (1996). Black dots show aftershocks up to December 31, 2006 with mb>4. The fault rupture coincides with the Muzzafarab fault (Calkins et al., 1975) northwest of Muzaffarad. Southeast of Muzaffarabad, along the upper Jehlum river valley, it has reactivated the Tanda fault (Nakata et al., 1991). The fault thrusts Precambrian limestone and shales (Pz, shown in blue) over Tertiary molasse of the Murree formation (R, shown in yellow) or over Proterozoic schists (Pr, shown in green). The Muzaffarabad fault paralls the Murree thrust, which is a segment of the Main Boundary Thrust (MBT), but has as sense of motion opposite to the long term geological motion. Southwest of Muzzaffarad the fault cuts trough the Murree formation.

5.5.3 Relation to known active faults and geological structures

The 2005 Kashmir earthquake ruptured major faults in the Muzaffarabad area which had already been identified and mapped (Calkins et al., 1975; Nakata et al., 1991). Geomorphic evidence for activity of the Tanda fault are clear (Nakata et al., 1991) (Figures 5.3); well developed triangular facets bound the northeastern flank of the valley; the topography northeast of the valley is systematically higher and more rugged than on the southwestern side of the valley; rivers, in particular the Neelum river, are systematically more entrenched into the hanging wall. Evidence for recent activity along the Muzaffarabad fault is more subtle: some triangular facets are apparent on the east the Kunhar valley (Figure 5.3); also, the topography is higher on the eastern side of the Kunhar valley. This is the opposite of what one would expect given that the eastern side consists of the Mureee molasses, a formation much more readily erodable than the Proterozoic metasediments on the western side of the valley. It is interesting to note that the Muzzaffarad fault which has thrust the Murree formation and underlying Precambrian limestones and shales over Proterozoic formations, parallels the MBT (Searle et al., 1996) (Figure 5.10) but has the opposite sense of motion and dip. This is consistent with the observation of a recent reversal of the sense of motion on the MBT (Calkins et al., 1975). It illuminates observations that recent deformation cuts across the syntaxis (Seeber, Armbruster and Quittmeyer 1981).

The fact that surface ruptures along the Muzzafarad fault parallel the MBT and terminate abruptly at the hairpin turn of the MBT is a clear indication for a strong structural control of the earthquake rupture. We also observe that the surface slip is relatively uniform along the straight fault segment along the Upper Jehlum river, suggesting that variability of the slip and geometric complexity are correlated and decrease with cumulative geological offset (Wesnousky 1990).

It is noteworthy that the aftershock activity does not correlate well with the extent of the surface ruptures and was particularly intense beyond the abrupt northern termination of rupture (Figure 5.10), along the IKSZ.

5.6. Conclusion

The Kashmir 2005 earthquake is the first modern earthquake in the Himalaya to produce documented surface rupture. Despite the complex geological setting associated with the

Hazara syntaxis, the slip pattern and source kinematics are relatively simple. This earthquake occurred along the seismicity belt which follows the front of the high range all along the arc, but it departs from previous events with similar magnitudes since it was caused by rupture of a steeply dipping thrust fault that broke all the way to the surface. The 2005 Kashmir shows that seismic hazard related to out-of-sequence thrusting in the Himalaya can be devastating and should not be overlooked, although major events along the Main Himalayan Thrust seem much more probable.

The 2005 earthquake must have increased the probability of rupture along the MHT or possible out-of-sequence thrust faults along the Himalayan front to the south east, with the possible repetition of events such the 1555 *AD* earthquake. The death toll in such an event would probably be even larger than in 2005. This should be a major concern for the growing population living in the region.

This study, carried on with 15m resolution images taken 5 years apart, demonstrates the potential of optical imagery as a complement to seismology for the analysis of large earthquakes. The models of teleseismic waves with constrains coming from optical imagery lead to models that are more consistent with geodetic data. A global coverage already exists thanks to the SPOT and ASTER programs, and even there is no doubt that high quality optical imagery, with metric or submetric resolution, will be available in the future. This warrants that the approach described here will be applicable to future large earthquake. Well constrained source models, and some estimate of near-field effects, could be produced a couple of hours after the images are available.

5.7 Acknowledgement

My collaborators in this study were Jean-Philippe Avouac, Francois Ayoub, Sebastien Leprince, and Don Helmberger.

Chapter 6: Conclusions

The conclusions for individual earthquake studies are explained in detail at the end of each chapter. As a global conclusion, I would like to express where this PhD study falls in the broader field of earthquake studies. Throughout my PhD, we have studied large earthquakes using all available datasets to understand the earthquakes, fault geometries, slip patterns and kinematics.

We have shown that by taking advantage of different sensitivities of long period data and teleseismic data, using near-field geodetic and field data, we can obtain accurate rupture models and constrain the earthquake moment along with the average dip of the megathrust. Then, dip angle and moment can be used to constrain the fault geometry and finite fault modeling.

In order to understand the earthquake phenomenon, it is important to integrate the knowledge of long term behavior of faults to the detailed studies of coseismic, postseismic and interseismic slip. This integral approach can give a clearer understanding of faulting and earthquakes. Our study of the 2007 South Sumatra earthquakes was aimed to be a step toward a more integrated comprehension of subduction zones.

The most important part that was missing in these studies was (arguably) implementing 2D or preferably 3D velocity models to examine the affects of the velocity structure on our models. In addition, earthquakes occur on boundaries that are likely to be structural discontinuities, leading to even harder obstacles, since at a discontinuity even the standard definition of "seismic moment" is inherently erroneous. Another fundamental issue of earthquake studies is using dynamical models to take advantage of the detailed kinematic earthquake studies. This is an important yet difficult step to deepen our understanding of earthquake physics.

In any case, this thesis contributes to earthquake studies by addressing fundamental questions such as; what is the rupture velocity of earthquakes? Can we constrain the fault geometry, slip distribution, rupture velocity and rise times by using more data and realistic fault geometry? How do we use different sensitivities of various frequency bands and phases of a

seismogram to develop earthquake source models? How do the coseismic ruptures relate to interseismic coupling and historical earthquakes? Can we improve rapid damage assessments and strong-motion estimations using satellite imagery and refined fault geometries?

Bibliography

Abercrombie RE, M Antolik, and G Ekstrom. (2003), The June 2000 M-w 7.9 earthquakes south of Sumatra: Deformation in the India-Australia Plate. *Journal of Geophysical Research-Solid Earth* **108**, art. no.-2018.

Agnew DC. (1997), NLOADF: A program for computing ocean-tide loading. *Journal of Geophysical Research-Solid Earth* **102**, 5109-5110.

Aki K. (1984), Asperities, Barriers, Characteristic Earthquakes and Strong Motion Prediction. *Journal of Geophysical Research* **89**, 5867-5872.

Aktar M, G Orgulu, S Ozalaybey, M Ergin, and Karabulut. Study of the aftershock sequence of 17th August Izmit earthquake (2000).

Akyuz HS. (2002), Surface rupture and slip distribution of the 12 November 1999 Duzce earthquake (M 7.1), North Anatolian fault, Bolu, Turkey. *Bull. Seism. Soc. Amer.* **92**, 61-66.

Ammon C, C Ji, H Thio, D Robinson, S Ni, V Hjorleifsdottir, H Kanamori, et al., (2005), Rupture process of the 2004 Sumatra-Andaman earthquake. *Science* **308**, 1133-1139.

Anderson JG, P Bodin, JN Brune, P J., SK Singh, R Quaas, and a M., (1986), Strong Ground Motion from the Michoacan, Mexico, Earthquake. *Science* **233**, 1043-1049.

Andrews DJ. (1976), Rupture velocity of plane strain shear cracks. *Geophys. Res. Let.* **81**, 5679–5687.

Araki E, M Shinohara, K Obana, T Yamada, Y Kaneda, and K T., (2006), Aftershock distribution of the 26 December 2004 Sumatra–Andaman earthquake from ocean bottom seismographic observation. *Earth Planets Space* **58**, 113-119.

Archuleta R. (1984), A faulting model for the 1979 Imperial Valley earthquake. *J. Geophys. Res.* **89**, 4559-4585.

Avouac JP (2003) Mountain building, erosion and the seismic cycle in the Nepal Himalaya. In: *Advances in Geophysics.* (ed. Dmowska R). Elsevier, Amsterdam.

Avouac JP, F Ayoub, S Leprince, O Konca, and DV Helmberger. (2006), The 2005, Mw 7.6 Kashmir earthquake: Sub-pixel correlation of ASTER images and seismic waveforms analysis. *Earth and Planetary Science Letters* **249**, 514-528.

Ayhan ME, R Burgmann, and S McClusky. (2001), Kinematics of the Mw 7.2, 12 November 1999, Duzce, Turkey Earthquake. *Geophys. Res. Lett.* **28**, 367-370.

Barka A. (1996), Slip Distribution along the North Anatolian Fault Associated with the Large Earthquakes of the Period 1939 to 1967. *Bull. Seism. Soc. Amer.* **86**, 1238-1254.

Bassin C, G Laske, and G Masters. (2000), The current limits of resolution for surface wave tomography in North America. *Eos Trans. AGU* **81(48)**, S12A-03.

Ben-Zion Y, and JR Rice. (1993), Earthquake Failure Sequences Along a Cellular Fault Zone in a 3-Dimensional Elastic Solid Containing Asperity and Nonasperity Regions. *Journal of Geophysical Research-Solid Earth* **98**, 14109-14131.

Bettinelli P, J-P Avouac, M Flouzat, Fo Jouanne, L Bollinger, P Willis, and G Chitrakar. (2006), Plate Motion of India and Interseismic Strain in the Nepal Himalaya from GPS and DORIS Measurements. *Journal of Geodesy*, 1.

Bilham R. (2004), Earthquakes in India and the Himalaya: tectonics, geodesy and history. *Annals Of Geophysics* **47**, 839-858.

Bilham R, VK Gaur, and P Molnar. (2001), Earthquakes - Himalayan seismic hazard. *Science* **293**, 1442-1444.

Binet R, and L Bollinger. (2005), Horizontal coseismic deformation of the 2003 Bam (Iran) earthquake measured from SPOT-5 THR satellite imagery. *Geophysical Research Letters* **32**

Birgoren G, H Sekiguchi, and K Irikura. (2004), Rupture model of the 1999 Duzce, Turkey, earthquake deduced from high and low frequency strong motion data. *Geophys. Res. Let.* **31**

Bouchon M, M Bouin, H Karabulut, M Toksoz, M Dietrich, and A Rosakis. (2001), How fast is rupture during an earthquake? New insights from the 1999 Turkey earthquakes. *Geophys. Res. Let.* **28**, 2723-2726.

Bouchon M, MN Toksoz, H Karabulut, MP Bouin, M Dietrich, M Aktar, and M Edie. (2002), Space and Time Evolution of Rupture and Faulting during the 1999 Izmit (Turkey) Earthquake. *Bull. Seism. Soc. Amer.* **92**, 256-266.

Bouchon M, N Toksoz, H Karabulut, MP Bouin, M Dietrich, M Aktar, and M Edie. (2000), Seismic imaging of the 1999 Izmit (Turkey) rupture inferred from the near-fault recordings. *Geophysical Research Letters* **27**, 3013-3016.

Bouchon M, and M Vallee. (2003), Observation of Long Supershear Rupture During the Magnitude 8.1 Kunlunshan Earthquake. *Science* **301**

Bouin MP, M Bouchon, H Karabulut, and M Aktar. (2004), Rupture process of the 1999 November 12 Duzce (Turkey) earthquake deduced from strong motion and Global Positioning System measurements. *Geophys. J. Int.* **159**, 207-211.

Briggs RW, K Sieh, AJ Meltzner, D Natawidjaja, J Galetzka, B Suwargadi, YJ Hsu, et al., (2006), Deformation and slip along the Sunda Megathrust in the great 2005 Nias-Simeulue earthquake. *Science* **311**, 1897-1901.

Burgmann R, ME Ayhan, EJ Fielding, TJ Wright, S McClusky, B Aktug, C Demir, O Lenk, and A Turkezer. (2002), Deformation during the 12 November 1999 Duzce, Turkey, earthquake, from GPS and InSAR data. *Bull. Seism. Soc. Amer.* **92**, 161-171.

Burgmann R, MG Kogan, GM Steblov, G Hilley, VE Levin, and E Apel. (2005), Interseismic coupling and asperity distribution along the Kamchatka subduction zone. *Journal of Geophysical Research-Solid Earth* **110**

Burridge R, G Conn, and LB Freund. (1979), The Stability of a rapid Mode II Shear Crack. *J. Geophys. Res. B.* **85**, 2210-2222.

Byrne DE, DM Davis, and LR Sykes. (1988), Loci and maximum size of thrust earthquakes and the mechanics of the shallow region of subduction zones. *Tectonics* **7**, 833-857.

Calkins JA, TW Offield, SKM Abdullah, and ST Ali. (1975), Geology of the southern Himalaya in Hazara, Pakistan and adjacent areas. *U.S. Geological Survey, Professional Paper* **716-C**, Washington

Chen CW, and HA Zebker. (2002), Phase unwrapping for large SAR interferograms: statistical segmentation and generalized network models: . *IEEE Transactions on Geoscience and Remote Sensing* **40**, 1709-1719.

Chlieh M, J-P Avouac, K Sieh, DH Natawidjaja, and J Galetzka. (in press), Heterogeneous coupling on the Sumatra megathrust constrained from geodetic and paleogeodetic measurements. *J. Geophys. Res.,*

Chlieh M, JP Avouac, V Hjorleifsdottir, TRA Song, C Ji, K Sieh, A Sladen, et al., (2007), Coseismic slip and afterslip of the great M-w 9.15 Sumatra-Andaman earthquake of 2004. *Bulletin of the Seismological Society of America* **97**, S152-S173.

Cochard A, and R Madariaga. (1996), Complexity of seismicity due to highly rate-dependent friction. *Journal of Geophysical Research-Solid Earth* **101**, 25321-25336.

Cotton F, and M Campillo. (1995a), Frequency-Domain Inversion of Strong Motions - Application to the 1992 Landers Earthquake. *Journal of Geophysical Research-Solid Earth* **100**, 3961-3975.

Cotton F, and M Campillo. (1995b), Stability of the Rake During the 1992, Landers Earthquake - an Indication for a Small Stress Release. *Geophysical Research Letters* **22**, 1921-1924.

Cross RS, and JT Freymueller. (2007), Plate coupling variation and block translation in the Andreanof segment of the Aleutian arc determined by subduction zone modeling using GPS data. *Geophysical Research Letters* **34**

Dahlen T, and J Tromp.(1998), *Theoretical Global Seismology* Princeton University Press, Princeton, NJ,

Delouis B, D Giardini, P Lundgren, and J Salichon. (2002), Joint inversion of InSAR, GPS, teleseismic, and strong-motion data for the spatial and temporal distribution of earthquake slip: Application to the 1999 Izmit mainshock. *Bull. Seism. Soc. Amer.* **92**, 278-299.

Deuss A, and J Woodhouse. (2001), Seismic Observations of Splitting of the Mid-Transition Zone Discontinuity in Earth's Mantle. *Science* **294**, 354-357.

Dieterich JHK, B., (1996), Implications of fault constitutive properties for earthquake prediction. *Proc. Nat. Acad. Sci. USA* **93**, 3787-3794.

Dmowska R, and LC Lovison. (1992), Influence of Asperities Along Subduction Interfaces on the Stressing and Seismicity of Adjacent Areas. *Tectonophysics* **211**, 23-43.

Dominguez S, JP Avouac, and R Michel. (2003), Horizontal coseismic deformation of the 1999 Chi-Chi earthquake measured from SPOT satellite images: Implications for the seismic cycle along the western foothills of central Taiwan. *Journal of Geophysical Research-Solid Earth* **108**, art. no.-2083.

Dunham E, and R Archuleta. (2004), Evidence for a Supershear Transient during the 2002 Denali Fault Earthquake. *Bull. Seism. Soc. Amer.* **94**, S256-S268.

Egbert GD, and SY Erofeeva. (2002), Efficient inverse Modeling of barotropic ocean tides. *Journal of Atmospheric and Oceanic Technology* **19**, 183-204.

Farr TG, PA Rosen, E Caro, R Crippen, R Duren, S Hensley, M Kobrick, et al., (2007), The Shuttle Radar Topography Mission. *Rev. Geophys.* **45**, RG2004.

Feigl KL, F Sarti, H Vadon, P Durand, S Mclusky, S Ergintav, R Bürgmann, A Rigo, D Massonnet, and R Reilinger. (2002), Estimating slip distribution for the Izmit mainshock from coseismic GPS, ERS-1, RADARSAT and SPOT measurements. *Bull. Seism. Soc. Amer., in press*

Freymueller JT, and J Beavan. (1999), Absence of strain accumulation in the western shumagin segment of the Alaska subduction zone. *Geophysical Research Letters* **26**, 3233-3236.

Fujiwara S, M Tobita, HP Sato, S Ozawa, H Une, M Koaarai, H Nakai, et al., (2006), Satellite Data Gives Snapshot of the 2005 Pakistan Earthquake. *EOS, Transactions, American Geophysical Union* **87**

Guilbert J, J Vergoz, E Schissele, A Roueff, and Y Cansi. (2005), Use of hydroacoustic and seismic arrays to observe rupture propagation and source extent of the M-w=9.0 Sumatra earthquake. *Geophysical Research Letters* **32**

Haeussler PJ, DP Schwartz, TE Dawson, H Stenner, JJ Lienkaemper, B Sherrod, FR Cinti, et al., (2004), Surface Rupture and Slip Distribution of the Denali and Totschunda Faults in the 3 November 2002 M 7.9 Earthquake, Alaska. *Bull. Seism. Soc. Amer.* **94**, 23-52.

Hartzell S, and D Helmberger. (1982a), Strong-motion modelling of the Imperial Valley earthquake of 1979. *Bull.Seism.Soc.Am.* **72**, 571-596.

Hartzell S, and DV Helmberger. (1982b), Strong-motion Modeling of the Imperial-Valley Earthquake of 1979. *Bull. Seism. Soc. Amer.* **72**, 571-596.

Hartzell SH, and TH Heaton. (1983), Inversion of Strong Ground Motion and Teleseismic Waveform data for the Fault Rupture History of the 1979 Imperial Valley, California, EARTHQUAKE. ***Bull. Seism. Soc. Amer.*** **73**, 1553-1583.

Heaton TH. (1990), Evidence for and implications of self-healing pulses of slip in earthquake rupture. *Physics of the Earth and Planetary Interiors* **64**, 1-20.

Hernandez B, F Cotton, and M Campillo. (1999), Contribution of radar interferometry to a two-step inversion of the kinematic process of the 1992 Landers earthquake. *J. Geophys. Res.* **104**, 13083-13099.

Honda R, S Aoi, N Morikawa, H Sekiguchi, T Kunugi, and H Fujiwara. (2004), Ground motion and rupture process of the 2003 Tokachi-oki earthquake obtained from strong motion data of K-NET and KiK-net. *Earth Planets and Space* **56**, 317-322.

Hsu YJ, M Simons, JP Avouac, J Galetzka, K Sieh, M Chlieh, D Natawidjaja, L Prawirodirdjo, and Y Bock. (2006), Frictional afterslip following the 2005 Nias-Simeulue earthquake, Sumatra. *Science* **312**, 1921-1926.

Ji C, D Helmberger, and DM Wald, KF. (2003), Slip history and dynamic implications of the 1999 Chi-Chi, Taiwan, earthquake. *Journal of Geophysical Research-Solid Earth* **108**, Art. No. 2412.

Ji C, DV Helmberger, T-RA Song, K-F Ma, and DJ Wald. (2001), Slip distribution and tectonic implications of the 1999 Chi-Chi, Taiwan earthquake. *Geophysical Research Letters* **28**, 4379-4382.

Ji C, K Larson, K Hudnut, and K Choi. (2004), Slip history of the 2003 San Simeon earthquake constrained by combining 1--Hz GPS, strong motion, and teleseismic data. *Geophys. Res. Let.* **31**, L17608.

Ji C, D Wald, and DV Helmberger. (2002a), Source Description of the 1999 Hector Mine, California Earthquake, Part I: Wavelet Domain Inversion Theory and Resolution Analysis. *Bull. Seismol. Soc. Am.* **92**, 1192-1207.

Ji C, DJ Wald, and DV Helmberger. (2002b), Source description of the 1999 Hector Mine, California, earthquake, part I: Wavelet domain inversion theory and resolution analysis. *Bull. Seism. Soc. Amer.* **92**, 1192-1207.

Ji C, DJ Wald, and DV Helmberger. (2002c), Source Description of the 1999 Hector Mine, California, Earthquake, Part II: Complexity of Slip History *Bull. Seism. Soc. Am.* **92**, 1208-1226.

Kanamori H, and J Given. (1981), Use of long-period surface waves for rapid determination of earthquake-source parameters. *Physics of the Earth and Planetary Interiors* **27**, 8-31.

Kanamori H, and GS Stewart. (1976), Mode of the strain release along the Gibbs fracture zone, Mid-Atlantic ridge. *Physics of the Earth and Planetary Interiors* **11**, 312-332.

Karig D, M Lawrence, G Moore, and J Curray. (1980), Structural framework of the fore-arc basin, NW Sumatra. *Geological Society of London Journal* **137**, 77-91.

Komatitsch D, and J Tromp. (2002a), Spectral-element simulations of global seismic wave propagation - I. Validation. *Geophysical Journal International* **149**, 390-412.

Komatitsch D, and J Tromp. (2002b), Spectral-element simulations of global seismic wave propagation - II. Three-dimensional models, oceans, rotation and self-gravitation. *Geophysical Journal International* **150**, 303-318.

Konca AO, V Hjorleifsdottir, TRA Song, JP Avouac, DV Helmberger, C Ji, K Sieh, R Briggs, and A Meltzner. (2007), Rupture kinematics of the 2005 M-w 8.6 Nias-Simeulue earthquake from the joint inversion of seismic and geodetic data. *Bulletin of the Seismological Society of America* **97**, S307-S322.

Kumar S, SG Wesnousky, TK Rockwell, R Briggs, VC Thakur, and R Jayangondaperumal. (2006), Paleoseismic evidence of great surface-rupture earthquakes along the Indian Himalaya. *Journal Of Geophysical Research* **111**, doi: 10.1029/2004JB003309.

Lapusta N, and JR Rice. (2003), Nucleation and early seismic propagation of small and large events in a crustal earthquake model. *Journal of Geophysical Research-Solid Earth* **108**, art. no.-2205.

Lay T, H Kanamori, CJ Ammon, M Nettles, SN Ward, RC Aster, SL Beck, et al., (2005), The great Sumatra-Andaman earthquake of 26 December 2004. *Science* **308**, 1127-1133.

Lay T, H Kanamori, and L Ruff. (1982), The Asperity Model and the Nature of Large Subduction Zone Earthquakes. *Earthquake Prediction Research* **1**, 3-71.

Leprince S, S Barbot, F Ayoub, and JP Avouac. (2007), Automatic, Precise, Ortho-Rectification and Co-Registration for Satellite Image Correlation, Application to Seismotectonics. *IEEE Transactions on Geoscience and Remote Sensing* **45**, 1529-1558.

Liu Y, and JR Rice. (2005), Aseismic slip transients emerge spontaneously in three-dimensional rate and state modeling of subduction earthquake sequences. *J. Geophys. Res.* **110**, B08307.

Lohman RB, and M Simons. (2005), Some thoughts on the use of InSAR data to constrain models of surface deformation: Noise structure and data downsampling. *Geochem. Geophys. Geosyst* **6**

McGill SF, and CM Rubin. (1999), Surficial slip distribution on the central Emerson fault during the June 28, 1992, Landers earthquake, California. *Journal of Geophysical Research-Solid Earth* **104**, 4811-4833.

Meltzner AJ, K Sieh, M Abrams, DC Agnew, K Hudnut, JP Avouac, and D Natawidjaja. (2006), Uplift and Subsidence Associated with the Great Aceh-Andaman Earthquake of 2004. *Journal Of Geophysical Research* **111**, doi: 10.1029/2005JB003891.

Michel R, and JP Avouac. (2002), Deformation due to the 17 August 1999 Izmit, Turkey, earthquake measured from SPOT images. *Journal of Geophysical Research-Solid Earth* **107**, art. no.-2062.

Michel R, J.P. Avouac, and J. Taboury. (1999), Measuring ground displacements from SAR amplitude images : Application to the Landers earthquake. *Geophys. Res. Lett.* **26**, 875-878.

Mindavelli O, and BJ Mitchell. (1989), Crustal Structure and Possible Anisotropy in Turkey from Seismic Surface Wave Dispersion *Geophysical journal international* **98**, 93-106.

Nakata T, H Tsutsumi, SH Khan, and RD Lawrence Active Faults of Pakistan, p. 141 pp. Research Center for Regional Geography Hiroshima University, Hiroshima, Japan.(1991)

Natawidjaja DH, K Sieh, M Chlieh, J Galetzka, BW Suwargadi, H Cheng, RL Edwards, JP Avouac, and SN Ward. (2006), Source parameters of the great Sumatran megathrust earthquakes of 1797 and 1833 inferred from coral microatolls. *Journal of Geophysical Research-Solid Earth* **111**

Newcomb KR, and WR McCann. (1987), Seismic History and Seismo Tectonics of the Sunda Arc. *Journal of Geophysical Research* **92**, 421-439.

Olsen KB, R Madariaga, and RJ Archuleta. (1992), Three-Dimensional Dynamic Simulation of the 1992 Landers Earthquake. *Science* **278**

Olson AH, and RJ Apsel. (1982), Finite Faults and Inverse-Theory with Applications to the 1979 Imperial-Valley Earthquake. *Bull. Seism. Soc. Amer.* **72**, 1969-2001.

Pacheco JF, LR Sykes, and CH Scholz. (1993), Nature of Seismic Coupling Along Simple Plate Boundaries of the Subduction Type. *Journal of Geophysical Research* **98**, 14133-14160.

Park J, and F Gilbert. (1986), Coupled Free Oscillations of an Aspherical, Dissipative, Rotating Earth: Galerkin Theory. *Journal of Geophysical Research* **91**, 7241-7260.

Park SC, and J Mori. (2007), Are asperity patterns persistent? Implication from large earthquakes in Papua New Guinea. *Journal of Geophysical Research-Solid Earth* **112**

Pathier E, EJ Fielding, TJ Wright, R Walker, BE Parsons, and S Hensley. (2006), Displacement Field and Slip Distribution of the 2005 Kashmir Earthquake from SAR imagery. *Geophys. Res. Let.* **33**, L20310.

Perfettini H, and JP Ampuero. (2008), Dynamics of a velocity strengthening fault region: Implications for slow earthquakes and postseismic slip. *Journal of Geophysical Research*

Pondard N, R Armijo, GCP King, B Meyer, and F Flerit. (2007), Fault interactions in the Sea of Marmara pull-apart (North Anatolian Fault): earthquake clustering and propagating earthquake sequences. *Geophys. J. Int.* **171**, 1185-1197.

Pritchard ME, and M Simons. (2006), An aseismic slip pulse in northern Chile and along-strike variations in seismogenic behavior. *Journal of Geophysical Research-Solid Earth* **111**

Pucci S, N Palyvos, C Zabci, D Pantosti, and M Barchi. (2006), Coseismic ruptures and tectonic landforms along the Duzce segment of the North Anatolian Fault Zone (Ms 7.1, November 1999) *J. Geophys. Res.* **111**

Pucci SS, D Pantosti, MR Barchi, and N Palyvos. (2007), A complex seismogenic shear zone: The Duzce segment of north anatolian fault (Turkey). *Earth and planetary science letters* **262**, 185-203.

Ritsema J, H van Heijst, and J Woodhouse. (1999), Complex shear wave velocity structure imaged beneath Africa and Iceland. *Science* **286**, 1925-1928.

Rosakis A, O Samudrala, and D Coker. (1999), Cracks faster than the shear wave speed. *Science* **284**, 1337-1340.

Rosen PA, S Henley, G Peltzer, and S M., (2004), Updated Repeat Orbit Interferometry Package Released,. *Eos Trans. AGU* **85**, 47.

Ruegg J, J Campos, R Armijo, S Barrientos, P Briole, R Thiele, M Arancibia, et al., (1996), The M_w = 8.1 Antofagasta (North Chile) Earthquake of July 30,1995: First results from teleseismic and geodetic data. *Geophys.Res.Lett.* **23**, 917-920.

Ruff L, and H Kanamori. (1983), Seismic Coupling and Uncoupling at Subduction Zones. *Tectonophysics* **99**, 99-117.

Rundle JB, and H Kanamori. (1987), Application of an Inhomogeneous Stress (Patch) Model to Complex Subduction Zone Earthquakes - a Discrete Interaction Matrix Approach. *Journal of Geophysical Research-Solid Earth and Planets* **92**, 2606-2616.

Sandwell D, R Mellors, M Shimada, B Brooks, and J Foster. (2007), Accuracy and Resolution of ALOS Interferometry: Vector Deformation Maps of the Father's Day Intrusion at Kilauea, . *IEEE Geoscience and Remote Sensing Letters*

Schiek CG, and JM Hurtado. (2006), Slip analysis of the Kokoxili earthquake using terrain change detection and regional

earthquake data. *Geosphere*

Scholz C.(1990), *The Mechanics of Earthquakes and Faulting* Cambridge University Press, New York,

Scoffin TP, and RF McLean. (1978), Exposed limestones of the northern province of the Great Barrier Reef. *Philosophical Tranactions Royal Society of London, Series A* **291**, 119-138.

Scoffin TP, and DR Stoddart. (1978), The nature and significance of microatolls. *Phil□ osophical Transactions of the Royal Society London, Series B* **284**, 99-122.

Searle MP, M Khan, MQ Jan, JA DiPietro, KR Pogue, DA Pivnik, WJ Sercombe, et al. Geological Map of North Pakistan (Western Himalaya, Salt Ranges, Kohistan, Karakoram, Hindu Kush).(1996)

Seeber L, J Armbruster, and R Quittmeyer (1981) Seismicity and continental collision in the Himalayan arc. In: *Zagros-Hindukush-Himalaya: Geodynamic Evolution* (ed. Gupta HK, and Delany, F.M.), pp. 215-242. Amerian Geophysical Union, Washington.

Sekiguchi H, and T Iwata. (2002), Rupture Process of the 1999 Kocaeli, Turkey, Earthquake Estimated from Strong-Motion Waveforms. *Bull. Seism. Soc. Amer.* **92**, 300-311.

Shimada M, O Isoguchi, T Tadono, R Higuchi, and K Isono PALSAR CALVAL Summary and Update. In: *IGARSS07*, Barcelona.(2007a)

Shimada M, O Isoguchi, T Tadono, R Higuchi, and K Isono. PALSAR CALVAL Summary and Update 2007 (2007b).

Shimazaki K, and T Nakata. (1980), Time-predictable recurrence model for large earthquakes. *Geophys. Res. Lett.* **7**, 279-282.

Sieh K, and D Natawidjaja. (2000), Neotectonics of the Sumatran fault, Indonesia. *Journal of Geophysical Research* **105**, 28295-28326.

Simons M, Y Fialko, and L Rivera. (2002), Coseismic deformation from the 1999 M-w 7.1 Hector Mine, California, earthquake as inferred from InSAR and GPS observations. *Bulletin of the Seismological Society of America* **92**, 1390-1402.

Subarya C, M Chlieh, L Prawirodirdjo, JP Avouac, Y Bock, K Sieh, AJ Meltzner, DH Natawidjaja, and R McCaffrey. (2006), Plate-boundary deformation associated with the great Sumatra-Andaman earthquake. *Nature* **440**, 46-51.

Suwa Y, S Miura, A Hasegawa, T Sato, and K Tachibana. (2006), Interplate coupling beneath NE Japan inferred from three-dimensional displacement field. *Journal of Geophysical Research-Solid Earth* **111**

Taylor FW, C Frohlich, J Lecolle, and M Strecker. (1987), Analysis of Partially Emerged Corals and Reef Terraces in the Central Vanuatu Arc - Comparison of Contemporary Coseismic and Nonseismic with Quaternary Vertical Movements. *Journal of Geophysical Research-Solid Earth and Planets* **92**, 4905-4933.

Thatcher W. (1990), Order and diversity in the modes of Circum-Pacific earthquake recurrence. *J. Geophys. Res.* **95**, 2609-2623.

Tse ST, and JR Rice. (1986), Crustal earthquake instability in relation to depth variation of frictional slip properties. *J. Geophys. Res.* **91**, 9452-9472.

Tsuboi S, D Komatitsch, C Ji, and J Tromp. (2003), Broadband modeling of the 2002 Denali fault earthquake on the Earth Simulator *Physics of the Earth and Planetary Interiors* **139**, 305-312.

Van Puymbroeck N, Michel, R., Binet, R., Avouac, J.P. and J. Taboury. (2000), Measuring earthquakes from optical satellite images. *Applied Optics Information Processing* **39**, 1-14.

Wald DJ, DV Helmberger, and TH Heaton. (1991), Rupture Model of the 1989 Loma Prieta Earthquake from the Inversion of Strong-Motion an Broadband Teleseismic Data. *Bull. Seism. Soc. Am.* **81**, 1540-1572.

Wesnousky SG. (1990), Seismicity as a function of Cumulative geologic offset: Some observations from southern California. *Bull. Seismol. Soc. Am.* **80**, 1374-1381.

Woodhouse J. (1981), The excitation of long period seismic waves by a source spanning a structural discontinuity. *Geophys. Res. Let.* **8**, 1129-1131.

Xia K, A Rosakis, and K H. (2004), Laboratory earthquakes: The sub-Rayleigh-to-supershear rupture transition. *Science* **303**, 1859-1861.

Xie X, and ZX Yao. (1989), A generalized reflection-transmission coefficient matrix method to calculate static desplacement field of a dislocation source in a stratified half space. *Chinese Journal of Geophysics* **32**, 191-205.

Yagi Y. (2004), Source rupture process of the 2003 Tokachi-oki earthquake determined by joint inversion of teleseismic body wave and strong ground motion data. *Earth Planets and Space* **56**, 311-316.

Yeats RS, and A Hussain. Surface Features of the Mw 7.6, 8 October 2005 Kashmir Earthquake, Northern Himalaya, Pakistan: Implications for the Himalayan Front (2006).

Yeats RS, T Nakata, A Farah, M Fort, MA Mirza, MR Pandey, and RS Stein. (1992), The Himalayan Frontal Fault System. *Annales Tectonicae* **6**, 85-98.

Yu SB, L. C. Kuo, Y. J. Hsu, H. H. Su, C. C. Liu, C. S. Hou, J. F. Lee, T. C. Lai, C. C. Liu, C. L. Liu, T. F. Tseng, C. S. Tsai, and T. C. Shin. (2001), Preseismic deformation and coseismic displacements associated with the 1999 Chi-Chi, Taiwan, earthquake. *Bull. Seism. Soc. Am.* **91**, 995-1012.

Zachariasen J, K Sieh, F Taylor, RL Edwards, and WS Hantoro. (1999), Submergence and uplift associated with the giant 1833 Sumatran subduction earthquake: Evidence from coral microatolls. *J.Geophys.Res.* **104**, 895-919.

Zachariasen J, K Sieh, F Taylor, and WS Hantoro. (2000), Modern vertical deformation at the Sumatran subduction zone: Paleogeodetic Insights from Coral Microatolls. *Bull.Seism.Soc.Am.* **90**, 897-913.